HHS Public Access

Author manuscript

Prog Mater Sci. Author manuscript; available in PMC 2025 April 01.

Published in final edited form as:

Prog Mater Sci. 2024 April ; 142: . doi:10.1016/j.pmatsci.2023.101228.

Recent progress in multifunctional, reconfigurable, integrated liquid metal-based stretchable sensors and standalone systems

Jia Zhu[1,2,*], **Jiaying Li**[1], **Yao Tong**[3], **Taiqi Hu**[4], **Ziqi Chen**[5], **Yang Xiao**[1], **Senhao Zhang**[3], **Hongbo Yang**[3], **Min Gao**[1], **Taisong Pan**[1], **Huanyu Cheng**[2,*], **Yuan Lin**[1,6,*]

[1]School of Material and Energy, University of Electronic Science and Technology of China, Chengdu 610054, China

[2]Department of Engineering Science and Mechanics, The Pennsylvania State University, University Park, Pennsylvania 16802, USA

[3]Suzhou Institute of Biomedical Engineering and Technology, Chinese Academy of Science, Suzhou 215011, PR China

[4]School of Electrical Engineering and Automation, Jiangxi University of Science and Technology, Ganzhou 341000, P. R. China

[5]School of Physical Sciences, University of Science and Technology of China, Hefei 230026, PR China

[6]Medico-Engineering Cooperation on Applied Medicine Research Center, University of Electronics Science and Technology of China, Chengdu 610054, China

Abstract

Possessing a unique combination of properties that are traditionally contradictory in other natural or synthetical materials, Ga-based liquid metals (LMs) exhibit low mechanical stiffness and flowability like a liquid, with good electrical and thermal conductivity like metal, as well as good biocompatibility and room-temperature phase transformation. These remarkable properties have paved the way for the development of novel reconfigurable or stretchable electronics and devices. Despite these outstanding properties, the easy oxidation, high surface tension, and low rheological viscosity of LMs have presented formidable challenges in high-resolution patterning. To address this challenge, various surface modifications or additives have been employed to tailor the oxidation state, viscosity, and patterning capability of LMs. One effective approach for LM patterning is breaking down LMs into microparticles known as liquid metal particles (LMPs). This facilitates LM patterning using conventional techniques such as stencil, screening, or inkjet printing. Judiciously formulated photo-curable LMP inks or the introduction of an adhesive seed layer combined with a modified lift-off process further provide the micrometer-level LM patterns. Incorporating porous and adhesive substrates in LM-based electronics allows direct interfacing

[*]To whom correspondence should be addressed. zhujia1990@uestc.edu.cn (J.Z.), Huanyu.Cheng@psu.edu (H.C.), and linyuan@uestc.edu.cn (Y.L.).

with the skin for robust and long-term monitoring of physiological signals. Combined with self-healing polymers in the form of substrates or composites, LM-based electronics can provide mechanical-robust devices to heal after damage for working in harsh environments. This review provides the latest advances in LM-based composites, fabrication methods, and their novel and unique applications in stretchable or reconfigurable sensors and resulting integrated systems. It is believed that the advancements in LM-based material preparation and high-resolution techniques have opened up opportunities for customized designs of LM-based stretchable sensors, as well as multifunctional, reconfigurable, highly integrated, and even standalone systems.

1. Introduction

Gallium (Ga) and Ga-based liquid metals (LMs) have combined good conductivity and flowability with biocompatibility and phase transition at room temperature, providing unique application opportunities in biosensing, energy harvesting, circuits, active switches, and biomedicine [1–4]. Common stretchable conductors often rely on the use of stretchable structures (e.g., island-bridge [5–7], serpentine [8], and kirigami design [9]) or stretchable materials with conductive nanofillers (e.g., graphene [10, 11], carbon black [12], carbon nanotube [13–15], metal nanoparticle/nanowire/nanodisk [16, 17], and MXene [18, 19]). Compared with them, LMs-based devices exhibit much higher stretchability and strain-insensitivity conductivity for use under severe deformations [20–24]. Due to high reactivity, an oxide layer with a self-limiting thickness is formed on the surface of LMs in the ambient environment [25]. The existence of the oxide layer has a profound impact on the mechanical and rheological properties of LMs, including improved stiffness, wettability, viscosity, and interactions with other materials [26–28]. The fundamental study of the intrinsic properties of LMs and their oxide layer has laid a solid foundation for further modifications and optimization of LMs. Surface modification on LMs or LM particles (LMPs) has been proven to be an effective way to control the oxide extent, improve dispersion stability, and load drugs. Incorporating polymers can also provide LMs with enhanced light absorption and photothermal properties [29].

Due to the high surface tension of LMs, traditional stencil or screen printing is not applicable. Fabricating high-resolution LM patterns has become a main challenge in the field of LM-based electronics [30]. Direct printing of LMs to form complex 3D structures can be achieved by exploiting the self-supporting oxide layer. For instance, vigorously stirring the pristine bulky LM can modify its rheology and render an easily applicable paste due to the accumulated oxidation, enabling simple application on aluminum-based biomedical devices [31]. Direct integration with microfluidics also allows simple LM patterning for low-cost, high-integrated, and multifunctional stretchable systems [32, 33]. Recently developed LM patterning techniques include modifying LMs with metal or metal oxide microparticles to form a printable paste [34], introducing metallic seed layering for selective wetting [35], or breaking LMs down to form printable LM particles (LMPs) [36, 37]. Among them, LMPs have drawn intensive attention due to their low cost and scalable production potential in LM-based stretchable electronics. Despite the aforementioned advantages, the oxide layer of LMPs is intrinsically insulating to block the conductive pathway. In order to circumvent this issue, two main strategies have been proposed: rendering the insulating oxide layer

conductive by chemical modifications [38] or rupturing the oxide layer to expose inner LMs (by mechanical, thermal, or laser activation) [39, 40]. With the surface-modification or interfacial wetting, LMs can be patterned on various elastomeric substrates via inject printing [41], stencil printing [42–44], or blading coating [45]. LM patterning can achieve a spatial resolution from hundreds of microns in inject printing to several microns in photolithography [46].

In applications intended for use on the human body, factors such as adhesion and gas permeability require special consideration [47–49]. Good adhesion to form an intimate interface and gas permeability provides an enhanced level of comfort for high-fidelity and long-term monitoring of physiological signals while avoiding irritation or infection [50–52]. Considering the low adhesion of LMs to human skins, mixing LMPs with specific polymers to form adhesive inks or building LM patterns on adhesive substrates have been exploited to improve the adhesion of LM-based electronics. High gas permeability of on-skin electronics requires the use of porous substrates, which can be fabricated from templates, electrospinning, or the phase separation method [53–56]. However, microstructures in the porous substrate reduce the wettability of LMs, which is adverse to LM patterning. At the same time. LM leakage may degrade the performance of LM-based electronics.

By exploiting the unique and versatile properties of LMs, various stretchable devices have been recently developed, including passive stretchable electrodes or interconnections [57–59], mechanical or chemical sensors [60–63], energy harvesters or storage units [45, 64–68], active switches [69, 70], and integrated systems [71–73]. Structural engineering strategies have also been widely adopted to tune the electromechanical properties of LMs, switching the use from passive stretchable interconnections and electrodes to active mechanical sensors. This review will first introduce the intrinsic physical and chemical properties of Ga-based LMs and their oxides, along with various surface modification strategies. Next, newly developed patterning techniques to circumvent the high surface tension of LM in the fabrication of LM-based electronics will be discussed. Moving forward, LM-based electronics with good adhesion and high gas permeability for on-body applications are further elaborated. Lastly, the state-of-the-art LM-based devices, from single sensing units and functional modules to highly integrated systems, are reviewed.

2. Intrinsic properties of Ga-based LMs and the oxide layer

Gallium belongs to the group III_A in the periodic table, with chemical properties analogous to aluminum. Pristine gallium has a melting point of ~ 29.8°C and an extremely high boiling point of ~ 2400°C, which results in zero vapor pressure at room temperature [74, 75]. Adding other metals to form eutectic alloys can lower the melting point further. For example, eutectic indium gallium (EGaIn) with a Ga/In mixing ratio of 75.5:24.5 as the most representative Ga alloy has a melting point of 15.5°C. Ga and Ga-based alloys in the liquid state are reported to have high surface tension (i.e., 705–730, 624, 600 mN/m for Ga, EGaIn, and Galinstan), which makes them tend to form a spherical shape in free space.

Highly reactive gallium leads to the formation of amorphous or poorly crystalline Ga oxide (α-Ga_2O_3) on its surface in the environment with an oxygen level over 20 ppm [76]. Since

gallium (−0.549 eV) has a higher negative redox potential than indium (−0.444 eV), the oxide layer is dominated by gallium oxide [77]. The thickness of the α-Ga_2O_3 layer is only 0.5–5 nm due to the self-limiting oxidation process, as described by the Cabrera-Mott oxidation mechanism [77–79]. The oxide layer has multiple influences on LMs, including modifying the surface tension of LMs by changing the chemical composition, serving as an interface layer to enhance interactions with other materials, and providing mechanical support for LMs due to its much higher stiffness and yield strength. In most cases, the surface tension of oxidized LMs is intangible due to its entanglement with the high yield strength of the oxide layer (500 mN/m). The effective surface tension which is the linear sum of contributions from the liquid surface tension and the yield stress was obtained in experimental measurements. These values obtained by submerging LM droplets of different sizes in various HCl baths within the pendant drop method show a large range due to different droplet sizes and oxidation thicknesses [80]. Therefore, obtaining the equilibrium of oxidized LMs by softening the oxide layer is an essential step to extract the effective surface tension of oxidized LMs in measurements. In one representative study, gradually attenuated vibrations were applied to LM droplets to yield their equilibrium shapes, and the surface tension of oxidized LMs was calculated to be 350−365 mN/m by the puddle height method [81]. Moreover, the oxide layer provides reactive sites for electrostatic adsorption or chemical modification to tailor the intrinsic properties of LMs. When treated with a high temperature of 750°C, a highly crystalline Ga oxide (β-Ga_2O_3) with semiconducting properties can also form on the surface of LMs [82]. The basic properties of LMs and the oxide are summarized in Table 1.

3. Surface modification of Ga-based LMs

Surface modification is an effective way to provide LMs with unique properties for drug loading, antioxidation, thermal actuation, and electronic doping, especially for LMPs. Depending on the surface state of LMs, surface modification is realized by chemical bonding between doped molecules and Ga or Ga_2O_3. With unpaired free electrons, Ga can form the Ga-S bond with thiols or serve as radicals in polymerization reactions, whereas Ga_2O_3 provides anchoring sites for surface functionalization with hydroxyl groups (Fig. 2a).

The high reactivity and unpaired electron of Ga make it a potential polymerization radical initiator. For instance, the exposed gallium can rapidly initiate free radical polymerization (FRP) with vinyl monomers, directly grafting hydrophilic polymers with high molecular weight onto the Ga surface [83]. This method is useful for fabricating highly stretchable LM-based functional hydrogels, such as poly-acrylamide (PAAm) and poly(N-isopropylacrylamide) (PNIPAAm) with enhanced electrical conductivity, thermal dissipation, and chemical reaction arising from LM additives. Thiol modification is the most commonly used method for Ga-based LMs, which competes with oxygen for surface sites in the formation of Ga_2O_3 and promotes the “softening” of LMs [84]. Thiol groups can form ordered, densely packed self-assembled monolayers (SAMs) on Ga surfaces through covalent polarization [85, 86]. The rapid self-assembly of thiolates can form a tightly packed two-dimensional ordered monolayer on the surface of Ga-based LMs, protecting the material from oxidation [86]. Additionally, thiols can also moderate the growth of gallium oxide by competing with oxygen for surface sites [84]. Meanwhile, various thiols can alter the

thermodynamics of oxide layer growth by changing the work function of Ga-based LMs. By controlling the thickness of the oxide layer on the surface of LMs, different levels of the "softening" effect can be achieved [87, 88]. Since thiol groups are often associated with an unpleasant odor and can be easily oxidized, the trithiocarbonate-functionalized brushed polyethylene glycol (bPEG) with molecular weights of 5–20 kDa can be explored as an alternative surface modifier (Fig. 2b) [89]. The resulting LMPs are homogeneous and stable in biological buffers due to steric repulsion between large conjugated molecules. Additionally, the addition of trisodium citrate further inhibits oxidation of the LM surface and stabilizes the dispersion. The carboxyl group on bPEG can form amide bonds with functional biomolecules by the 1-ethyl-3-(3-dimethylaminopropyl)carbodiimide (EDC)-mediated cross-linking method. A proof-of-concept demonstration includes a successful graft of fluorescent antibodies to the bPEG layer on the surface of LMPs.

Functional polymers or drugs have been conjugated with metal nanoparticles (NPs) through thiol ligands for catalyst, biosensing, or drug delivery [90]. Similarly, the highly reactive Ga linked with various thiols extends its biomedical applications, including biosensing [91], drug delivery [92], and bioimaging [93]. LMPs are usually prepared by a "top-down" sonication method. Therefore, the oxide layer formed during sonication needs to be removed before successful modifications with thiols. In a representative study, an LMP-based nanomedicine with excellent chemotherapeutic inhibition towards the xenograft tumor is prepared through a delicate design of ligand modifications (Fig. 2c) [92]. The addition of thiolated hyaluronic acid (*m*-HA) during sonication removes the oxide layer to expose the inner Ga and acts as the active targeting moiety. Another ligand, thiolated (2-hydroxypropyl)-β-cyclodextrin (MUA-CD), also conjugated with the LMP acts as the matrix for doxorubicin (Dox) loading. The HA ligand has specific binding towards the CD44 receptor that is overexpressed on the cell surface of a broad variety of tumors. After entering tumor cells, the acidic cellular environment triggers the fusion of ligand-modified LMPs by destructing the oxidized shell. Dox accumulates in the nucleus and contributes to high cytotoxic activity for killing cancer cells.

To overcome the high surface tension of pristine LMs for patterning, various organic microparticles (e.g., Al_2O_3, MoS_2, BN nanosheets) have been mixed with LMPs by mechanical stirring or simple ball milling to increase their rheological viscosity [94–96]. As LM fractions increase, the corresponding Al_2O_3/LM composite changes from the power to semi-solid putty and then to a liquid state (Fig. 2d-i) [95]. When the LM content is low, the organic microparticles are partially coated with LMPs, showing discrete distributions. Full or excessive LM encapsulation after increasing LM contents forms interconnections between microparticles, leading to the transformation to the putty or liquid-like state. X-ray photoelectron spectroscopy (XPS) of the pristine LM and LM/Al_2O_3 composite reveals the existence of coordination bindings between the Ga atom in LMs and the O atom in Al_2O_3 microparticles, manifested by another peak at ~530 eV (Fig. 2d-ii). The lone electron pair of O atoms can be transferred to the empty orbit of Ga to form a coordination bond. In contrast, carbon-based materials such as graphene nanoplates and carbon nanotubes cannot form a uniform composite with LMs due to the lack of lone pairs to activate this reaction. The improved rheological viscosity of LMs by incorporating organic microparticles allows their simple patterning on stretchable elastomeric substrates.

Compared with the pristine Ga core, the outer oxide shell of LMPs is easier for chemical modifications by forming covalent bonds either at the Ga or O site. The preparation of LMP-based functional composites requires stable dispersion in solvents. Tannic acid (TA) has a large amount of phenol functional groups that can form coordinate bonds with Ga_2O_3. The formation of a core-shell structure helps stabilize the LMP dispersion (Fig. 2e) [97]. The size of obtained LMPs in the dispersion fabricated by sonication decreases with increasing TA concentration. By leveraging the noncovalent self-assembly of LMPs and constitutional polymer matrix, a convergent synthesis strategy is adopted to prepare an LMP-based multifunctional hydrogel with good conductivity, stretchability, and self-healing capability. As an emerging organic-inorganic hybrid system, the LM-polyphenol network combines the powerful antioxidant, anti-inflammatory, antibacterial, and hemostatic properties of natural polyphenols with the pro-vascular, osteogenic, pro-repair, and broad-spectrum antimicrobial properties of metal ions [98]. The good anti-microbial activity and biocompatibility of the LMP-based multifunctional hydrogel lead to its applications in wound healing and subcutaneous injection for bioimaging, including MRI and CT scans.

In most cases, the LMP in the dispersion undergoes morphological transformation and settlement at elevated temperatures due to dealloying and the formation of Ga oxide monohydroxide (GaOOH) [99]. The specific polymer coating on the surface of LMPs promotes their stabilization in the solvent and introduces stimuli-responsive morphological transformation. Since the uptake of nanomaterials by cells is shape-dependent, the stimuli-responsive morphological transformation of LMPs implies great potential in tumor therapy and imaging [100]. Meanwhile, the morphological transformation can be leveraged to puncture drug-carrying capsules or merge LMPs to allow controllable drug delivery [101]. In a representative study, dopamine is used to trigger light-induced shape transformation by exploiting the photothermal effect (Fig. 2f) [102]. By adding 2-amino-2-(hydroxymethyl)-1,3-propanediol to the suspension, dopamine molecules undergo self-polymerization to form polydopamine (PDA) coated on LMPs. PDA has a broad absorption from ultraviolet to near-infrared (NIR) region with high photothermal conversion. After 20 min irradiation of NIR light, the temperature of LMP increases from 26.8 to 36.3 °C. As a result, LMPs undergo the dealloying process and trigger a thermal-induced morphological transformation from a spherical to an ellipsoidal shape due to the formation of gallium oxide monohydroxide (GaOOH) rods [84]. EDS mapping reveals a uniform distribution of Ga and In across the inner core of spherical LMPs. O accumulates on the outer layer of the inner core, which indicates the formation of gallium oxide. After changing to an ellipsoidal shape, Ga and O are dispersed all over the LMP with diminishing In. These results confirm the dealloying of Ga and the formation of GaOOH of LMPs under NIR irradiation. More complex morphological transformations from a spherical shape to a rod or rice shape under thermal stimulus have also been demonstrated [103]. The photothermal conversion is also possible in core-shell LMP with densely packed reduced graphene oxide (rGO) as the shell [104]. A large thickness of the rGO shell significantly boosts the photothermal conversion efficiency of Ga-based LMPs (Ga@rGO) to 42.4%, which is higher than 32.6% for barely Ga NPs and 22.1% for the commonly used photothermal gold nanorods. Due to the high photothermal conversion and thermal expansion coefficient, the injected Ga@rGO serves as a suitable photoacoustic (PA) material for bio-imaging and cancer detection. With the same amount of injection,

Ga@RGO exhibits a PA signal that is more than 3 times stronger than Ga NPs and gold nanorods.

The intrinsic oxide shell of LMPs prohibits the formation of conductive patterns, which has been a main challenge in the fabrication of LM-based electronics. Mechanical sintering is the most widely used method to break the oxide and activate LMPs. In order to facilitate the mechanical sintering process, LMPs are modified with an acrylate polymer to form highly cross-linked particle networks comprising >99.9% LMs by weight (Fig. 2g) [105]. The enhanced interaction between LMPs helps rapture the oxide shell upon stretching. As a result, the conductivity of the polymer/LM network increases from 2500 to 20000 S/cm under 700% stretching, which is opposite to the trend of conventional conductors. Meanwhile, the resulting network provides epidermal sensors and circuitry with high stretchability and mechanical fatigue resistance. However, the electrical conductivity of the LMP-based composite activated by mechanical sintering is inconsistent due to poor control of the dynamic rupture process and also limited by the maximum stretchability of the polymer matrix. To achieve enhanced conductivity while maintaining great conductivity stability, a chemical doping that introduces hydrogen to the oxide surface by ultrasonication in the presence of aliphatic polymers directly renders the oxide layer conductive (Fig. 2h-i) [38]. Poly(ethylene-co-vinylacetate) (PEVA) undergoes C-C homolytic cleavage to form primary carbon radicals (~C-C$^{\bullet}$) during sonication, which combines with free radicals from dicumyl peroxide (DCP) to form the secondary carbon radicals (~C-C$^{\bullet}$-C~). Afterward, the secondary carbon radicals transform into alkenes and hydrogen radicals (H$^{\bullet}$). The hydrogen radical donates free electrons to oxygen, resulting in the change of the electronic structure and electrical conductivity of Ga_2O_3, as verified by the XPS analysis (Fig. 2h-ii). The conductivity of printed LMP lines is comparable to that of conventional metals (25,000 S cm^{-1}), with excellent electromechanical decoupling, scratch resistance, and long-term stability upon deformations. Notably, the conductivity of modified LMPs depends on the hydrogen doping level, which is ultimately determined by the ethylene weight fraction (Fig. 2h-iii). Compared with the mechanical sintering process, the hydrogen-doping strategy offers better and more consistent control of the conductivity of LMPs.

As aforementioned, the existence of the oxide layer increases the wettability of LMPs on various substrates, which has been leveraged in LM patterning. However, the sticky oxide layer adheres to the channel walls of microfluidic devices to result in residuals. After the removal of the oxide shell, LMs tend to alloy with metal electrodes and cause embrittlement. Therefore, it is essential to reduce the wettability of LMPs while maintaining the oxide intact. Efforts to address this challenge led to the modification of the oxide shell of LMs with phosphoric acids [106]. Due to hydrogen and covalent bonding interactions, the 1-decylphosphonic acid (DPA) self-assembled on LMs forms a hydrophobic layer. The DPA-modified LM can pass through the capillary channel without leaving residues. In addition, this modification method provides a reversible electrical contact between LMs and metal electrodes for applications in reconfigurable electronics.

4. Patterning of LMs for stretchable electronics

LM patterning is an essential step in the fabrication of LM-based stretchable electronics [107]. Due to the fluidity, LMs can be patterned by a variety of ink-based printing techniques, including 3D printing, microfluidics, infiltration, inkjet printing, stencil printing, and transfer printing, depending on the rheological properties of LMs or LM-based composites and their adhesion to diverse substrates. The adhesion of the substrate can also be programmably modified with a seed layer for LM patterning. Laser pulses can selectively activate LMPs by rupturing the oxide layer as an effective top-down fabrication method. Loading LMPs with magnetic particles enables LM patterning with magnetic fields. An overview of diverse LM or LMP patterning techniques is provided in Fig. 3.

4.1 Patterning of pristine LMs

Microchannel technology is one of the most straightforward and well-developed methods for LM patterning, which typically involves three steps: preparation of microfluidic channels, LM injection, and sealing [108, 109]. Microfluidic channels are often obtained by standard replica molding from a template fabricated by laser scribing, 3D printing, or photolithography. Next, LMs are injected into microfluidic channels by a syringe or using vacuum pumping. Due to the high surface tension of LMs and the high yield strength of the oxide layer, high pressure is needed during the injection as described by the Laplace equation, especially for narrow channels. In a typical experimental setting, microfluidic channels are equipped with another outlet to facilitate air release. By leveraging the ultralow evaporation of LMs, a hand-free vacuum injection technique is developed to help air release without outlets. After dropping LMs over the inlet, the microfluidic channel is placed in a vacuum box for ~ 20 mins. After releasing the vacuum, LMs are forced to flow into microchannels by atmospheric pressure. The smallest channel that can be filled by this technique reaches ~ 5 μm [108]. Based on vacuum injection, large-sized complex 3D LM structures can be realized by exploiting dissolvable templates with porous structures [110]. By hot-pressing sugar particles in a humid environment, a porous sugar template with a desired shape is first fabricated (Fig. 4a) [111]. After immersing in LMs in a high vacuum for 60 mins at room temperature to infiltrate LMs, dissolving the template in ice water maintains the solid state of LMs. After rinsing with ice water several times, the 3D LM structure is then immersed in Ecoflex precursors at 0°C, followed by vacuum pumping to facilitate the infiltration of Ecoflex. The cured Ecoflex serves as an encapsulation for the 3D LM to maintain its structural integrity.

The utilization of high pressure or vacuum during LM injection requires microchannels to have sufficient mechanical strength to avoid deformations or collapses, resulting in the use of stiff and thick elastomers. In order to thin down the LM-based microfluidic device, a novel 3D printing technique is employed to fabricate microchannel walls with small dimensions on a thin Ecoflex layer supported by a rigid glass substrate with a sacrificial PVA layer (Fig. 4b) [112]. After laminating another thin elastomer and the reinforcing PVA layer, LMs are pumped into the microchannels with a syringe. After sealing the inlet and outlet, an ultrathin stretchable NFC device based on LM microfluidic can be obtained by dissolving the sacrificial and reinforcing PVA layer. Due to the small thickness (~ 7

μm), the obtained NFC device with an adhesive polydopamine coating can be conformally attached to wet biological tissues and exhibits stable RF powering performance under severe deformations. For 2D or 3D LM structures fabricated by either microchannels or porous templates, the encapsulation prevents straightforward integration with electrical components for extended functionalities. To address the issue, a plasma-treated polydimethylsiloxane (PDMS) layer with temporary and reversible adhesion to PDMS microchannels is employed for sealing. After the injection of LMs, the PDMS microchannel is peeled off manually from the solidified LM on a cold plate. The encapsulation-free LM pattern allows for direct integration with electrical components [113].

Considering its flowability, direct 3D printing or inkjet printing seems like an easy and plausible way to create LM patterns [114–118]. However, direct 3D printing of LMs is challenging due to a couple of factors, including the high surface tension and low viscosity of LMs, as well as the high yield stress of the oxide layer. However, the newly formed oxide layer on the surface of extruded LMs can be leveraged to directly print and form complex 3D LM structures. After extruding from a syringe, an oxide layer forms automatically on the newly exposed LM surfaces. The oxide layer not only increases the adhesion between LMs and substrates but also helps sustain the shape of LMs against gravity and surface tension. High-resolution 3D printing of LMs with fine nozzles has demonstrated the capability to create miniaturized reconfigurable or integrated circuits (Fig. 4c) [119]. The fine nozzle with an inner diameter of 5–40 μm is fabricated from regular glass capillaries by a pipette puller. During printing, the distance between the nozzle tip and the substrate is fixed to 2–16 μm and the pneumatic pressure is kept at ~30 psi. Coordinating the operation of the pneumatic pressure and the movement of the motion stage allows precise patterning of LMs with a minimum linewidth of 1.9 μm. Uniform linewidth is even obtained at the corner of the kinked or bent patterns. The smaller linewidth of LM patterns can also be achieved by increasing the printing rate. Additionally, by leveraging the rate-dependent adhesion between the LM filament and the substrate, self-supporting 3D LM patterns can be realized with three steps: printing, lift-off, and relocating. Overall, the adhesion increases with the lift-up rate of the nozzle. With a slow lift-up rate of less than 0.1 mm/s, the yield strength of the oxide layer is still able to withstand gravity and provide adhesion to hold the filament.

Due to the lack of stiffness, LMs are not able to maintain the structure without assistance from the oxide layer. However, the small thickness and limited yielding strength of the oxide layer set a limit for the printing speed and the spatial resolution of printed patterns. In addition, the applied pressure has great tunability on the morphology (e.g., necks, wires, or bulges) of printed LMs. The limited spatial resolution of printed patterns can be enhanced by 3D printing LMs inside a supporting hydrogel matrix or modifying the rheological properties of LMs. In the former approach, acrylamide/nanoclay suspension serves as a yield-stress fluid support bath and the additional hydrogen peroxide can accelerate the oxidation of LMs inside the matrix [120]. A low hydrogen peroxide concentration in the suspension leads to the discontinuity of printed LM wires due to the insufficient oxidation rate. It is observed that printing conditions such as velocity, flow rate, and nozzle size have a profound impact on the resolution and shape fidelity of LM filaments. Next, the hydrogel matrix with embedded LM patterns is polymerized under UV light. With optimized printing parameters, novel LM-based double-layered DC circuits and hourglass-shaped RF coils with

centimeter-long dimensions can be obtained. In the latter approach, the rheological property of LMs can be modified by adding metal or metal oxide particles [121, 122] or rigorously stirring to introduce more oxidate [31]. The obtained composite corresponds to much higher viscosity and lower surface energy, which can be used for printing 2D or complex 3D stretchable electronics.

Chemical modifications of elastomeric substrates present another effective means to improve their adhesion to LM or the oxide layer. LMs have good wettability on the metallic seed layer due to the alloying effect [123–125]. The Ag or Au seed layer is the most widely used in LM patterning, which can be prepared by *in situ* chemical [126], anion-assisted photochemical deposition [127], or vapor deposition such as e-beam, thermal, or plasma evaporation [128, 129]. Specific LM patterns can be obtained by selective modifications on the substrate surface with the seed layer [130, 131]. In a representative study, a dopamine seed layer is first patterned on a SEBS substrate by stencil printing. After polymerization in an alkaline solution, the polydopamine acts as the reducing agent for the deposited Ag layer, followed by galvanic replacement by copper ions. By leveraging their wettability on the Cu layer, LMs are successfully patterned on the SEBS substrate after removing the oxide layer in the alkaline environment [132]. Alternatively, the oxide layer can be directly leveraged in LM patterning. For instance, a carbon-based toner is first used to modify the substrate because its high surface roughness can reduce the adhesion to Ga_2O_3 (Fig. 4d) [133]. After printing the toner pattern on thermal transfer paper with a commercial laser printer, it is then transferred to a receiving substrate (e.g., TPU, PDMS, glass, PET) by thermal treatments. Ag-coated Cu microparticles are added into LMs to increase the viscosity and reduce the flowability. Coating the paste-like LM composite (i.e., Cu-Ag-EGaIn) onto the receiving substrate with a brush forms the targeted pattern defined by the toner. For receiving substrates with intrinsically low adhesion to Ga_2O_3 (e.g., knitted fabrics, paper, and wood), they can be coated with a thin TPU layer, followed by toner transfer printing and LM coating.

Obviously, the precision and resolution of LM patterns fabricated by selective adhesion critically depend on those of the seed layer. The smallest line width of the seed layer patterned by stencils or shadow masks is ~ 100 μm, which is not sufficient for many highly integrated devices. As a result, high-precision patterning techniques such as photo and e-beam lithography have been explored for the fabrication of the seed layer and resulting LM-based devices [134, 135]. It is worth noting that LMs cannot be patterned by photolithography directly. It is challenging to define high-resolution metal patterns on stretchable elastomer substrates by lithography due to their high thermal expansion and swelling effect. To circumvent this issue, the high-resolution pattern is first fabricated on a rigid PMMA substrate supported by a parylene-C layer and poly(acrylic acid) (PAA) sacrificial layer by e-beam lithography, combined with a soft lithography process (Fig. 4e) [134]. Next, an Au/Ti or Cu/Ti adhesive layer is deposited on the PMMA substrate with an electron-beam evaporator, followed by LM coating with a soft PDMS stamp under gentle pressing in order to overcome the high surface tension. Patterned LMs on the rigid PMMA substrate are obtained by a PMMA lift-off process in acetone. After spin coating or casting the PDMS precursor on the pattern LMs, the fabricated LM electronics are released by dissolving the PAA sacrificial layer. Subsequent dry etching of the parylene-C layer and encapsulating the backside of LM electronics with PDMS complete the fabrication process. The feature size

and line spacing of LMs patterned can reach as low as 180 nm and 1 μm, respectively, allowing for high-density integration of LM electronics. Alternatively, high-resolution LM patterns can be obtained by laser ablation of the LM and seed layer to achieve a line width and pitch as small as 4.5 and 100 μm [136]. With optimized laser parameters, the underlying PDMS remains intact during scribing, yielding a highly transparent electrode. Compared with the soft lithography, laser patterning has higher efficiency and yield.

4.2 Patterning of LM particles (LMPs)

Breaking bulky LMs down into micrometer-scale LMPs in organic solvents or polymer precursors to form a printable or sprayable composite is the simplest and most widely adopted method in LM patterning [137]. LMPs can be prepared by shear mixing or tip sonicating [138, 139], with a smaller LMP size obtained from the latter due to its higher power density. The obtained LMP composite can be patterned on stretchable substrates through inkjet, screen, or stencil printing, depending on its viscosity and stability. For example, when a low viscous solvent (e.g., DI water, ethanol, and IPA) is used, the as-fabricated LMP composite has low surface tension and can be patterned on various substrates by air spraying. The LMP composite with thicker polymer precursors such as TPU [140], PDMS [141], SEBS [142], and photopolymer [143] has a high viscosity suitable for screen printing. LMPs in the printed pattern are not electrically interconnected due to the existence of the oxide layer, so an additional reactivation process is needed to rupture the oxide layer to allow the coalescence. These activation processes include mechanical [144, 145], capillary forces[146], acoustic [147], laser [148], and thermal sintering [149]. Each activation process is affected by the mechanical properties and temperature tolerance of the polymer involved and its mechanical interaction with LMPs, which will be detailed in the following discussion.

As the most straightforward and widely adopted method [150, 151], mechanical sintering explores the applied strain that is larger than the yield limit of Ga_2O_3 from pressing, poking, and scratching on the LM composite. In a representative example, LMPs with an average diameter of 1 μm are prepared by sonicating in ethanol and then mixed with poly(ethylene glycol) diacrylate (PEGDA) prepolymer (Fig. 5a) [145]. With added 2-hydroxy-2-methylpropiophenone (HOMPP) as the photoinitiator, the obtained composite is immediately cured under UV irradiation to form a solid hydrogel. LMPs in the as-fabricated composite are initially encapsulated by the oxide layer and thin insulating PEGDA. The programmable LM patterns are obtained by direct writing of the LMP composite with a cylindrical metallic bar of approximately 1 mm in diameter (commercial writing and drawing machine controlled by software). With applied force above a threshold value, the oxide layer and surrounding PEGDA network are destructed, leading to the decrease of resistance by eight orders of magnitude to form conductive patterns. Interestingly, the swelling of the PEGDA matrix upon water spray induces severe deformations and ultimate disconnections of LM conductive pathways, rendering the LM/PEGDA composite into a nonconductive state. As a result, the LM pattern can be erased and rewritten by the water-assisted swelling and mechanical rupture.

Transfer printing represents another powerful approach to fabricating and automatically activating (by the peeling-off force) LM stretchable electronics. First, LMP-based inks are

fabricated by sonicating LMs in a volatile solvent (n-decyl alcohol) and then screen-printed on a donor substrate, such as PET, glass, and paper (Fig. 5b) [152]. Polymer precursors such as PDMS and Ecoflex are then cast on patterns and infiltrated into the interspacing between LMPs. After curing, the polymer with embedded LMPs is peeled off from the donor substrate, completing the transfer printing process. The tensile stress (~ 4500 MPa) arising from peeling-off is much larger than the yield stress of Ga_2O_3, thus breaking the oxide layer to form electrically conductive pathways. The entire or partial transfer of LM patterns can be controlled by changing the stiffness and adhesion of the polymer. By reducing the mixing ratio of the curing agent for stronger adhesion and lower stiffness, fracture takes place in the polymer/LMP composite layer during peeling-off. As a result, a large amount of LMs and polymer residuals are left on the donor substrate, which allows LM patterning on a non-curable substrate (as the donor substrate). Besides transfer printing, the intentional introduction of the peeling-off process before/after stencil printing of LMPs also activates the LI-based stretchable electronics [153].

Thermal sintering of LMPs relies on heating-induced thermal expansion of microspheres to introduce the stress. An LMP ink with added thermal expansion microspheres (TEMs) is first patterned on Ecoflex substrates, followed by thermal treatments at 150°C for 5 mins (Fig. 5c) [154]. TEMs consisting of low-boiling liquid hydrocarbon encapsulated by gas-tight acrylic copolymer shells have three states as the temperature is increased: initial (10–15 μm), expanded (15–80 μm), and rapture states. The shell softens while the hydrocarbon vaporizes at 110°C, resulting in the expansion of the microspheres. With continuously increased temperature, the polymer shell ruptures as the internal pressure exceeds its maximum strain tolerance. As a result, hydrocarbon vapor jets from the microspheres at 150°C, contributing to the rapture of the oxide layer to form conductive LM patterns.

As another form of mechanical energy, acoustic waves can also be leveraged to activate LMPs (Fig. 5d). LMPs with an average size of 2–3 μm are collected from the sediments after probe-sonication in acetone for 20 mins and then mixed with TPU precursors [147]. The obtained LMP/PU ink is patterned on a PU substrate by screen printing, followed by thermal annealing at 80°C to evaporate the remaining solvents. The printed patterns on the PU substrate are fixed by a glass slice with scotch tape and placed in a glass container filled with water. A probe sonicator is then programmed to output acoustic energy with 30% power for 30 s to activate the printed LMP/PU composites. The SEM images show that small LMPs (less than 1 μm) are newly induced between large-sized LMPs in the LMP/PU composite after activation. It is believed that the acoustic energy accumulates at the LMP/PU interface due to the large difference in acoustic impedance. Even though these small LMPs are still separated, the small interspacing of 1.85 nm between them can still ensure electron hooping, according to the quantum-mechanical tunneling effect. As a result, the conductivity of the LMP/PU composite increases by 5 orders of magnitude after the acoustic activation. The deformation of LMPs is size-dependent, with large LMPs deformed to an ellipsoidal shape and small LMPs remaining intact. This ensures the unaltered electrical pathways (i.e., small LMPs) between large LMPs and ultimately the strain-resilient conductivity of the LMP-PU composite. The acoustic activation strategy can be applied to the composite with different polymers, including hydrogels, silicone elastomers, SEBS, plastics, and even photoresist (SU-8) for high-resolution patterning of LM-based composites.

It is highly desirable to combine the patterning and sintering of LMPs into a single process to afford the low-cost and scalable fabrication of LM-based electronics. Laser sintering has demonstrated its capability in achieving this goal on diverse substrates [155, 156]. The LMP dispersion prepared by a probe sonicator is coated on the substrate by an automatic and programmable air-spraying system (Fig. 5e) [155]. After solvent evaporation, a ytterbium pulsed fiber laser (wavelength of 1065 nm) is employed to write on the LMP for sintering. Laser-sintering changes the insulating LMP pattern into a conductive one for simultaneous patterning and sintering. Both the linewidth and conductivity of the sintered LMP pattern increase with the laser fluence, with negligible influence from the size of LMPs and thickness of the LMP coating. Impressively, multilayered functional LM-based circuits with interlayer isolation can be fabricated by repeating the spraying and sintering process. Laser sintering relies on stress arising from the photothermal effect to rupture the oxide layer, accompanied by phase segregation. Compared with direct thermal sintering, laser sintering causes more extensive oxide rupture and allows LM to flow and coalesce into conductive pathways [156], providing a mask-free, high-resolution, and programmable patterning method with high yield. However, the non-scribed insulating region is vulnerable to mechanical sintering and could become conductive, leading to compromised performance or even device failure in practical applications.

A semi-solid-state ink containing polyelectrolyte-attached LMPs can also be used for high-resolution nozzle printing of intrinsically conductive LM patterns [157, 158]. The intrinsic conductivity arises from a chemical sintering effect in the delicately formulated LMP ink. The inclusion of PSS in the ink modifies the zeta potential of LMPs and improves the wettability of the resulting ink. The wettability of the ink is essential for reliable and high-resolution LM patterning based on meniscus-guided thin-film deposition. The improved wettability of the ink lowers the contact angle and facilitates the meniscus formation during printing. Solvent evaporation occurs at the meniscus as the nozzle moves is beneficial to thin-film deposition for achieving high spatial resolution. Due to the incorporated acetic acid, the pH of the ink decreases as the solvent evaporates at 70°C, which facilitates the chemical etching of the oxide. This rapid meniscus-guided printing is applicable to various substrates, including VHB tape, PDMS, hydrogel, biogel, metal film, wafer, glass, and PET [157]. Although the nozzle-printed doped-LMPs show reliable intrinsic electrical conductivity and high stability, the organic solvent-based ink and the need to anneal at high temperatures for an extended period (120°C, 3 h) pose challenges on rapid manufacturing and the choice of substrates that can be used. In another work, the oxide layer on LMPs can be made conductive by doping hydrogen in the presence of aliphatic polymers to eliminate the sintering process for LMPs after printing [38]. The success of this fabrication method critically hinges on the adhesion between the aliphatic polymer and the substrate. Therefore, the focus of the current developments is still on powerful patterning techniques with high spatial resolution, low complexity, mild processing requirements, and wide applicability. Various newly-developed patterning techniques of LMs are summarized in Table 2 to highlight their advantages and limitations.

5. LM-based flexible/stretchable electronics, devices, or systems for bio-applications

The unique properties of LMs from material modification with precise patterning create application opportunities in various sensors and multifunctional, standalone stretchable systems for the Internet of Things or on-body networks. The main functionality of LMs in flexible/stretchable devices falls into three categories: passive electrical conductors (interconnects or electrodes), active mechanical sensing materials, and mechanical/electrical reconfigurable materials. Of note, the burgeoning applications of LMs in energy storage and skin-interfaced device platforms also fall into the three categories.

5.1 LM-based passive interconnects, electrodes, or ground planes

The early application of LMs stems from stretchable conductors in both the AC and DC domains. The room-temperature flowability of LMs provides them with unprecedented strain-resilient conductivities upon mechanical deformations, outperforming their counterparts based on the stretchable conductive composites with nanofillers. The electromechanical response of an LM-based microfluidic device under stretching mainly results from the geometric changes (i.e., elongation/ narrowing along the longitudinal/ transverse direction). Different from nanofiller-based stretchable composite conductors which are described by the percolation model [159], the LM-based conductor features a high electrical conductivity in a large stretching range.

The ultrahigh stretchability and low mechanical stiffness allow conformal attachments of these devices on human tissues for bio-relevant chemical sensing and bio-imaging[142, 160]. Combined with other biochemical sensing units, the LM-based epidermal bioelectronics is capable of non-invasively capturing various physiological signals under artificial movements, including glucose [161, 162], pH [163], and electrolytes [164]. For instance, the LM-based NFC stretchable circuit is combined with electrochemically modified carbon electrodes, a colorimetric sensing strip, and a PDMS channel in an epidermal patch to detect key sweat metabolites and electrolytes in a battery-free manner (Fig. 6a-i) [165]. Layer-by-layer assembling of these components is achieved by either uncured PDMS or oxygen plasma-activated interface bonding. The LM-based stretchable circuit fabricated by a simple transfer process demonstrates non-degraded conductivity under 500% stretching. The electrochemical sensors based on potentiometric measurements are fabricated by screen printing carbon and Ag/AgCl inks on a PET film for working and reference electrodes, respectively. Selective sodium and potassium ion detection relies on the coating of an ion-selective membrane on the carbon electrode. The carbon-based electrodes modified with polyaniline and GOx result in selective glucose measurements. Coating urease on a commercial pH stripe leads to colorimetric urea detection. During excise, the sweat Na^+ (or K^+) concentration measured by the epidermal patch increases (or decreases). The sweat glucose concentration increases steadily and reaches the peak 40 mins after the intake of energy bars, followed by a small decrease (Fig. 6a-ii). The measured signals from the epidermal patch are validated by the commercial sensors with high consistency. In another work, a standalone LM-based glucose sensing platform with multilayered structures on the

cotton fabric by using the PMA adhesive layer shows good mechanical robustness, enhanced comfort, and long-term stability [166].

Multiplexed or multichannel monitoring is critical for the precise evaluation of physiological conditions and bio-imaging, which often requires high-density integration of stretchable electronics from precise patterning or multilayered integrations of LMs [93, 167]. The high-density integration of piezoelectric array with LM-based stretchable interconnects provides a wearable ultrasonic device for assessing continuous, real-time, and direct cardiac functions (Fig. 6b-i) [142]. After sonicating LMs in SEBS solution and blade-coating the prepared composite ink on a SEBS substrate, laser scribing is used to obtain high-density LM patterns with the smallest linewidth of 30 μm and spacing of 24 μm. Taken together with drilled VIAs for vertical electrical connections between different layers, a high-density piezoelectric array with a pitch of 0.4 mm on a 2 cm × 2 cm SEBS substrate can generate images with high spatial resolution (1–8 mm) and signal-to-noise ratio (30–45 dB). Capable of capturing real-time M-mode echocardiography during exercise, i.e., stress echocardiography, the objective and reliable diagnosis of coronary artery diseases can be made based on the extracted left ventricular internal diameter end diastole (LVIDd) and left ventricular internal diameter end systole (LVIDs) waveforms (Fig. 6b-ii).

Surface-enhanced infrared absorption (SEIRA) can significantly enhance molecular vibration through the intensified electrical field (i.e., the hot spot) to result in high sensitivity for molecule detection [168]. SEIRA is simple to set up and can be implemented in the wearable form. Ga nanoparticles with intrinsic metallic properties and unique electronic structures have shown comparable performance with traditional nanostructured Ag and Au in surface plasmon resonance [169]. A variety of resonant nanophotonic structures with smaller gaps, such as dimer antennas and split-ring resonators, have been employed in SEIRA sensing for field enhancement and improved sensing performance [170]. However, it has been a challenge to assemble molecules on the SEIRA sensor with small planar gaps. To address this challenge, a SEIRA sensor with vertical gaps could allow target molecules to be loaded before the formation of vertical gaps. To be specific, patterned Au nanopatches with a spin-coated nanometric dielectric layer (i.e., the target molecule) on a glass substrate are placed on the LM droplet as the ground plane in the SEIRA sensor (Fig. 6c-i) [171]. It should be noted that the good flowability of LMs leads to the formation of small vertical gaps nanopatch while avoiding short circuits between the Au nanopatch and the Ga ground plane. In a proof-of-the-concept demonstration, the LM-based SEIRA sensor is able to successfully detect the v1-octa-decanethiol (ODT) molecule, manifested by the characteristic peak at ~ 2900 cm^{-1} (Fig. 6c-ii). However, no obvious characteristic peaks of ODT are observed with the SEIRA sensor with the Au ground plane, possibly due to either the damaged ODT during the deposition of the Au ground plane or the direct contact between the Au nanostrip and the Au ground plane. Most importantly, LM can be completely removed from the top Au electrode after measurements for recycling and reuse due to the low wettability of LMs on the organic molecule.

The combined high conductivity and stretchability of LMs make them suitable for stretchable RF devices. However, the higher resistivity of Ga-based LM has a larger skin depth than traditional metals such as Cu, Ag, and Au in the AC/RF domain. Therefore,

The LM-based RF electronics working at 100 MHz need to have a thickness over 26 μm (i.e., the corresponding skin depth) to get rid of the skin effect [172]. The pioneering work on LM-based stretchable RF devices includes loop and dipole antennas [173–175]. For example, an LM-based stretchable dipole antenna exhibits a well-maintained radiation efficiency of >95 % for 50% stretching [175]. Also, the resonant frequency is inversely related to the dimension, resulting in decreased resonant frequency upon stretching and tunable radiation properties by mechanical deformations. To achieve the strain-insensitive resonant frequency, additional structural design needs to be performed to mitigate the mechanically induced detuning effect [176]. In recent work, the LM-based metasurface in a microfluidic network beneath a high-performance wearable slot antenna helps reduce resonant frequency shift to 3.23% from 3.40 to 3.51 GHz upon 30% stretching, maintaining an operational band from 3.3 to 3.6 GHz (Fig. 6d-i) [177]. Compared to previously reported stretchable dipole [175] or microstrip antennas[178], the resonant frequency of the LM-based antenna in this work shifts to the opposite direction by a much smaller value upon stretching. Unlike the straight dipole antenna, the slot antenna is less sensitive to mechanical stretching. The opposite shift of resonant frequency is attributed to the elongation of gaps between unit cells, other than the slot antenna itself. The resonant frequency also remains almost unchanged when conformally placed on various human parts, including the chest, arm, stomach, and thigh (Fig. 6d-ii). The LM-based metasurface can also greatly mitigate the degradation arising from the lossy human tissues for improved radiation performance to achieve a high gain of 5.08 dBi for 30% stretching (Fig. 6d-iii).

Combining the excellent electromagnetic interference (EMI) shielding and heating transfer properties of metals [179–183] with mechanical pliability, LMs can be used as coatings for stretchable electromagnetic shielding and thermal interface materials. Without the need for patterning and integration, it is convenient and straightforward to use LMs directly. Fabricated by infiltration from a porous sugar template, an LM/polymer composite with an interconnected 3D conductive network [111] exhibits a much better combination of EMI shielding efficiency (SE) (40–80 dB) and mechanical softness (<0.1 MPa) in a broad frequency range from 2.65 up to 40 GHz than other nanofiller-based composites, including graphene nanoplates, carbon nanotubes, and $Ti_3C_2T_x$. The conductivity and EM SE also increase with tensile strain up to 400%, possibly due to the densification of the 3D network upon stretching. Achieving high SE at a small thickness is challenging, so new materials and design strategies are needed. Although nanometer-thin MXene films have shown excellent EMI SE, lack of stretchability restricts their applications [184]. Efforts to address this challenge have led to a stretchable multi-layered graphene-LM nanocomposite with an ultrathin thickness (33 μm) and extremely high EMI SE (~ 80 dB) (Fig. 6e-i) [185]. Graphene and rGO have been reported to exhibit excellent EMI SE [186]. LMPs with an average size of 646 nm prepared by probe sonication are mixed with graphene oxide (GO) sheets with a lateral size of 1040 μm to form a stable dispersion. After vacuum filtration to obtain a thin GO/LM film, GO is reduced to rGO by thermal annealing at 800°C for 2 h followed by dip-coating with a thin PDMS layer to complete the fabrication of slippery rGO-LM (S-rGO-LM) composites. The resulting thin S-rGO-LM composite exhibits excellent EMI SE (> 70 dB) due to multiple reflections of rGO and dipole polarization at heterogeneous rGO/LMs interfaces (Fig. 6e-ii) even in harsh environments (e.g., at extraordinarily low or

high temperatures and in corrosion solutions) and upon cyclic mechanical deformations. As a result, EM energy is effectively dissipated in the form of thermal energy due to the ohm loss and polarization relaxation.

LMs and LM-based composites are also excellent passive cooling materials for thermal management, which fall into three different categories: thermal interface material (TIM), phase change material, and heat transfer fluid [187]. Among them, LM-based TIM is most extensively studied in flexible/stretchable electronics. The aforementioned LM/polymer EMI composite also has high thermal dissipation efficiency for TIM with in-plane and out-plane thermal conductivities of 4.25 and 4.05 $Wm^{-1}K^{-1}$ under 60% compression, which is about 8.3 and 7.9 times greater than that of the undeformed (0.51 $Wm^{-1}K^{-1}$) [188]. Non-metallic particles (e.g., GO, diamond, graphite, and silicon carbide) above a critical size and lacking surface roughness can also be incorporated into the fluidic LM to create highly deformable LM-based functional paste with high heat dissipation. Used as coatings or seals at the interface, the LM-based GO putty shows a temperature-dependent and reversible morphology from a porous structure to a viscous solid due to the reduction and oxidation between GO and rGO. Outstanding high thermal conductivity in the perpendicular direction ($10.5 \pm 2.3 W\ m^{-1}\ K^{-1}$) is achieved due to the synergic contribution from LMs and rGO. Even higher values ($104.5 \pm 2.7\ W\ m^{-1}\ K^{-1}$) can be realized by replacing GO with more thermal-conductive diamond particles [96].

5.2 LM-based flexible/stretchable mechanical or motion sensors

Different from electrical interconnects, stretchable strain sensors need large electromechanical responses to accurately measure strain values.[21, 189–192] The electromechanical response of microchannel-based LM stretchable strain sensors arising from geometric changes upon stretching can be described as [193]: $\Delta R/R_0 = \varepsilon^2 + \varepsilon$, giving a gauge factor of 3 under 100% stretching. Combining the LM with Ag film as the “brick” and “mortar” in a hybrid strain sensor increases the gauge factor due to the high sensitivity of Ag film (Fig. 7a-i) [6]. LMs blade-coated on PDMS with Cr/Cu as the adhesive layer in hydrochloric acid solution are first patterned into separated cells with a pulse laser. An Ag film deposited on the pattern sample with electrical wiring on both sides promotes crack formations during stretching, whereas the separated LM cells are crack-free, preventing unfavorable continuous LM pathways (Fig. 7a-ii). The resulting strain sensor exhibits 2 orders of magnitude higher sensitivity over a wide working range of >85% (Fig. 7a-iii), capable of detecting small and large bending deformation at the elbow joint. Other structural designs such as a winded LM structure wrapped around a high-elastic-modulus rectangular elastomer prism can also boost the sensitivity. Upon stretching, the localized strain occurs at the contact point between LMs and the prism to dramatically shrink the cross-sectional area, leading to a 400-time increase in the sensitivity in the proposed 3D LM-strain sensor compared with its 2D counterpart [194].

Exploring novel knotting structures can also amplify the local deformations for high-sensitivity LM-based piezoresistive pressure sensors [195]. LMs encapsulated in a thin silicone tubing go through cross-sectional narrowing upon pressure to result in increased electrical resistance according to the ohm law (Fig. 7b-i). Simply tying knots on the LM-infused

catheter can further achieve a large change in electrical resistance upon small pressure. The resulting sensor exhibits a high sensitivity of (2.4 kPa^{-1}), good linearity ($R^2 > 0.985$), and low-hysteresis (<0.5%) over a large pressure range from 0 to 50 kPa (Fig. 7b-ii). With a knotted series combining spatially distributed pressure-insensitive and sensitive regions, the knotted LM catheter can be implemented in three different modes (according to the specific application requirements such as the implementation complexity or the capability of spatial and multiplexed mapping) to effectively map the pressure distribution (Fig. 7b-iii). The LM-infused knotted catheter with the mode-3 configuration (for both spatial and multiplexed pressure mapping) measures gastrointestinal (GI) motility in multiple anatomic sites of the GI tract of anaesthetized pigs (Fig. 7b-iv). The LM-infused catheter in an 8-channel ribbon-shaped mamometry device evaluates the oesophageal pressure during the passage of artificial food bolus attached to the tip of an endoscope and the rectoanal pressure during rectoanal inhibitory reflex (RAIR). After insertion into the oesophagus via the oral route, the mamometry device captures the food swallow retention process and the simultaneous pressure events due to the presence of two boluses. Compared with commercial GI manometry devices, the LM-based one features low-cost, disposable, portable, and simple implementation, which is crucial for less developed regions or non-hospital settings.

On the other hand, extensive efforts have also been devoted to improving the strain-resilient properties of LM-based electronics over a large strain range. Most of them rely on the structural engineering of the 2D or 3D LM conductive network to allow for the reorganization and rebuilding of conductive pathways [16, 111, 196–198]. In a representative study, a uniform LM coating on a porous TPU substrate (a water-on-net structure) leverages the rotation and reorganization of TPU fibers and the self-adaptable interface between the fiber and LM to accommodate the tensile strain. It maintains conductive pathways and a small resistance change of 5% upon 100% elongation [197]. Structural engineering can be applied to LM-based devices on the microscale to improve strain-insensitivity. Depositing LMs on an Au-coated silicone substrate with a kirigami design allows the LM-based elastic kirigami electrode (LM-eKE) to unfold itself like a spring upon stretching (Fig. 7c-i) [198], leading to improved maximal elongation (820%) and enhanced strain resilience (increased electrical resistance by 33% upon 820% stretching). Interconnecting a crack-based touch sensor with the strain-insensitive LM-eKE in a smart glove accurately detects deformations on the fingertip (Fig. 7c-ii), such as the grip of a tennis ball with different finger positions. Compared to nanocomposite-based stretchable interconnectors, the intrinsic flowability of LMs features stable electric stability upon mechanical mismatch at the interconnect interface. However, since the strain-resilience originates from kirigami structures, these strategies may be not suitable for fabricating LM patterns requiring small feature sizes and high compactness.

Besides low sensitivity, LMs-based stretchable mechanical sensors also face challenges in poor dynamic response and hysteresis effect. Although some studies leverage the transient deformed state of LM [199], more efforts have been devoted to mitigating the hysteresis effect, including structural or chemical engineering of microfluidic channels [106] and formulating LM-based composites as the sensing material [200]. The key idea of these strategies is to enhance interactions between the substrate and LM or increase the viscosity of LMs. For example, shear stress introduced by wavy microchannels could restrain viscoelasticity

during the unloading cycle to result in low hysteresis [21]. Chemical modifications of LMs and microchannel walls to mitigate their interactions can further reduce the hysteresis in strain sensing [106]. Considering the small temperature coefficient of resistance of metals (~ 0.5% $^{o}C^{-1}$) and temperature variation of human bodies (< 4°C), the resulting resistance change of LM-based electronics is much smaller than that from the deformation. Therefore, temperature change has a negligible influence on mechanical sensing accuracy. When the temperature change covers the phase transformation threshold, the mechanical sensing performance of LM-based devices exhibits strong temperature dependence. This is because the state of LMs (i.e., the liquid or solid state) in the polymer matrix greatly affects the deformation distribution. In another representative work, the phase change of LMs has been leveraged in reconfigurable pressure sensors to obtain dual modes (i.e., the low and high sensitivity) [201]. However, the switch between the low and high-sensitivity mode is achieved at a significantly low temperature due to the supercooling effect [202], which is challenging to be triggered by the body temperature change, especially in a reversible manner.

The high surface tension, good flowability, and conductivity of LMs also open up application opportunities in posture and inertial motion detection. The most widely used strategy is to explore the connection or disconnection between two electrodes by the free-moving LM drops under gravity [203]. A representative title sensor uses eight pairs of laser-induced graphene (LIG) electrodes with circular distribution patterned on a PI thin film and then transferred to a PDMS substrate [204]. After texturing the PI/PDMS substrate to further reduce its adhesion to LMs, the injection of a Ga droplet with optimized volume into the cavity using a syringe is followed by sealing with a PDMS cap. The position of LMs inside the cavity caused by tilting triggers the on-off state of LIG electrode pairs. The smart diaper with an integrated LM-based tilt sensor accurately captures standing and sleeping postures on the back, side, and stomach of five babies. The same principle is also used in the LMs-based inertial motion sensor for real-time wireless monitoring of movement patterns and control of a robotic arm [205]. The LM droplet modified with LIG particles improves mobility and avoids residuals in a PDMS cavity, which rolls to the left (or right) along a LIG electrode with interdigital configurations to increase (or decrease) the overall resistance (Fig. 7d-i). The movement of the LM droplet over a planar surface is governed by friction between the LM and the channel surface along with air damping, according to Newton's second law: $ma = md^2x/dt^2 + b^{dx}/_{dt}$, where m is the mass of the droplet, a is the applied acceleration, x is the displacement, and b is the damping coefficient. The use of a circular channel in the inertial motion sensor allows quick restoration of the LM droplet for dynamic measurements.

In this case, the droplet movement can be expressed as $ma\sin(2ft)\cos\left(\frac{x}{R}\right) = m\frac{d^2x}{dt^2} + b\frac{dx}{dt} + mg\sin\left(\frac{x}{R}\right)$, where g is the gravity constant, R is the radius of the circular channel, and f is the stimulating frequency. The assembled two-axis inertial sensor can detect the acceleration along the x or y-direction with negligible interferences (Fig. 7d-ii). The on-body standalone sensing platform integrated with two inertial motion sensors (one for horizontal and the other for vertical movements) allows real-time monitoring of physical activities, including walking, jogging, jumping, and laying

down. When attached to human arms, the inertial motion sensor can be utilized to actuate the robotic arm to complete the grabbing task (Fig. 7d-iii). Different from widely used wearable strain/pressure sensors [206], the inertial momentum sensor can be applied on locations without severe deformations.

While it is challenging to achieve high sensitivity over a wide working range [207–209], room-temperature phase transformation of LMs can provide a simple switch between two different modes (i.e., highly sensitive or wide working range) as reconfigurable devices. In a representative study, Ga-based LMs can switch from a stiff to soft substrate as the working temperature increases from below to above its melting point [210]. The localized strain at the interface between the solid LM and soft elastomer leads to high sensitivity as a result of the cut-through crack formation in the sensing layer. Melting the LM through joule heating results in reduced interfacial mechanical mismatch and uniformly distributed cracks to provide a wide working range. The same design principle is also applied to result in a flexible reconfigurable capacitive pressure sensor [201]. The reconfiguration results from the Ga microgranules-based separation layer between two flexible electrodes. The separation layer features a core-shell structure with Ga droplets encapsulated by PDMS, which is prepared by a T-junction microfluidic device fed by liquid Ga and PDMS precursors from two inlets, with the feeding rate controlling the size and core/shell ratio. The rigid/soft switch changes the mechanical stiffness of the separation layer by more than 611 times. As a result, the pressure sensor can measure both large loads (e.g., human weight, foot pressure, and acupressure) in the rigid mode and subtle pressures (e.g., the carotid artery pulse and insect movements with a pressure of only 3 Pa) in the soft mode.

The captured body gestures or movements from various LM-based physical (e.g., strain) sensors promise applications in human-machine interfaces [205, 211–213]. For example, the motion of human fingers captured by highly linear LM-based strain sensors in a smart glove is wirelessly transmitted to robotic fingers for real-time control [193]. LM-based capacitive sensors also enable non-contact sensing based on the dielectric constant change induced by the vicinity of objects for manipulation, smart identification, and trajectory monitoring. Patterning LMs into interdigital electrodes on electrospun PVA film as the capacitive sensor and arranging four sensors into an “arrow key” configuration results in a wireless car control system to control the movement of a toy car or play video games [214].

5.3 LM-based smart, electrically reconfigurable flexible/stretchable devices

The room-temperature phase transformation in LMs-based mechanically reconfigurable devices is mainly achieved by external heating modules [210], which need extra control and lack self-adaptness or smartness for operation. Efforts to address these challenges exploit the self-heating effect and the interplay between the mechanical and electrical properties of LMs. For instance, combining the Field’s metal particle (i.e, eutectic tin–bismuth–indium) with spiked Ni microparticles in PDMS as a stretchable hybrid elastomer (FMHE) (Fig. 8a-i) offers tunable electrical and mechanical properties, as well as the interplay between them (Fig. 8a-ii) [215]. The spiked Ni particles increase the separation between LMPs to result in higher initial resistance, which decreases dramatically upon compression (more than 4 orders of magnitude) with the LMP in a solid state at 25°C in $FMHE_3$ (Ni/PDMS

mass ratio of 3:1). The large change and high strain sensitivity result from the spike shape that facilitates the formation of conductive pathways under deformation. Compared with the one without spiked Ni (i.e., $FMHE_0$), $FMHE_3$ exhibits opposite piezoresistive responses under stretching, which is attributed to the hybrid conductive pathways induced by spiked Ni microparticles. Melting of LMPs at 80°C decreases the electrical resistance of $FMHE_3$ upon both compression and stretching, manifesting a lower electromechanical response. Therefore, $FMHE_3$ shows a switch from a low (with solid LMPs) to a high (with fluidic LMPs) resistance state during the phase transformation of LMs. Attributed to the supercooling effect, the resistance curve of $FMHE_3$ does not coincide during a full heating-cooling process under 10% compression and the resistance becomes higher than the initial value because of the conserved deformation of LMPs during solidification, leading to resistance hysteresis. Changing the environment temperature or exploiting the self-heating effect to trigger the phase transformation of LMs also varies the mechanical stiffness of the composite by ~ 3 times. Under a constant bias, the increasing applied strain decreases electrical resistance and increases the current and resulting heating power. After reaching the critical strain, the LMP starts to melt to trigger the phase transition, leading to the recovery of the high resistance to avoid overheating. The critical strain is inversely related to the applied bias. The self-heating effect can also correlate the reconfigurable electrical with mechanical properties. As a proof-of-concept demonstration, the $FMHE_3$-based compliance compensation unit can bend to prevent damage to servomotors from excessive torque by self-heating-induced softening for buffering when a robotic manipulator is blocked (Fig. 8a-iii). As the constant bias increases from 0 to 5 V, the $FMHE_3$ softens at a critical bending angle of 5° to increase the compensation angle from 7.3° to 16.5°. In another scenario, the compression of the $FMHE_3$ fits it in a trapezoidal groove with a controllable size and also adjusts its initial resistance and fusion current in a smart current-liming fuse (Fig. 8a-iv). Different from the traditional fuse for one-time use, the $FMHE_3$-based one features unique reusability enabled by reversible and resettable resistance change.

Although the mechanical deformation-induced reconfigurability has spurred the development of the LMs-based stretchable RF devices [216], they are often associated with a slow response. Possible solutions include the use of LM-based microfluidic devices to change the dimension of radiation units and LM distribution in microchannels with syringe pumping or electrical actuation, which can also modulate the other RF properties such as polarization and gain. The acid or alkaline electrolytes fed from different inlets from LMs remove the oxide residuals on the wall of microchannels during manipulation. The electrical actuation is based on a surface-tension gradient that generates Marangoni forces to attract LMs toward the anode, whereas straightforward mechanical pumping often needs bulky equipment and has high power consumption.

Consisting of L-shaped units that have one LM input and two HCl inputs/outputs with two LM/HCl interfaces, the reconfigurable metasurface exhibits a broadband multifunctional polarization and large angular tolerance of incidence (Fig. 8b-i) [217]. The LM in the two arms can be changed symmetrically or asymmetrically by separate pumping. The symmetric L-shaped resonator exhibits two orthogonal resonant eigenmodes when the incident electric field is along or perpendicular to the symmetric axes of the structure (Fig. 8b-ii). The polarization of the reflected EM wave is determined by the magnitude and phase

difference of the two eigenmodes. With a symmetric resonator, the reflected EM wave has no *x*-component ($\Delta R = -1$) for the arm length within the range of 1.5–2.2 mm, which means that the polarization converter acts as a perfect reflector. Increasing arm length to 3 mm increases ΔR from −1 to 0 with $\Delta\varphi$ fixed as $\pi/2$, realizing the linear-to-elliptical polarization conversion. A linear-to-circular polarization conversion is achieved for an arm length ranging from 3.3 to 4.8 mm. A linear, circular, or elliptical reflected EM wave can be realized by simply changing the length of LM arms. Reconfigurable radiation patterns have been demonstrated in the Fabry–Pérot antenna and dipole antenna by selectively pumping the LM into microchannels [218]. The integration of LM components in a Thz waveguide allows control of the power flow such as a reconfigurable directional coupler, as the existence of LMs between the two waveguides changes the electromagnetic coupling between them [219]. By arranging three reconfigurable directional couplers in series, the input power threshold for a specific output port to reach error-free performance can be modulated by as large as 6 dB at 0.1 THz, which demonstrates the great potential of LM-based reconfigurable device in active THz communication modulations.

The interaction of the LM with solid metal in reconfigurable electronics may impede the movement of the LM or cause damage to metal circuits, so the liquid-liquid contact is preferred in reconfigurable RF electronics. A Laplace barrier can be used at the interface to facilitate the merge and separation of LMs [220]. A large pressure threshold is needed to pump LMs into the barrier at the narrowed microchannels for a controllable switch. Once LMs merged, the circuit remains closed even after the pressure release. The off-state of the switch is achieved by applying a negative pressure to retract LMs and replacing LMs with NaOH in the barrier. Another issue in LM-based reconfigurable electronics is that the LM recovers to its equilibrium shape to minimize its free surface energy upon removal of the applied bias voltage, so it is difficult to maintain a nonequilibrium deformation without the bias. Geometric modifications of the microchannel could provide a metastable locking effect to eliminate the need for a continuous DC bias and the recovery of LMs can also be achieved by simply applying a reverse bias [221].

The flowability of LMs is also directly related to their self-healing properties, as damaged LM patterns tend to coalesce after removing the oxide layer with mechanical sintering to recover the electrical conductivity [216, 222, 223]. The self-healing LMs are often combined with the specific supporting polymer either acting as a substrate [216, 222] or forming a composite with LMs [223, 178] to yield the self-healing electronics. These polymers feature a large quantity of non-covalent interactions, including hydrogen bonds, metal-ligand coordination, or van der Waals bonds for dynamic breakdown and rebuilding [224]. In a recent representative study, a hygroscopic randomly hyperbranched polymer (HRHP) synthesized by one-pot Michael addition between N, N′ – methylene diacrylamide (MBA) and 1,4-butane diamine (BDA) at a molar ratio of 1:1 provides a rapid self-healing substrate (Fig. 8c-i) [222]. The secondary and tertiary amines generated from BDA serve as branching points and chain-extending units to provide abundant dynamic hydrogen bonds. LMPs prepared by sonication can be facilely patterned on the HRHP substrate by air-spraying through a paper mask to serve as electrical interconnects or electrodes. The LM-based electronics can recover its function in 5 minutes at room temperature after damage. The ECG signals

collected from the self-healed LM-HRHP electrode show no signs of degradation, compared to the pristine one (Fig. 8c-ii). Combining self-healing with the strong adhesion of HRHP also allows the fabrication of LM-based electronics on 3D complex surfaces through the piece-by-piece assembly of the constituent parts designed by the 3D modeling and surface expansion method (Fig. 8c-iii). Self-healing between adjacent parts on a target 3D surface forms conformal LM-based electronics to measure the temperature and motion of the 3D objects for future Internet-of-Things.

LMs can also be combined with polymers as constituent components to form self-healing conductive hydrogels that can be patterned with a stencil or inkjet printing [223]. LMs not only improve the conductivity but also provide radicals to initiate the polymerization in adhesive hydrogels. The dynamic hydrogen bonding in the hydrogel network results in super-stretchability and autonomous self-healing in an ambient environment. However, the self-healing hydrogel has a lower conductivity, due to the low LM content and limited conductive pathways.

The reduced surface tension of LMs from the oxidized to reduced state in electrolytes induces a dramatic shape change, promising their use as artificial muscle for applications in soft robotics, human-machine interface, and prosthetics [74, 225]. For instance, switching the driving voltage from a positive to a negative value triggers the state change for the LM droplet placed between a pair of copper electrodes, generating substantial actuation forces in the LM artificial muscle (LMAM) (Fig. 8d-i) [226]. The actuated displacement of the LMAM with four units reaches ~ 1.1 mm under a stepwise driving voltage from −0.5 to 4 V at 0.25 Hz for a load of 1 g, with a maximum pushing and pulling force of 43 and 16 mF in one driving cycle (Fig. 8d-ii). Of note, the actuated force and displacement can be improved by increasing the number of LM droplets with parallel and series connections. The fast response of LMAM (~ 0.14 s) enables optical modulation in a reconfigurable optical reflector, with different patterns formed by the reflected light for display. Moreover, an untethered biomimetic fish with an LMAM-based single-caudal fin and embedded driving system (i.e., a Li-ion battery and a control PCB) can be actuated by LMAM on both sides to swing the caudal fin to 20° (in 0.2 M NaOH) when actuated by at 2 Hz (7.4 V) (Fig. 8d-iii). After adjusting the position and weight of the fin and hollow chamber to achieve the balanced posture, the fish can swim at an average speed of 15 mm s^{-1}, which is much faster than the speed of 0.12 mm s^{-1} in the fish without the caudal fin (driven by bubbles generated by electrolysis).

5.4 LM-based energy storage devices

Energy storage devices with mechanical foldability and pliability can improve energy density and operate upon extreme deformation [227–230]. LMs or LM-based composites are often used as stretchable electrodes in supercapacitors [231], thermoelectric generators [232], and biofuel cells [233], which exhibit stable performance under various deformations and power external sensing nodes in standalone stretchable platforms.

By converting body heat to electricity, stretchability thermoelectric generators (TEGs) can power wearable sensing nodes with improved levels of comfort and reduced thermal barriers between TEG and human skin to effectively harvest body heat and maintain high efficiency,

especially under deformations. In the stretchable TEG, the highly conductive LM elastomer composite (LMEC) can serve as both the electrical interconnects (30% LMPs with a size of 150 μm in PDMS) and TIMs (50% LMPs of 3.5 μm in diluted PDMS) (Fig. 9a-i) [141]. Except for the TE bismuth telluride (Bi_2Te_3), all other components such as the LMEC interconnect, (top/bottom) TIM layer, and (middle) thermal insulation layer can be fabricated on diverse substrates (e.g., stretchable fabric armband) by highly efficient inkjet printing. The output open-circuit voltage increases linearly with the temperature difference (Fig. 9a-ii), but it is reduced by 70% after using the fabric substrate due to the thermal barrier effect. Therefore, it is highly desirable to explore the substrate with high thermal conductivity on the hot side and a heatsink or fan to dissipate heat on the cold side (i.e., the face exposed to air).

When used in stretchable batteries, LMs may get involved in the complex chemical reaction to cause stability issues. The first LM-based rechargeable, stretchable battery introduced in 2019 is composed of an LM anode, a carbon paste cathode coated with MnO_2 slurry, a KOH/PAAm anodic hydrogel electrolyte, a LiOH/KOH/PAAm cathodic hydrogel electrolyte, and a soft elastomeric package [180]. Using EGaIn LMs as the anode material can address the issues of rigidity and dendrite formation, whereas hydrogel electrolytes avoid potential short circuits from the free flow of LMs. Applying the carbon paste and MnO_2 slurry on a pre-stretched substrate followed by releasing obtains a wavy cathode. $CaCl_2$ additives used at the EGaIn anode/hydrogel interface reduce polarization and side reactions. The rechargeable EGaIn/MnO_2 battery operates through the gallium stripping/plating and a reversible MnO_2 chemical conversion, which can operate for 100 (or 60) cycles at 0.4 (or 1) mA cm^{-2} and continuously power on-body electronics (e.g., LED and strain gauges) under 150% stretching.

Efforts to address the potential short-circuit issue have led to the use of an LMP/polyacrylamide-hemicellulose hydrogel as the anode of printable flexible batteries [138]. The unpaired electrons of Ga serve as the radical to react with the acrylamide monomer π-bonds and initiate the acrylamide polymerization (Fig. 9b-i). To obtain shear-thinning behavior for printing, carbon black additives are explored to reduce viscosity from 5789.9 to 5.2 Pa s and increase the shear stress from 76.2 to 2446.7 Pa. The conductivity of the printed composite decreases dramatically from infinity to 41.0 μΩ $square^{-1}$. Hemicellulose microparticles uniformly distributed in the composite through hydrogen bonding also avoid nonuniform polymerization caused by the sink of LMPs. The printed anode shows reversible Zn^{2+} plating/stripping, which can be attributed to the effective energy dissipation from the dynamic double-bonding network (Fig. 9b-ii). The composite also exhibits a long lifetime of over 700 hrs (up to 1500 cycles), outperforming that of the pristine Zn anode. EIS measurements indicate that the charge transfer resistance of the symmetric cell with deposited Zn (173 Ω) is much smaller than that with pure Zn (539 Ω) after 100 cycles. A full cell consisting of the composite anode and a commonly used MnO_2 cathode in an electrolyte containing $ZnSO_4$ (2 M) and $MnSO_4$ (0.1 M) also exhibits reversible Zn^{2+} plating/stripping, confirmed by the reduction and oxidation peaks at 1.15 and 1.65 V. It maintains a high capacity in the range of 238.5–118.8 mAh g^{-1} as the charging rate increases from 1 to 10 C, compared to the full cell with pure Zn anode (~125.0–50.0 $mAhg^{-1}$). The high stability of the composite and the resulting battery is first attributed to the porosity and self-healing of

hydrogels for stress dissipation and limited dendrite growth during charge/discharge cycles. Also, the corrosion resistance of LMP to the $ZnSO_4$ aqueous electrolyte could improve the stability and enhance the Zn ion transfer.

Used as stretchable hermetic seals in stretchable batteries, LMs stabilize the performance of lithium-ion batteries (LIBs) with an inner cell and outer seal against various deformations over long-term measurements (Fig. 9c-i) [234]. The fabrication of the battery cell starts with coating cathode and anode materials on stainless steel meshes, followed by wrapping with a hydrophilic porous polytetrafluoroethylene (PTFE) separator. After placing the two electrodes on a PDMS substrate and capping them with another PDMS sheet, a water-based electrolyte is injected into the cavity to complete the fabrication. The large-area stretchable seal is fabricated by vacuum-filling LMs into a PDMS chamber supported by glass beads that help avoid the collapse of PDMS sheets without loss of stretchability. The LIB with the LM-based seal does not show obvious mass change during a one-day measurement before and after 20% stretching, whereas the one without the seal has a mass loss of > 20 mg (Fig. 9c-ii). The LIB with the LM seal exhibits reversible capacity retention of 90% (or 72.5%) after 140 (or 500) cycles, but the one without decays to almost zero after 160 cycles. Moreover, the LM-sealed LIB exhibits stable output voltage and capacity under various deformations (e.g., stretching, bending, and twisting) (Fig. 9c-iii). The LM-based seal is also compatible with other types of batteries, such as the one with LM/hydrogel anodes or hydrogel electrolytes, to mitigate water evaporation and improve long-term stability and lifetime.

5.5 LM-based skin-electronics

5.5.1 LM-based adhesive bioelectronics—Skin-interfaced stretchable electronics need to have strong adhesion [235] and high gas-permeability [51] for the improved level of comfort and long-term high-fidelity physiological monitoring. The LM and widely used polymers (e.g., silicone elastomer, TPU, and SEBS) in LM-based electronics have poor adhesion and gas permeability. Although reducing the thickness can help both aspects, its efficacy is very limited, so adhesive polymers have been explored [236].

It is straightforward to coat another adhesive layer on the as-fabricated LM electronics for application on the skin, similar to commercial transfer tattoos (Fig. 10a-i) [237]. After fabricating multifunctional LM electronics layer by layer with interlayered connections on a silicone film (as the release layer), spin-coating a water-based acrylic pressure-sensitive adhesive (PSA), followed by the removal of the release layer with low adhesion, allows strong attachment to the skin. Due to the small thickness and strong adhesion, the integrated strain sensor on the skin creases can accurately detect local joint movements (Fig. 10a-ii) with higher sensitivity than others with additional glue or magic tape (Fig. 10a-iii).

The widely used biocompatible PDMS in LM-based stretchable electronics has limited adhesive strength [238], but the adhesion can be greatly improved by reducing its crosslinking density [239, 240]. Because the vinyl group reacts with the hydrosiloxane with the catalysis of Pt to form a highly cross-linked network in the curing process, the small addition of oligomers such as PEIE [240] and PEG [239] dramatically decreases the crosslinking density of PDMS due to the inhibited Pt catalyst by surrounding oligomers (Fig. 10b-i) [239].

For instance, the PDMS with 4.7 wt% PEG oligomers (molecular weight: 400) exhibits strong adhesion (1 N/m) to skins even under wet conditions, along with a reduced Young's modulus and improved stretchability (Fig. 10b-ii). LMs patterned on a donor substrate by stencil printing can be transferred printed to the as-fabricated adhesive PDMS for directly applying to the skin without inducing irritation (Fig. 10b-iii), allowing for continuous and stable monitoring of joint motion and electrophysiological signals, as well as electrical stimulation therapy for wound healing. In another work, the use of the pressure-sensitive adhesion (PSA) prepared from acrylate monomers results in transfer printed LM electronics from a release film with a surface-enriched structure composed of LMs and acrylate polymer adhesives, followed by biaxial stretching for activation [241]. Commercial off-the-shelf chips can be easily welded with transferred LM patterns to form multifunctional devices by simple pressing. The elimination of the use of heating and solvents during welding is crucial for bio-interfaced electronics.

Instead of directly fabricating LM electronics on adhesive substrates [242], a conductive LMP composite with self-healing and reversible wet adhesion can be created by delicately formulating the polymer matrix [243]. Introducing thioctic monomers (e.g., thioctic acid (TA), 5-(1,2-dithiolan-3-yl)-N-dodecylpentanamide (TA-C12) and N-(3,4-dihydroxyphenethyl)-5-(1,2-dithiolan-3-yl) pentanamide (TA-DPA) leads to covalent crosslinking with 1,3-diisopropenylbenzene (DIB). The biological catechol groups form physical crosslinking with multivalent ions (i.e., Al^{3+}), which are responsible for wet adhesion and self-healing. The mechanical properties of the as-prepared composites such as the LMP/hydrogel composite can be tuned by the covalent and physical crosslinking density. The presence of disulfide bonds, catechol groups, and carboxyl groups provides effective binding to LMPs for uniform dispersion. With the LMPs over 40 vol.%, the resulting LM composite elastomer exhibits high electric conductivity (1.3×104 S m^{-1}) and strong wet adhesion (670 kPa) for excellent and durable electromyography sensing even under large lifting forces (~ 15 N) The design principle is also applied to the formulation of the LM adhesive based on PVA [244], PAM [245], and PSA [241].

Different from the above thick LMP composite, a low-viscosity PVA/ LMP ink can be *in situ* air-sprayed through a flexible conformal mask to form thin LM-based electronics on the skin [246]. The hydroxyl group of PVA forms hydrogen bonds with the oxide layer of LM to improve the dispersion uniformity (Fig. 10c-i) and skin adhesion (Fig. 10c-ii). The crosslinked PVA enhances interactions between LMPs, which is important for mechanical sintering. The strong bonding between PVA and the keratin of the epidermis allows intact contact with the skin even after rubbing (Fig. 10c-iii), which ensures high-fidelity monitoring of electrophysiological signals with high SNRs (15 and 23 for ECG and EMG) even under deformations.

5.5.2 Highly permeable LM-based electronics—LM-based stretchable electronics with high gas permeability often leverage breathable substrates such as fibrous substrates fabricated by electrospinning [247]. Electrospinning is an electrohydrodynamic process, during which the polymer precursor is electrified to form a Taylor cone by the high voltage between a metal syringe tip and collector, followed by the generation of a stretched and thinned jet. After the evaporation of solvents, fine breathable fiberous substrates are collected by

a metal plate or rotator. For instance, fibrous poly(styrene-block-butadiene-block-styrene) (SBS) prepared by electrospinning as substrates for stencil printing of LMs yields breathable LM-based electronics (Fig. 11a-i) [196]. As revealed in SEM images (Fig. 11a-ii), uniform LM coatings transform into a mesh structure after mechanical activation, resulting in air and moisture permeability (79.5 mm s^{-1} and 724 g m^{-2}day) that is even higher than the nylon cloth (11.8 mm s^{-1} and 621 g m^{-2}day). Besides excellent gas permeability, the LM/SBS with mesh structure also exhibits strain-resilient electromechanical property (i.e., resistance increase of 18% under 1000% stretching), with oxide wrinkles on the newly exposed LMs to help release the local strain. Different from the non-breathable counterpart, the breathable LM/SBS mat does not cause skin rashes even after one week of continuous wearing (Fig. 11a-iii).

The conductivity and strain-resilient electromechanical property of the gas-permeable LM/SBS can be further improved by introducing a lyophilic Ag layer on the fibrous SBS mat to generate uniform LM patterns (LM-LAg-SBS) (Fig. 11b-i/ii) [248]. Ag coating achieved by the *in situ* chemical reduction of CF_3COOAg with N_2H_4 H_2O allows uniform coating of LM to provide the LM-LAg-SBS mat with lower air resistance and higher moisture permeability (1300 g m^{-2}day) than the above-mentioned one without the Ag seed layer (724 g m^{-2}day) (Fig. 11b-iii). Besides improved gas permeability, the LM-LAg-SBS exhibits an ultrahigh conductivity of 155,900 S cm^{-1} and a marginal resistance change by only 2.5 folds upon 2500% stretching, which can be attributed to the formation of conductive pathways along the thickness direction. The breathable LM-based electronics with fibrous TPU substrate are also reported for on-skin ECG recording and temperature management by leveraging their strain-resilient electromechanical properties. [197].

Phase separation is a simple, inexpensive, and scalable approach to fabricate gas-permeable elastomers or polymers with highly ordered porous structures [206, 249]. In a typical process, the polymer dissolved in a volatile solvent is mixed with another miscible non-solvent. During the quick evaporation of the solvent, the non-solvent separates and forms nano/microscale drops with no solute polymers, which creates uniformly distributed porous structures in the polymer matrix after complete evaporation of the non-solvent. Based on the phase separation, LM-embedded, porous soft conductors are prepared for multifunctional on-skin electronics [250]. The fabrication of porous LM composites starts with mixing LMPs with PU dissolved in THF and 1-butanol (Fig. 11c-i). By leveraging their different boiling points, the phase separation between THF and 1-butanol leads to the formation of porous structures, with LMPs self-assembled on the pore surface due to the Pickering effect. The LMPs merge to form conductive pathways after mechanical sintering with a stainless-steel roller. The porous LM/PU composite shows outstanding moisture permeability (~ 5000 $gm^{-2}d^{-1}$) due to the large pore size (Fig. 11c-ii). Meanwhile, the uniform pores also serve as a buffer to avoid LM leakage under severe deformations (Fig. 11c-iii). Although laser cutting can be employed to pattern the porous LM composite for functional electronics [251], it does not apply to small or complex LM patterns due to the limited resolution of laser patterning of elastomer-based composites, which may limit its potential applications.

6. Conclusions and future perspectives

This review summarizes the intrinsic physical/chemical properties and unique applications of Ga-based LMs in biosensors, reconfigurable devices, energy storage devices, and highly integrated standalone stretchable electronic systems. The oxide layer with high surface tension affects the wettability of LMs and also poses a challenge for precise patterning. Various surface modifications with conjugated surfactants and polymers have been attempted to tailor the reactivity, patternability, adhesion, and even optical absorption of LMs for biomedicine applications. The room-temperature phase transformation and good flowability from the liquid side combined with superior thermal and electrical conductivity from the metal side provide LMs-based stretchable electronics with unprecedented and unique mechanical, electromagnetic, electrical, thermal, and optical properties. The strain-resilient electromechanical property of LMs ensures stable connections even under severe deformations, while structural engineering and phase transformation with tunable mechanical properties can also boost its electromechanical response for strain sensing. The exploration of porous and adhesive substrates greatly extends the application of LM-based electronics for long-term skin-interfaced use.

6.1 Mechanical, physical, and chemical properties of submicron-sized LMPs for high-resolution LM patterning

Precise patterning techniques of LMs on stretchable substrates range from the conventional microchannel and direct printing methods (i.e., inkjet, stencil, or screen printing) to transfer printing and the use of a pre-patterned metal seed layer (from photolithography or EBL) with increasing spatial resolution. Till now, the high-resolution patterning of LMs based on metal seed layer relies on sophisticated etching processes and is only applicable to specific stretchable elastomeric substrates. Patterning with high spatial resolution on the submicron scale relies on deep insights into the physical-chemical and mechanical properties of LMs and LMPs, as well as their interactions with supporting elastomeric substrates (Fig. 12a). Meanwhile, it is necessary to explore the mechanical properties of submicron-sized LMPs and their interactions with various elastomeric substrates, especially those with strong adhesion and high porosity, to afford high-resolution LM patterning.

6.2 All-LM stretchable electronics with spatial-tunable electromechanical properties

Although the electromechanical properties of LMs have been pushed to strain-insensitive and strain-resilient, stretchable electronic devices often require the combination of both units in the same system (Fig. 12b). However, stretchable systems with hetero-integrations of both units are prone to electrical failures due to interfacial mismatch, so it is desirable to exploit the homo-integration of LM composites with different electromechanical properties for all-LM stretchable systems. In the all-AuNW stretchable sensor, the low strain-responsive region contributes to a stable electrical connection to external data acquisition units, whereas the high strain-responsive region is responsible for mechanical sensing at the target location [252]. As for LMs, their electrical and electromechanical properties are often predetermined by the fabrication process (often incompatible with one another). Therefore, it is vital to develop a general fabrication approach for manufacturing LMs with controllable electromechanical properties for all-LM electronics. In a recent work, inkjet printing of

LMP/silicone elastomer composites allows on-demand programming of their electrical and electromechanical properties by changing the printing speed [253]. It is found that the LMP evolves from a spherical to a needle-like microstructure with increasing printing speed, allowing for the transition from an insulator to an electrical conductor throughout a printed part. However, the spatial resolution of inkjet printing in this work is only ~ 1 mm. It is worthwhile investigating the mechanical properties of LMPs with smaller sizes and their interactions with polymer precursors in the composite ink to explore high-resolution printing.

6.3 Standalone LM-based device systems integrated with commercial chips

Despite the significant development in the preparation and processing techniques of LMs, the interconnects between LMs and commercial chips (for extended multifunctionality) remain the bottleneck for LM-based electronics. Different from soldering chips with high precision in conventional PCB or FPCB, integration in LM-based electronics is mainly based on physical contact (Fig. 12c). Therefore, additional encapsulations at connection points are needed to avoid failure from mechanical deformations. At the same time, the fluidity of LMs severely restricts the integration density of all-LM stretchable electronics. To circumvent these issues, LM-based paste is introduced to solder commercial chips with LM patterns. For example, an *in situ* welding strategy exploits a sticky conductive composite consisting of LMPs and pressure-sensitive adhesive [241]. An LM-based isotropic conductor activated by an external magnetic field [254] also allows simple integration with commercial chips. In another recent study, self-soldering and encapsulations are achieved in one step by leveraging the polymer-gel transition of styrene-isoprene block copolymers (SIS) in the LM-based composite ink and substrate [255]. Upon exposure to the solvent (i.e., toluene) vapor, SIS changes from the polymer to gel state and then cures at room temperature after commercial chips sink to connect with LM patterns to encapsulate and protect the interface. However, this strategy is only applicable to specific polymers that are compatible with LMs and exhibit polymer-gel transition induced by solvent evaporation. Moreover, the high-precision patterning techniques of LMs such as photolithography and EBL are not compatible with the soldering process in terms of the material system. Therefore, innovations in the preparation and integration of LM composites are still needed to address this challenge.

Acknowledgments

This work was supported by the Core Facility, Medico-Engineering Cooperation on Applied Medicine Research Center, University of Electronic Science and Technology of China, the National Natural Science Foundation of China under grant numbers 61825102, 62301116, 52021001, and U21A20460; H.C. acknowledges the support provided by NIH (Award Nos. R21EB030140, U01DA056242 and R21OH012220), NSF (Grant No. 2222654).

Uncategorized References

1. Kalantar-Zadeh K; Tang JB; Daeneke T; O'Mullane AP; Stewart LA; Liu J; Majidi C; Ruoff RS; Weiss PS; Dickey MD, Emergence of Liquid Metals in Nanotechnology. Acs Nano 2019, 13 (7), 7388–7395. [PubMed: 31245995]
2. Dickey MD, Emerging Applications of Liquid Metals Featuring Surface Oxides. ACS Appl. Mater. Interfaces 2014, 6 (21), 18369–18379.
3. Dickey MD, Stretchable and Soft Electronics using Liquid Metals. Adv. Mater. 2017, 29 (27), 19.

4. Li XK; Li MJ; Zong L; Wu XC; You J; Du PK; Li CX, Liquid Metal Droplets Wrapped with Polysaccharide Microgel as Biocompatible Aqueous Ink for Flexible Conductive Devices. Advanced Functional Materials 2018, 28 (39), 8.

5. Silva CA; Lv J; Yin L; Jeerapan I; Innocenzi G; Soto F; Ha YG; Wang J, Liquid Metal Based Island-Bridge Architectures for All Printed Stretchable Electrochemical Devices. Advanced Functional Materials 2020, 30 (30), 10.

6. Feng B; Jiang X; Zou GS; Wang WG; Sun TM; Yang H; Zhao GL; Dong MY; Xiao Y; Zhu HW; Liu L, Nacre-Inspired, Liquid Metal-Based Ultrasensitive Electronic Skin by Spatially Regulated Cracking Strategy. Advanced Functional Materials 2021, 31 (29), 10.

7. Li JH; Ma QQ; Gao S; Liang T; Pang YS; Zeng XL; Li YY; Zeng XL; Sun R; Ren LL, Liquid bridge: liquid metal bridging spherical BN largely enhances the thermal conductivity and mechanical properties of thermal interface materials. Journal of Materials Chemistry C 2022, 10 (17), 6736–6743.

8. He Z; Wang Y; Xiao H; Wu Y; Xia X; Li S; Liu J; Huang K; Wang F; Shang J; Liu Y; Li H; Li F; Wang S; Zhu G; Li R-W, Highly Stretchable, Deformation-stable Wireless Powering Antenna for Wearable Electronics. Nano Energy 2023, 112, 108641.

9. Choi H; Luo Y; Olson G; Won P; Shin JH; Ok J; Yang YJ; Kim T.i.; Majidi C, Highly Stretchable and Strain-Insensitive Liquid Metal based Elastic Kirigami Electrodes (LM-eKE). Advanced Functional Materials 2023.

10. Tandel R; Gozen BA, Direct-Ink-writing of liquid metal-graphene-based polymer composites: Composition-processing-property relationships. J. Mater. Process. Technol. 2022, 302, 10.

11. Saborio MG; Cai SX; Tang JB; Ghasemian MB; Mayyas M; Han JL; Christoe MJ; Peng SH; Koshy P; Esrafilzadeh D; Jalili R; Wang CH; Kalantar-Zadeh K, Liquid Metal Droplet and Graphene Co-Fillers for Electrically Conductive Flexible Composites. Small 2020, 16 (12), 12.

12. Li YD; Luo YX; Nayak S; Liu ZJ; Chichvarina O; Zamburg E; Zhang XY; Liu Y; Heng CH; Thean AVY, A Stretchable-Hybrid Low-Power Monolithic ECG Patch with Microfluidic Liquid-Metal Interconnects and Stretchable Carbon-Black Nanocomposite Electrodes for Wearable Heart Monitoring. Adv. Electron. Mater. 2019, 5 (2), 12.

13. Wang JS; Wang Y; Jue R; Li DQ; Zhao Z; Cai GM; Cheng DS; Wang X, Liquid metal/CNT nanocomposite coated cotton fabrics for electromagnetic interference shielding and thermal management. Cellulose 2022, 29 (16), 8907–8918.

14. Wang Y; Gao YN; Yue TN; Chen XD; Wang M, Achieving high-performance and tunable microwave shielding in multi-walled carbon nanotubes/polydimethylsiloxane composites containing liquid metals. Applied Surface Science 2021, 563, 11.

15. Li MX; Wu DY; Tang RY; Zhou SY; Liang WH; Liu J; Li L, Liquid metal integrated PU/CNT fibrous membrane for human health monitoring. Front. Bioeng. Biotechnol. 2023, 11, 11.

16. Yun GL; Tang SY; Sun SS; Yuan D; Zhao QB; Deng L; Yan S; Du HP; Dickey MD; Li WH, Liquid metal-filled magnetorheological elastomer with positive piezoconductivity. Nat. Commun. 2019, 10, 9. [PubMed: 30602780]

17. Yun GL; Tang SY; Lu HD; Cole T; Sun SS; Shu J; Zheng JH; Zhang QT; Zhang SW; Dickey MD; Li WH, Liquid Metal Hybrid Composites with High-Sensitivity and Large Dynamic Range Enabled by Micro- and Macrostructure Engineering. Acs Applied Polymer Materials 2021, 3 (10), 5302–5315.

18. Yi P; Zou HH; Yu YH; Li XF; Li ZY; Deng G; Chen CY; Fang M; He JZ; Sun X; Liu XF; Shui JL; Yu RH, MXene-Reinforced Liquid Metal/Polymer Fibers via Interface Engineering for Wearable Multifunctional Textiles. Acs Nano 2022, 13.

19. Kamysbayev V; James NM; Filatov AS; Srivastava V; Anasori B; Jaeger HM; Gogotsi Y; Talapin DV, Colloidal Gelation in Liquid Metals Enables Functional Nanocomposites of 2D Metal Carbides (MXenes) and Lightweight Metals. Acs Nano 2019, 13 (11), 12415–12424.

20. Lim T; Kim M; Akbarian A; Kim J; Tresco PA; Zhang HA, Conductive Polymer Enabled Biostable Liquid Metal Electrodes for Bioelectronic Applications. Adv. Healthc. Mater. 2022, 11 (11), 11.

21. Chen J; Zhang J; Luo Z; Zhang J; Li L; Su Y; Gao X; Li Y; Tang W; Cao C; Liu Q; Wang L; Li H, Superelastic, Sensitive, and Low Hysteresis Flexible Strain Sensor Based on Wave-Patterned

Liquid Metal for Human Activity Monitoring. ACS Appl Mater Interfaces 2020, 12 (19), 22200–22211.

22. Votzke C; Daalkhaijav U; Menguc Y; Johnston ML, 3D-Printed Liquid Metal Interconnects for Stretchable Electronics. IEEE Sens. J. 2019, 19 (10), 3832–3840.
23. Choe M; Sin D; Bhuyan P; Lee S; Jeon H; Park S, Ultrasoft and Ultrastretchable Wearable Strain Sensors with Anisotropic Conductivity Enabled by Liquid Metal Fillers. Micromachines 2023, 14 (1), 12.
24. Jiao YY; Young CW; Yang S; Oren S; Ceylan H; Kim S; Gopalakrishnan K; Taylor PC; Dong L, Wearable Graphene Sensors With Microfluidic Liquid Metal Wiring for Structural Health Monitoring and Human Body Motion Sensing. IEEE Sens. J. 2016, 16 (22), 7870–7875.
25. Handschuh-Wang S; Gan TS; Wang T; Stadler FJ; Zhou XC, Surface Tension of the Oxide Skin of Gallium-Based Liquid Metals. Langmuir 2021, 37 (30), 9017–9025. [PubMed: 34281345]
26. Martin A; Du CS; Chang B; Thuo M, Complexity and Opportunities in Liquid Metal Surface Oxides. Chem. Mat. 2020, 32 (21), 9045–9055.
27. Paik YH; Shin HC; Lee JM, Electrical charge of metal oxides in liquid metals. Met. Mater.-Korea 1998, 4 (5), 995–1000.
28. Zouvelou N; Mantzouris X; Nikolopoulos P, Interfacial energies in oxide/liquid metal systems with limited solubility. Int. J. Adhes. Adhes. 2007, 27 (5), 380–386.
29. Zhang W; Ou JZ; Tang SY; Sivan V; Yao DD; Latham K; Khoshmanesh K; Mitchell A; O'Mullane AP; Kalantar-zadeh K, Liquid Metal/Metal Oxide Frameworks. Advanced Functional Materials 2014, 24 (24), 3799–3807.
30. Li GY; Sun FK; Chen HS; Jin Y; Zhang AB; Du JK, High-Efficiency Large-Area Printed Multilayer Liquid Metal Wires for Stretchable Biomedical Sensors with Recyclability. ACS Appl. Mater. Interfaces 2021, 13 (48), 56961–56971. [PubMed: 34802230]
31. Feig VR; Remlova E; Muller B; Kuosmanen JLP; Lal N; Ginzburg A; Nan KW; Patel A; Jebran AM; Bantwal MP; Fabian N; Ishida K; Jenkins J; Rosenboom JG; Park S; Madani W; Hayward A; Traverso G, Actively Triggerable Metals via Liquid Metal Embrittlement for Biomedical Applications. Adv. Mater. 2023, 10.
32. Zhu LF; Wang B; Handschuh-Wang S; Zhou XC, Liquid Metal-Based Soft Microfluidics. Small 2020, 16 (9), 32.
33. Palleau E; Reece S; Desai SC; Smith ME; Dickey MD, Self-Healing Stretchable Wires for Reconfigurable Circuit Wiring and 3D Microfluidics. Adv. Mater. 2013, 25 (11), 1589–1592. [PubMed: 23334983]
34. Kong W; Wang ZY; Wang M; Manning KC; Uppal A; Green MD; Wang RY; Rykaczewski K, Oxide-Mediated Formation of Chemically Stable Tungsten-Liquid Metal Mixtures for Enhanced Thermal Interfaces. Adv. Mater. 2019, 31 (44), 8.
35. Xiao C; Feng J; Xu H; Xu R; Zhou T, Scalable Strategy to Directly Prepare 2D and 3D Liquid Metal Circuits Based on Laser-Induced Selective Metallization. ACS Appl Mater Interfaces 2022, 14 (17), 20000–20013.
36. Jo Y; Hwang JH; Lee SS; Lee SY; Kim YS; Kim DG; Choi Y; Jeong S, Printable Self-Activated Liquid Metal Stretchable Conductors from Polyvinylpyrrolidone-Functionalized Eutectic Gallium Indium Composites. ACS Appl. Mater. Interfaces 2022, 14 (8), 10747–10757.
37. Hajalilou A; Parvini E; Pereira JPM; Lopes PA; Silva AF; De Almeida A; Tavakoli M, Digitally Printable Magnetic Liquid Metal Composite for Recyclable Soft-Matter Electronics. Advanced Materials Technologies 2023, 13.
38. Veerapandian S; Jang W; Seol JB; Wang HB; Kong M; Thiyagarajan K; Kwak J; Park G; Lee G; Suh W; You I; Kilic ME; Giri A; Beccai L; Soon A; Jeong U, Hydrogen-doped viscoplastic liquid metal microparticles for stretchable printed metal lines. Nat. Mater. 2021, 20 (4), 533–540. [PubMed: 33398123]
39. Cho C; Shin W; Kim M; Bang J; Won P; Hong S; Ko SH, Monolithically Programmed Stretchable Conductor by Laser-Induced Entanglement of Liquid Metal and Metallic Nanowire Backbone. Small 2022, 18 (37), e2202841.
40. Dong JC; Tang XW; Peng YD; Fan CH; Li L; Zhang C; Lai FL; He GJ; Ma PM; Wang ZC; Wei QF; Yan XP; Qian HL; Huang YP; Liu TX, Highly permeable and ultrastretchable E-textiles

with EGaIn-superlyophilicity for on-skin health monitoring, joule heating, and electromagnetic shielding. Nano Energy 2023, 108, 13.

41. Yu YZ; Lu JR; Liu J, 3D printing for functional electronics by injection and package of liquid metals into channels of mechanical structures. Mater. Des. 2017, 122, 80–89.
42. Lazarus N; Bedair SS; Kierzewski IM, Ultrafine Pitch Stencil Printing of Liquid Metal Alloys. ACS Appl. Mater. Interfaces 2017, 9 (2), 1178–1182. [PubMed: 28058840]
43. Wang M; Ma C; Uzabakiriho PC; Chen X; Chen ZR; Cheng Y; Wang ZR; Zhao G, Stencil Printing of Liquid Metal upon Electrospun Nanofibers Enables High-Performance Flexible Electronics. Acs Nano 2021, 15 (12), 19364–19376. [PubMed: 34783541]
44. Hao XP; Li CY; Zhang CW; Du M; Ying ZM; Zheng Q; Wu ZL, Self-Shaping Soft Electronics Based on Patterned Hydrogel with Stencil-Printed Liquid Metal. Advanced Functional Materials 2021, 31 (47), 10.
45. Jeong YR; Kim J; Xie Z; Xue Y; Won SM; Lee G; Jin SW; Hong SY; Feng X; Huang Y; Rogers JA; Ha JS, A skin-attachable, stretchable integrated system based on liquid GaInSn for wireless human motion monitoring with multi-site sensing capabilities. NPG Asia Materials 2017, 9 (10), e443–e443.
46. Abbasi R; Mayyas M; Ghasemian MB; Centurion F; Yang J; Saborio M; Allioux FM; Han JL; Tang JB; Christoe MJ; Kabir KMM; Kalantar-Zadeh K; Rahim MA, Photolithography-enabled direct patterning of liquid metals. Journal of Materials Chemistry C 2020, 8 (23), 7805–7811.
47. Lin RZ; Kim HJ; Achavananthadith S; Xiong Z; Lee JKW; Kong YL; Ho JS, Digitally-embroidered liquid metal electronic textiles for wearable wireless systems. Nat. Commun. 2022, 13 (1), 10. [PubMed: 35121730]
48. Yang W; Li NW; Zhao SY; Yuan ZQ; Wang JN; Du XY; Wang B; Cao R; Li XY; Xu WH; Wang ZL; Li CJ, A Breathable and Screen-Printed Pressure Sensor Based on Nanofiber Membranes for Electronic Skins. Advanced Materials Technologies 2018, 3 (2), 7.
49. Ding SS; Lou YY; Niu ZH; Wang J; Jin X; Ma JY; Wang B; Li XY, A Highly Sensitive, Breathable, and Biocompatible Wearable Sensor Based on Nanofiber Membrane for Pressure and Humidity Monitoring. Macromol. Mater. Eng. 2022, 307 (9), 12.
50. Hyland M; Hunter H; Liu J; Veety E; Vashaee D, Wearable thermoelectric generators for human body heat harvesting. Appl. Energy 2016, 182, 518–524.
51. Huang QY; Zheng ZJ, Pathway to Developing Permeable Electronics. Acs Nano 2022, 16 (10), 15537–15544. [PubMed: 36200673]
52. Tan D; Xu BG; Gao YY; Tang Y; Liu YF; Yang YJ; Li ZH, Breathable fabric-based triboelectric nanogenerators with open-porous architected polydimethylsiloxane coating for wearable applications. Nano Energy 2022, 104, 8.
53. Peng Y; Liu H; Li T; Zhang J, Hybrid Metallic Foam with Superior Elasticity, High Electrical Conductivity, and Pressure Sensitivity. ACS Appl Mater Interfaces 2020, 12 (5), 6489–6495. [PubMed: 31927977]
54. Gao J; Ye J; Chen S; Gong J; Wang Q; Liu J, Liquid Metal Foaming via Decomposition Agents. ACS Appl Mater Interfaces 2021, 13 (14), 17093–17103. [PubMed: 33788538]
55. Jia LC; Jia XX; Sun WJ; Zhang YP; Xu L; Yan DX; Su HJ; Li ZM, Stretchable Liquid Metal-Based Conductive Textile for Electromagnetic Interference Shielding. ACS Appl Mater Interfaces 2020, 12 (47), 53230–53238.
56. Li Y; Wang S; Zhang J; Ma X; Cao S; Sun Y; Feng S; Fang T; Kong D, A Highly Stretchable and Permeable Liquid Metal Micromesh Conductor by Physical Deposition for Epidermal Electronics. ACS Appl Mater Interfaces 2022, 14 (11), 13713–13721.
57. Kim B; Jang J; You I; Park J; Shin S; Jeon G; Kim JK; Jeong U, Interfacing Liquid Metals with Stretchable Metal Conductors. ACS Appl. Mater. Interfaces 2015, 7 (15), 7920–7926. [PubMed: 25835190]
58. Yang YJ; Han J; Huang JR; Sun J; Wang ZL; Seo S; Sun QJ, Stretchable Energy-Harvesting Tactile Interactive Interface with Liquid-Metal-Nanoparticle-Based Electrodes. Advanced Functional Materials 2020, 30 (29), 10.
59. Park TH; Kim JH; Seo S, Facile and Rapid Method for Fabricating Liquid Metal Electrodes with Highly Precise Patterns via One-Step Coating. Advanced Functional Materials 2020, 30 (35), 9.

60. Zhang LJ; Gao M; Wang RH; Deng ZS; Gui L, Stretchable Pressure Sensor with Leakage-Free Liquid-Metal Electrodes. Sensors 2019, 19 (6), 16.
61. Lou Y; Liu HZ; Zhang JY, Liquid metals in plastics for super-toughness and high-performance force sensors. Chemical Engineering Journal 2020, 399, 8.
62. Hu T; Xuan SH; Ding L; Gong XL, Liquid metal circuit based magnetoresistive strain sensor with discriminating magnetic and mechanical sensitivity. Sens. Actuator B-Chem. 2020, 314, 11.
63. Guoqiang L; Sanhu L; Zhiwu X; Jinhong G; Shi-Yang T; Xing M, Recent advancements in liquid metal enabled flexible and wearable biosensors. Soft Science 2023, 3 (4), 37.
64. Costa G; Lopes PA; Sanati AL; Silva AF; Freitas MC; de Almeida AT; Tavakoli M, 3D Printed Stretchable Liquid Gallium Battery. Advanced Functional Materials 2022, 32 (27), 10.
65. Vallem V; Roosa E; Ledinh T; Jung W; Kim TI; Rashid-Nadimi S; Kiani A; Dickey MD, A Soft Variable-Area Electrical-Double-Layer Energy Harvester. Adv. Mater. 2021, 33 (43), 7.
66. Jackson N; Stam F, Sloshing liquid-metal mass for widening the bandwidth of a vibration energy harvester. Sens. Actuator A-Phys. 2018, 284, 17–21.
67. Wang KZ; Hu J; Chen TY; Tang JT; Wang ZY; Fan NN; Zhang WJ; Wang KJ, A High-Performance Room-Temperature Li||Ga-Sn Liquid Metal Battery for Grid Energy Storage. Energy Technol. 2021, 9 (9), 8.
68. Kim MG; Alrowais H; Kim C; Yeon P; Ghovanloo M; Brand O, All-soft, battery-free, and wireless chemical sensing platform based on liquid metal for liquid- and gas-phase VOC detection. Lab Chip 2017, 17 (13), 2323–2329. [PubMed: 28613302]
69. Moorefield MR; Ohta AT; Shiroma WA, Paper-based capillary actuation of liquid metal. Electron. Lett. 2017, 53 (20), 1372–1373.
70. Cho J; Richards C; Bahr D; Jiao J; Richards R, Evaluation of contacts for a MEMS thermal switch. J. Micromech. Microeng. 2008, 18 (10), 6.
71. Zhu JY; Tang SY; Khoshmanesh K; Ghorbani K, An Integrated Liquid Cooling System Based on Galinstan Liquid Metal Droplets. ACS Appl. Mater. Interfaces 2016, 8 (3), 2173–2180. [PubMed: 26716607]
72. Rahman MS; Huddy JE; Hamlin AB; Scheideler WJ, Broadband mechanoresponsive liquid metal sensors. npj Flexible Electronics 2022, 6 (1).
73. Karbalaei Akbari M; Zhuiykov S, A bioinspired optoelectronically engineered artificial neurorobotics device with sensorimotor functionalities. Nat Commun 2019, 10 (1), 3873. [PubMed: 31455784]
74. Daeneke T; Khoshmanesh K; Mahmood N; de Castro IA; Esrafilzadeh D; Barrow SJ; Dickey MD; Kalantar-zadeh K, Liquid metals: fundamentals and applications in chemistry. Chem. Soc. Rev. 2018, 47 (11), 4073–4111. [PubMed: 29611563]
75. Tang SY; Tabor C; Kalantar-Zadeh K; Dickey MD, Gallium Liquid Metal: The Devil's Elixir. In Annual Review of Materials Research, Vol 51, 2021, Clarke DR, Ed. Annual Reviews: Palo Alto, 2021; Vol. 51, pp 381–408.
76. Yu Q; Zhang Q; Zong J; Liu S; Wang X; Wang X; Zheng H; Cao Q; Zhang D; Jiang J, Identifying surface structural changes in a newly-developed Ga-based alloy with melting temperature below 10 °C. 2019, 492, 143–149.
77. Morris NJ; Farrell ZJ; Tabor CE, Chemically modifying the mechanical properties of core-shell liquid metal nanoparticles. Nanoscale 2019, 11 (37), 17308–17318.
78. Bilodeau RA; Zemlyanov DY; Kramer RK, Liquid Metal Switches for Environmentally Responsive Electronics. Adv. Mater. Interfaces 2017, 4 (5), 9.
79. Cabrera N; Mott NF, Theory of the oxidation of metals. Reports on Progress in Physics 1949, 12 (1), 163.
80. Xu Q; Oudalov N; Guo Q; Jaeger HM; Brown E, Effect of oxidation on the mechanical properties of liquid gallium and eutectic gallium-indium. Physics of Fluids 2012, 24 (6).
81. Handschuh-Wang S; Gan T; Wang T; Stadler FJ; Zhou X, Surface Tension of the Oxide Skin of Gallium-Based Liquid Metals. Langmuir 2021, 37 (30), 9017–9025. [PubMed: 34281345]

82. Xiong Y; Zhang X; Li H; Ding J; Cai S; Zhang W; Yang R, Liquid Gallium-Assisted Patterned Growth of β-Ga2O3 Nanowires on Metallic Foils for Photocatalytic Dye Degradation. ACS Applied Nano Materials 2023.

83. Ma J; Lin YL; Kim YW; Ko Y; Kim J; Oh KH; Sun JY; Gorman CB; Voinov MA; Smirnov AI; Genzer J; Dickey MD, Liquid Metal Nanoparticles as Initiators for Radical Polymerization of Vinyl Monomers. ACS Macro Lett. 2019, 8 (11), 1522–1527. [PubMed: 35651195]

84. Farrell ZJ; Tabor C, Control of Gallium Oxide Growth on Liquid Metal Eutectic Gallium/Indium Nanoparticles via Thiolation. Langmuir 2018, 34 (1), 234–240. [PubMed: 29215890]

85. McGuiness CL; Blasini D; Masejewski JP; Uppili S; Cabarcos OM; Smilgies D; Allara DL, Molecular self-assembly at bare semiconductor surfaces: Characterization of a homologous series of n-alkanethiolate monolayers on GaAs(001). Acs Nano 2007, 1 (1), 30–49. [PubMed: 19203128]

86. Hohman JN; Kim M; Wadsworth GA; Bednar HR; Jiang J; LeThai MA; Weiss PS, Directing Substrate Morphology via Self-Assembly: Ligand-Mediated Scission of Gallium-Indium Microspheres to the Nanoscale. Nano Lett. 2011, 11 (12), 5104–5110. [PubMed: 22023557]

87. Mou L; Qi J; Tang LX; Dong RH; Xia Y; Gao Y; Jiang XY, Highly Stretchable and Biocompatible Liquid Metal-Elastomer Conductors for Self-Healing Electronics. Small 2020, 16 (51), 9.

88. Vallem V; Aggarwal V; Dickey MD, Stretchable Liquid Metal Films with High Surface Area and Strain Invariant Resistance. Advanced Materials Technologies 2023, 8 (5), 9.

89. Tang SY; Qiao RR; Yan S; Yuan D; Zhao QB; Yun GL; Davis TP; Li WH, Microfluidic Mass Production of Stabilized and Stealthy Liquid Metal Nanoparticles. Small 2018, 14 (21), 8.

90. Bark H; Lee PS, Surface modification of liquid metal as an effective approach for deformable electronics and energy devices. Chem. Sci. 2021, 12 (8), 2760–2777. [PubMed: 34164040]

91. Huang ZY; Zou SY; Liu GZ, Surface Modification of Liquid Metal with p-Aniline Derivatives toward Bioapplications: Biosensing as an Example. ACS Appl. Mater. Interfaces 2022, 14 (51), 56429–56439.

92. Lu Y; Hu QY; Lin YL; Pacardo DB; Wang C; Sun WJ; Ligler FS; Dickey MD; Gu Z, Transformable liquid-metal nanomedicine. Nat. Commun. 2015, 6, 10.

93. Chechetka SA; Yu Y; Zhen X; Pramanik M; Pu KY; Miyako E, Light-driven liquid metal nanotransformers for biomedical theranostics. Nat. Commun. 2017, 8, 19. [PubMed: 28559566]

94. Guo C; He L; Yao YH; Lin WZ; Zhang YZ; Zhang Q; Wu K; Fu Q, Bifunctional Liquid Metals Allow Electrical Insulating Phase Change Materials to Dual-Mode Thermal Manage the Li-Ion Batteries. Nano-Micro Lett. 2022, 14 (1), 15.

95. Wu D; Liu DY; Tian XY; Lei CX; Chen XC; Zhang SM; Chen F; Wu K; Fu Q, A Universal Mechanochemistry Allows On-Demand Synthesis of Stable and Processable Liquid Metal Composites. Small Methods 2022, 6 (7), 8.

96. Wang CH; Gong Y; Cunning BV; Lee S; Le Q; Joshi SR; Buyukcakir O; Zhang HY; Seong WK; Huang M; Wang MH; Lee J; Kim GH; Ruoff RS, A general approach to composites containing nonmetallic fillers and liquid gallium. Science Advances 2021, 7 (1), 10.

97. Xu Y; Rothe R; Voigt D; Hauser S; Cui MY; Miyagawa T; Gaillez MP; Kurth T; Bornhauser M; Pietzsch J; Zhang YX, Convergent synthesis of diversified reversible network leads to liquid metal-containing conductive hydrogel adhesives. Nat. Commun. 2021, 12 (1), 19. [PubMed: 33397992]

98. Li Y; Miao Y; Yang LN; Zhao YT; Wu KK; Lu ZH; Hu ZQ; Guo JS, Recent Advances in the Development and Antimicrobial Applications of Metal-Phenolic Networks. Adv. Sci. 2022, 9 (27), 22.

99. Lin YL; Liu Y; Genzer J; Dickey MD, Shape-transformable liquid metal nanoparticles in aqueous solution. Chem. Sci. 2017, 8 (5), 3832–3837. [PubMed: 28580116]

100. Sun XY; Sun MM; Liu MM; Yuan B; Gao WP; Rao W; Liu J, Shape tunable gallium nanorods mediated tumor enhanced ablation through near-infrared photothermal therapy. Nanoscale 2019, 11 (6), 2655–2667. [PubMed: 30601530]

101. Lu Y; Lin YL; Chen ZW; Hu QY; Liu Y; Yu SJ; Gao W; Dickey MD; Gu Z, Enhanced Endosomal Escape by Light-Fueled Liquid-Metal Transformer. Nano Lett. 2017, 17 (4), 2138–2145. [PubMed: 28325042]

102. Gan TS; Shang WH; Handschuh-Wang S; Zhou XC, Light-Induced Shape Morphing of Liquid Metal Nanodroplets Enabled by Polydopamine Coating. Small 2019, 15 (9), 6.
103. Yan JJ; Zhang XD; Liu Y; Ye YQ; Yu JC; Chen Q; Wang JQ; Zhang YQ; Hu QY; Kang Y; Yang M; Gu Z, Shape-controlled synthesis of liquid metal nanodroplets for photothermal therapy. Nano Research 2019, 12 (6), 1313–1320.
104. Zhang YY; Guo ZZ; Zhu HR; Xing WK; Tao P; Shang W; Fu BW; Song CY; Hong Y; Dickey MD; Deng T, Synthesis of Liquid Gallium@Reduced Graphene Oxide Core-Shell Nanoparticles with Enhanced Photoacoustic and Photothermal Performance. J. Am. Chem. Soc. 2022, 144 (15), 6779–6790. [PubMed: 35293736]
105. Thrasher C; Farrell Z; Morris N; Willey C; Tabor C, Mechanoresponsive Polymerized Liquid Metal Networks. Adv. Mater. 2019, 31 (40), 8.
106. Ilyas N; Cook A; Tabor CE, Designing Liquid Metal Interfaces to Enable Next Generation Flexible and Reconfigurable Electronics. Adv. Mater. Interfaces 2017, 4 (15), 6.
107. Ma JW; Krisnadi F; Vong MH; Kong MS; Awartani OM; Dickey MD, Shaping a Soft Future: Patterning Liquid Metals. Adv. Mater. 2023, 35 (19), 31.
108. Lin Y; Gordon O; Khan MR; Vasquez N; Genzer J; Dickey MD, Vacuum filling of complex microchannels with liquid metal. Lab on a Chip 2017, 17 (18), 3043–3050. [PubMed: 28805880]
109. Khoshmanesh K; Tang SY; Zhu JY; Schaefer S; Mitchell A; Kalantar-Zadeh K; Dickey MD, Liquid metal enabled microfluidics. Lab on a Chip 2017, 17 (6), 974–993. [PubMed: 28225135]
110. Liang SQ; Li YY; Chen YZ; Yang JB; Zhu TP; Zhu DY; He CX; Liu YZ; Handschuh-Wang S; Zhou XC, Liquid metal sponges for mechanically durable, all-soft, electrical conductors. Journal of Materials Chemistry C 2017, 5 (7), 1586–1590.
111. Yao B; Hong W; Chen TW; Han ZB; Xu XW; Hu RC; Hao JY; Li CH; Li H; Perini SE; Lanagan MT; Zhang SL; Wang Q; Wang H, Highly Stretchable Polymer Composite with Strain-Enhanced Electromagnetic Interference Shielding Effectiveness. Adv. Mater. 2020, 32 (14), 7.
112. Yamagishi K; Zhou W; Ching T; Huang SY; Hashimoto M, Ultra-Deformable and Tissue-Adhesive Liquid Metal Antennas with High Wireless Powering Efficiency. Adv Mater 2021, 33 (26), e2008062.
113. Yang JB; Zhou TJ; Zhang LY; Zhu DY; Handschuh-Wang S; Liu Z; Kong TT; Liu YZ; Zhang JM; Zhou XC, Defect-free, high resolution patterning of liquid metals using reversibly sealed, reusable polydimethylsiloxane microchannels for flexible electronic applications. Journal of Materials Chemistry C 2017, 5 (27), 6790–6797.
114. Haake A; Tutika R; Schloer GM; Bartlett MD; Markvicka EJ, On-Demand Programming of Liquid Metal-Composite Microstructures through Direct Ink Write 3D Printing. Adv Mater 2022, 34 (20), e2200182.
115. Rahim MA; Centurion F; Han J; Abbasi R; Mayyas M; Sun J; Christoe MJ; Esrafilzadeh D; Allioux FM; Ghasemian MB; Yang J; Tang J; Daeneke T; Mettu S; Zhang J; Uddin MH; Jalili R; Kalantar-Zadeh K, Polyphenol-Induced Adhesive Liquid Metal Inks for Substrate-Independent Direct Pen Writing. Advanced Functional Materials 2020, 31 (10).
116. Xu J; Guo H; Ding H; Wang Q; Tang Z; Li Z; Sun G, Printable and Recyclable Conductive Ink Based on a Liquid Metal with Excellent Surface Wettability for Flexible Electronics. ACS Appl Mater Interfaces 2021, 13 (6), 7443–7452. [PubMed: 33528998]
117. Ladd C; So JH; Muth J; Dickey MD, 3D printing of free standing liquid metal microstructures. Adv Mater 2013, 25 (36), 5081–5085. [PubMed: 23824583]
118. Neumann TV; Dickey MD, Liquid Metal Direct Write and 3D Printing: A Review. 2020, 5 (9), 2000070.
119. Park YG; An HS; Kim JY; Park JU, High-resolution, reconfigurable printing of liquid metals with three-dimensional structures. Science Advances 2019, 5 (6), 9.
120. Wu Q; Zhu F; Wu Z; Xie Y; Qian J; Yin J; Yang H, Suspension printing of liquid metal in yield-stress fluid for resilient 3D constructs with electromagnetic functions. npj Flexible Electronics 2022, 6 (1), 50.
121. Daalkhaijav U; Yirmibesoglu OD; Walker S; Menguc Y, Rheological Modification of Liquid Metal for Additive Manufacturing of Stretchable Electronics. Advanced Materials Technologies 2018, 3 (4), 9.

122. Votzke C; Alteir N; Vasquez V; Menguc Y; Johnston ML; Ieee In Auger-Based 3D Printing of Stretchable Liquid Metal Paste Interconnects: A Brief Tutorial, International Conference on Flexible and Printable Sensors and Systems (FLEPS), Electr Network, Jun 20–23; Ieee: Electr Network, 2021.

123. Guo R; Tang J; Dong S; Lin J; Wang H; Liu J; Rao W, One-Step Liquid Metal Transfer Printing: Toward Fabrication of Flexible Electronics on Wide Range of Substrates. Advanced Materials Technologies 2018, 3 (12).

124. Guo R; Cui B; Zhao X; Duan M; Sun X; Zhao R; Sheng L; Liu J; Lu J, Cu–EGaIn enabled stretchable e-skin for interactive electronics and CT assistant localization. Materials Horizons 2020, 7 (7), 1845–1853.

125. Johnston L; Yang J; Han J; Kalantar-Zadeh K; Tang J, Intermetallic wetting enabled high resolution liquid metal patterning for 3D and flexible electronics. Journal of Materials Chemistry C 2022, 10 (3), 921–931.

126. Dong JC; Peng YD; Nie XL; Li L; Zhang C; Lai FL; He GJ; Ma PM; Wei QF; Huang YP; Liu TX, Hierarchically Designed Super-Elastic Metafabric for Thermal-Wet Comfortable and Antibacterial Epidermal Electrode. Advanced Functional Materials 2022, 32 (48), 12.

127. Wu D; Yao BW; Wu SW; Hingorani H; Cui QY; Hua MT; Frenkel I; Du YJ; Hsiai TK; He XM, Room-Temperature Annealing-Free Gold Printing via Anion-Assisted Photochemical Deposition. Adv. Mater. 2022, 34 (32), 10.

128. Tsujioka T; Nishimura A, Selective noble-metal deposition modulation on photocurable polydimethylsiloxane films for electronics device applications. Appl. Phys. A-Mater. Sci. Process. 2021, 127 (4), 8.

129. Zeledon JAZ; Stevens MB; Gunasooriya G; Gallo A; Landers AT; Kreider ME; Hahn C; Norskov JK; Jaramillo TF, Tuning the electronic structure of Ag-Pd alloys to enhance performance for alkaline oxygen reduction. Nat. Commun. 2021, 12 (1), 9. [PubMed: 33397931]

130. Guo R; Zhen Y; Huang X; Liu J, Spatially selective adhesion enabled transfer printing of liquid metal for 3D electronic circuits. Applied Materials Today 2021, 25.

131. Li Q; Lin J; Liu T; Dong S; Zheng H; Liu J, Supermetallophobic Functional Coatings Based on Silicate Clays and a Method To Pattern Liquid Metals. ACS Applied Electronic Materials 2020, 2 (7), 2229–2241.

132. Zhu H; Wang S; Zhang M; Li T; Hu G; Kong D, Fully solution processed liquid metal features as highly conductive and ultrastretchable conductors. npj Flexible Electronics 2021, 5 (1).

133. Guo R; Li TY; Wu ZY; Wan CX; Niu J; Huo WX; Yu HX; Huang X, Thermal Transfer-Enabled Rapid Printing of Liquid Metal Circuits on Multiple Substrates. ACS Appl. Mater. Interfaces 2022, 14 (32), 37028–37038.

134. Kim MG; Brown DK; Brand O, Nanofabrication for all-soft and high-density electronic devices based on liquid metal. Nat Commun 2020, 11 (1), 1002. [PubMed: 32081910]

135. Park CW; Moon YG; Seong H; Jung SW; Oh JY; Na BS; Park NM; Lee SS; Im SG; Koo JB, Photolithography-Based Patterning of Liquid Metal Interconnects for Monolithically Integrated Stretchable Circuits. ACS Appl Mater Interfaces 2016, 8 (24), 15459–65.

136. Pan CF; Kumar K; Li JZ; Markvicka EJ; Herman PR; Majidi C, Visually Imperceptible Liquid-Metal Circuits for Transparent, Stretchable Electronics with Direct Laser Writing. Adv. Mater. 2018, 30 (12), 9.

137. Lin YL; Genzer J; Dickey MD, Attributes, Fabrication, and Applications of Gallium-Based Liquid Metal Particles. Adv. Sci. 2020, 7 (12), 18.

138. Shi G; Peng XW; Zeng JM; Zhong LX; Sun Y; Yang W; Zhong YL; Zhu YX; Zou R; Admassie S; Liu ZQ; Liu CF; Iwuoha EI; Lu J, A Liquid Metal Microdroplets Initialized Hemicellulose Composite for 3D Printing Anode Host in Zn-Ion Battery. Adv. Mater. 2023, 10.

139. Liu Y; Ji XY; Liang JJ, Rupture stress of liquid metal nanoparticles and their applications in stretchable conductors and dielectrics. Npj Flexible Electronics 2021, 5 (1), 7.

140. Qiao RR; Tang SY, Connecting liquid metals with sound A stretchable conductive circuit is formed using a liquid metal-polymer composite. Science 2022, 378 (6620), 594–595. [PubMed: 36356152]

141. Yang R; Zhang W; Tiwari N; Yan H; Li T; Cheng H, Multimodal Sensors with Decoupled Sensing Mechanisms. Adv Sci (Weinh) 2022, 9 (26), e2202470.

142. Hu HJ; Huang H; Li MH; Gao XX; Yin L; Qi RX; Wu RS; Chen XJ; Ma YX; Shi KR; Li CH; Maus TM; Huang B; Lu C; Lin MY; Zhou S; Lou ZY; Gu Y; Chen YM; Lei YS; Wang XY; Wang RT; Yue WT; Yang XY; Bian YZ; Mu J; Park G; Xiang S; Cai SQ; Corey PW; Wang JS; Xu S, A wearable cardiac ultrasound imager. Nature 2023, 613 (7945), 23.

143. Moon S; Kim H; Lee K; Park J; Kim Y; Choi SQ, 3D Printable concentrated liquid metal composite with high thermal conductivity. Iscience 2021, 24 (10), 16.

144. Won P; Valentine CS; Zadan M; Pan C; Vinciguerra M; Patel DK; Ko SH; Walker LM; Majidi C, 3D Printing of Liquid Metal Embedded Elastomers for Soft Thermal and Electrical Materials. ACS Appl Mater Interfaces 2022, 14 (49), 55028–55038.

145. Park JE; Kang HS; Baek J; Park TH; Oh S; Lee H; Koo M; Park C, Rewritable, Printable Conducting Liquid Metal Hydrogel. ACS Nano 2019, 13 (8), 9122–9130. [PubMed: 31407567]

146. Li X; Li M; Xu J; You J; Yang Z; Li C, Evaporation-induced sintering of liquid metal droplets with biological nanofibrils for flexible conductivity and responsive actuation. Nature Communications 2019, 10 (1), 3514.

147. Lee W; Kim H; Kang I; Park H; Jung J; Lee H; Park H; Park JS; Yuk JM; Ryu S; Jeong JW; Kang J, Universal assembly of liquid metal particles in polymers enables elastic printed circuit board. Science 2022, 378 (6620), 637–641. [PubMed: 36356149]

148. Kim M; Cho CL; Shin W; Park JJ; Kim J; Won P; Majidi C; Ko SH, Nanowire-assisted freestanding liquid metal thin-film patterns for highly stretchable electrodes on 3D surfaces. Npj Flexible Electronics 2022, 6 (1), 8.

149. Liu S; Shah DS; Kramer-Bottiglio R, Highly stretchable multilayer electronic circuits using biphasic gallium-indium. Nat Mater 2021, 20 (6), 851–858. [PubMed: 33603186]

150. Lin YL; Cooper C; Wang M; Adams JJ; Genzer J; Dickey MD, Handwritten, Soft Circuit Boards and Antennas Using Liquid Metal Nanoparticles. Small 2015, 11 (48), 6397–6403. [PubMed: 26568095]

151. Boley JW; White EL; Kramer RK, Mechanically Sintered Gallium-Indium Nanoparticles. Adv. Mater. 2015, 27 (14), 2355–2360. [PubMed: 25728533]

152. Tang LX; Cheng SY; Zhang LY; Mi HB; Mou L; Yang SJ; Huang ZW; Shi XH; Jiang XY, Printable Metal-Polymer Conductors for Highly Stretchable Bio-Devices. Iscience 2018, 4, 302–311. [PubMed: 30240749]

153. Chen SW; Fan SC; Qi JM; Xiong Z; Qiao Z; Wu ZX; Yeo JC; Lim CT, Ultrahigh Strain-Insensitive Integrated Hybrid Electronics Using Highly Stretchable Bilayer Liquid Metal Based Conductor. Adv. Mater. 2023, 35 (5), 14.

154. Niu Y; Tian GW; Liang CY; Wang TC; Ma X; Gong GF; Qi DP, Thermal-Sinterable EGaIn Nanoparticle Inks for Highly Deformable Bioelectrode Arrays. Adv. Healthc. Mater. 2023, 12 (10), 11.

155. Liu SLZ; Yuen MC; White EL; Boley JW; Deng BW; Cheng GJ; Kramer-Bottiglio R, Laser Sintering of Liquid Metal Nanoparticles for Scalable Manufacturing of Soft and Flexible Electronics. ACS Appl. Mater. Interfaces 2018, 10 (33), 28232–28241. [PubMed: 30045618]

156. Liu SLZ; Reed SN; Higgins MJ; Titus MS; Kramer-Bottiglio R, Oxide rupture-induced conductivity in liquid metal nanoparticles by laser and thermal sintering. Nanoscale 2019, 11 (38), 17615–17629.

157. Lee GH; Lee YR; Kim H; Kwon D; Kim H; Yang C; Choi SQ; Park S; Jeong JW; Park S, Rapid meniscus-guided printing of stable semi-solid-state liquid metal microgranular-particle for soft electronics. Nat. Commun. 2022, 13 (1), 10. [PubMed: 35121730]

158. Lee GH; Woo H; Yoon C; Yang CQ; Bae JY; Kim W; Lee DH; Kang HM; Han S; Kang SK; Park S; Kim HR; Jeong JW; Park S, A Personalized Electronic Tattoo for Healthcare Realized by On-the-Spot Assembly of an Intrinsically Conductive and Durable Liquid-Metal Composite. Adv. Mater. 2022, 34 (32), 10.

159. Peng S; Yu Y; Wu S; Wang C-H, Conductive Polymer Nanocomposites for Stretchable Electronics: Material Selection, Design, and Applications. ACS Appl. Mater. Interfaces 2021, 13 (37), 43831–43854.

160. Zhu XY; Duan MH; Zhang L; Zhao JS; Yang S; Shen R; Chen S; Fan LL; Liu J, Liquid Metal-Enabled Microspheres with High Drug Loading and Multimodal Imaging for Artery Embolization. Advanced Functional Materials 2023, 33 (18), 11.

161. Yi LT; Li JJ; Guo CR; Li L; Liu J, Liquid Metal Ink Enabled Rapid Prototyping of Electrochemical Sensor for Wireless Glucose Detection on the Platform of Mobile Phone. J. Med. Devices 2015, 9 (4), 7.

162. Zhang Y; Duan HW; Li GQ; Peng MY; Ma X; Li M; Yan S, Construction of liquid metal-based soft microfluidic sensors via soft lithography. J. Nanobiotechnol. 2022, 20 (1), 15.

163. Wang Y; Li LT; Liang ST; Sun K; Jiao CC; Wang Q; Hu L, Liquid Metal pH Morphology Sensor Used for Biological Microenvironment Detection. Anal. Chem. 2022, 8.

164. Baharfar M; Mayyas M; Rahbar M; Allioux FM; Tang JB; Wang YF; Cao ZB; Centurion F; Jalili R; Liu GZ; Kalantar-Zadeh K, Exploring Interfacial Graphene Oxide Reduction by Liquid Metals: Application in Selective Biosensing. Acs Nano 2021, 15 (12), 19661–19671.

165. Mou L; Xia Y; Jiang XY, Liquid metal-polymer conductor-based wireless, battery-free epidermal patch. Biosens. Bioelectron. 2022, 197, 8.

166. Chen XQ; Wan H; Guo R; Wang XP; Wang Y; Jiao CC; Sun K; Hu L, A double-layered liquid metal-based electrochemical sensing system on fabric as a wearable detector for glucose in sweat. Microsyst. Nanoeng. 2022, 8 (1), 12. [PubMed: 35136651]

167. Wang Q; Yu Y; Pan KQ; Liu J, Liquid Metal Angiography for Mega Contrast X-Ray Visualization of Vascular Network in Reconstructing In-Vitro Organ Anatomy. IEEE Trans. Biomed. Eng. 2014, 61 (7), 2161–2166. [PubMed: 24759980]

168. Hartstein A; Kirtley JR; Tsang JC, Enhancement of the Infrared Absorption from Molecular Monolayers with Thin Metal Overlayers. Physical Review Letters 1980, 45 (3), 201–204.

169. Wu PC; Khoury CG; Kim T-H; Yang Y; Losurdo M; Bianco GV; Vo-Dinh T; Brown AS; Everitt HO, Demonstration of Surface-Enhanced Raman Scattering by Tunable, Plasmonic Gallium Nanoparticles. J. Am. Chem. Soc. 2009, 131 (34), 12032–12033.

170. Bian KF; Schunk H; Ye DM; Hwang A; Luk TS; Li RP; Wang ZW; Fan HY, Formation of self-assembled gold nanoparticle supercrystals with facet-dependent surface plasmonic coupling. Nat. Commun. 2018, 9, 7. [PubMed: 29295972]

171. Miao XL; Luk TS; Liu PQ, Liquid-Metal-Based Nanophotonic Structures for High-Performance SEIRA Sensing. Adv. Mater. 2022, 34 (10), 9.

172. Rahman MS; Huddy JE; Hamlin AB; Scheideler WJ, Broadband mechanoresponsive liquid metal sensors. Npj Flexible Electronics 2022, 6 (1), 8.

173. Cheng S; Rydberg A; Hjort K; Wu ZG, Liquid metal stretchable unbalanced loop antenna. Appl. Phys. Lett. 2009, 94 (14), 3.

174. So J-H; Thelen J; Qusba A; Hayes GJ; Lazzi G; Dickey MD, Reversibly Deformable and Mechanically Tunable Fluidic Antennas. 2009, 19 (22), 3632–3637.

175. Kubo M; Li XF; Kim C; Hashimoto M; Wiley BJ; Ham D; Whitesides GM, Stretchable Microfluidic Radiofrequency Antennas. Adv. Mater. 2010, 22 (25), 2749–2752. [PubMed: 20414886]

176. Huang YA; Wang YZ; Xiao L; Liu HM; Dong WT; Yin ZP, Microfluidic serpentine antennas with designed mechanical tunability. Lab on a Chip 2014, 14 (21), 4205–4212. [PubMed: 25144304]

177. Low JH; Chee PS; Lim EH, Liquid EBG-Backed Stretchable Slot Antenna for Human Body. Ieee Transactions on Antennas and Propagation 2022, 70 (10), 9120–9129.

178. Song L; Myers AC; Adams JJ; Zhu Y, Stretchable and Reversibly Deformable Radio Frequency Antennas Based on Silver Nanowires. ACS Applied Materials & Interfaces 2014, 6 (6), 4248–4253. [PubMed: 24593878]

179. Xiang X; Yang JS; Fan AW; Liu W, A comparison between cooling performances of water-based and gallium- based micro-channel heat sinks with the same dimensions. Appl. Therm. Eng. 2018, 137, 1–10.

180. Wang L; Lu JR; Wang MX; Zhang B; Hou YP; Liu GC; Yang W; Liu J, Anti-fogging performances of liquid metal surface modified by ZnO nano-petals. J. Taiwan Inst. Chem. Eng. 2019, 95, 65–70.

181. Liang QX; Yang Z; Guo JY; Li ZH; Chen TN; Li DC, A high-efficient tunable liquid metal-based electromagnetic absorbing metamaterial. J. Mater. Sci.-Mater. Electron. 2020, 31 (21), 19242–19247.
182. Xu YD; Lin ZQ; Rajavel K; Zhao T; Zhu PL; Hu YG; Sun R; Wong CP, Tailorable, Lightweight and Superelastic Liquid Metal Monoliths for Multifunctional Electromagnetic Interference Shielding. Nano-Micro Lett. 2022, 14 (1), 15.
183. Zhu RQ; Li ZY; Deng G; Yu YH; Shui JL; Yu RH; Pan CF; Liu XF, Anisotropic magnetic liquid metal film for wearable wireless electromagnetic sensing and smart electromagnetic interference shielding. Nano Energy 2022, 92, 10.
184. Yun T; Kim H; Iqbal A; Cho YS; Lee GS; Kim MK; Kim SJ; Kim D; Gogotsi Y; Kim SO; Koo CM, Electromagnetic Shielding of Monolayer MXene Assemblies. Adv. Mater. 2020, 32 (9), 9.
185. Sun Y; Han X; Guo P; Chai ZY; Yue JY; Su YT; Tan SD; Sun X; Jiang L; Heng LP, Slippery Graphene-Bridging Liquid Metal Layered Heterostructure Nanocomposite for Stable High-Performance Electromagnetic Interference Shielding. Acs Nano 2023, 13.
186. Wei QW; Pei SF; Qian XT; Liu HP; Liu ZB; Zhang WM; Zhou TY; Zhang ZC; Zhang XF; Cheng HM; Ren WC, Superhigh Electromagnetic Interference Shielding of Ultrathin Aligned Pristine Graphene Nanosheets Film. Adv. Mater. 2020, 32 (14), 9.
187. Wang S; Zhao XY; Luo J; Zhuang LL; Zou DQ, Liquid metal (LM) and its composites in thermal management. Compos. Pt. A-Appl. Sci. Manuf. 2022, 163, 27.
188. Yao B; Xu XW; Li H; Han ZB; Hao JY; Yang G; Xie ZX; Chen YT; Liu WS; Wang Q; Wang H, Soft liquid-metal/elastomer foam with compression-adjustable thermal conductivity and electromagnetic interference shielding. Chemical Engineering Journal 2021, 410, 8.
189. Wu Y; Zhou Y; Asghar W; Liu Y; Li F; Sun D; Hu C; Wu Z; Shang J; Yu Z; Li R-W; Yang H, Liquid Metal - Based Strain Sensor with Ultralow Detection Limit for Human–Machine Interface Applications. Advanced Intelligent Systems 2021, 3 (10).
190. Sun F; Liu L; Liu T; Wang X; Qi Q; Hang Z; Chen K; Xu J; Fu J, Vascular smooth muscle-inspired architecture enables soft yet tough self-healing materials for durable capacitive strain-sensor. Nat Commun 2023, 14 (1), 130. [PubMed: 36624140]
191. Wu H; Qi H; Wang X; Qiu Y; Shi K; Zhang H; Zhang Z; Zhang W; Tian Y, Stretchable, sensitive, flexible strain sensor incorporated with patterned liquid metal on hydrogel for human motion monitoring and human–machine interaction. Journal of Materials Chemistry C 2022, 10 (21), 8206–8217.
192. Hao XP; Zhang CW; Zhang XN; Hou LX; Hu J; Dickey MD; Zheng Q; Wu ZL, Healable, Recyclable, and Multifunctional Soft Electronics Based on Biopolymer Hydrogel and Patterned Liquid Metal. Small 2022, 18 (23), e2201643.
193. Wu YZ; Zhou YL; Asghar W; Liu YW; Li FL; Sun DD; Hu C; Wu ZG; Shang J; Yu Z; Li RW; Yang HL, Liquid Metal-Based Strain Sensor with Ultralow Detection Limit for Human-Machine Interface Applications. Advanced Intelligent Systems 2021, 3 (10), 8.
194. Li GQ; Zhang MY; Liu SH; Yuan M; Wu JJ; Yu M; Teng LJ; Xu ZW; Guo JH; Li GL; Liu ZY; Ma X, Three-dimensional flexible electronics using solidified liquid metal with regulated plasticity. Nature Electronics 2023, 6 (2), 154–163.
195. Nan K; Babaee S; Chan WW; Kuosmanen JLP; Feig VR; Luo Y; Srinivasan SS; Patterson CM; Jebran AM; Traverso G, Low-cost gastrointestinal manometry via silicone-liquid-metal pressure transducers resembling a quipu. Nat Biomed Eng 2022, 6 (10), 1092–1104. [PubMed: 35314802]
196. Ma ZJ; Huang QY; Xu Q; Zhuang QN; Zhao X; Yang YH; Qiu H; Yang ZL; Wang C; Chai Y; Zheng ZJ, Permeable superelastic liquid-metal fibre mat enables biocompatible and monolithic stretchable electronics. Nat. Mater. 2021, 20 (6), 859–868. [PubMed: 33603185]
197. Cao JW; Liang F; Li HY; Li X; Fan YJ; Hu C; Yu J; Xu J; Yin YM; Li FL; Xu D; Feng HF; Yang HL; Liu YW; Chen XD; Zhu G; Li RW, Ultra-robust stretchable electrode for e-skin: In situ assembly using a nanofiber scaffold and liquid metal to mimic water-to-net interaction. Infomat 2022, 4 (4), 14.
198. Choi H; Luo YC; Olson G; Won P; Shin JH; Ok J; Yang YJ; Kim TI; Majidi C, Highly Stretchable and Strain-Insensitive Liquid Metal based Elastic Kirigami Electrodes (LM-eKE). Advanced Functional Materials 2023, 10.

199. Sun XL; Fu JH; Zhao HB; Xiang WT; Zhan F; Sun CK; Tang SS; Wang L; Liu J, Electronic whiskers for velocity sensing based on the liquid metal hysteresis effect. Soft Matter 2022, 18 (48), 9153–9162. [PubMed: 36458603]

200. Wang YL; Qin WJ; Yang M; Tian ZH; Guo WJ; Sun JK; Zhou X; Fei B; An BG; Sun RM; Yin SG; Liu ZF, High Linearity, Low Hysteresis Ti3C2Tx MXene/AgNW/Liquid Metal Self-Healing Strain Sensor Modulated by Dynamic Disulfide and Hydrogen Bonds. Advanced Functional Materials 2023, 11.

201. Lee S; Byun S-H; Kim CY; Cho S; Park S; Sim JY; Jeong J-W, Beyond Human Touch Perception: An Adaptive Robotic Skin Based on Gallium Microgranules for Pressure Sensory Augmentation. 2022, 34 (44), 2204805.

202. Malakooti MH; Kazem N; Yan J; Pan C; Markvicka EJ; Matyjaszewski K; Majidi C, Liquid Metal Supercooling for Low-Temperature Thermoelectric Wearables. 2019, 29 (45), 1906098.

203. Varga M; Ladd C; Ma SY; Holbery J; Tröster G, On-skin liquid metal inertial sensor. Lab on a Chip 2017, 17 (19), 3272–3278. [PubMed: 28836638]

204. Xu KC; Fujita Y; Lu YY; Honda S; Shiomi M; Arie T; Akita S; Takei K, A Wearable Body Condition Sensor System with Wireless Feedback Alarm Functions. Adv. Mater. 2021, 33 (18), 13.

205. Babatain W; Buttner U; El-Atab N; Hussain MM, Graphene and Liquid Metal Integrated Multifunctional Wearable Platform for Monitoring Motion and Human-Machine Interfacing. Acs Nano 2022, 16 (12), 20305–20317.

206. Xu YD; Sun BH; Ling Y; Fei QH; Chen ZY; Li XP; Guo PJ; Jeon N; Goswami S; Liao YX; Ding SH; Yu QS; Lin J; Huang GL; Yan Z, Multiscale porous elastomer substrates for multifunctional on-skin electronics with passive-cooling capabilities. Proc. Natl. Acad. Sci. U. S. A. 2020, 117 (1), 205–213. [PubMed: 31871158]

207. Wan YB; Qiu ZG; Huang J; Yang JY; Wang Q; Lu P; Yang JL; Zhang JM; Huang SY; Wu ZG; Guo CF, Natural Plant Materials as Dielectric Layer for Highly Sensitive Flexible Electronic Skin. Small 2018, 14 (35), 8.

208. Guo Y; Zhong MJ; Fang ZW; Wan PB; Yu GH, A Wearable Transient Pressure Sensor Made with MXene Nanosheets for Sensitive Broad-Range Human-Machine Interfacing. Nano Lett. 2019, 19 (2), 1143–1150. [PubMed: 30657695]

209. Yang CF; Li LL; Zhao JX; Wang JJ; Xie JX; Cao YP; Xue MQ; Lu CH, Highly Sensitive Wearable Pressure Sensors Based on Three-Scale Nested Wrinkling Microstructures of Polypyrrole Films. ACS Appl. Mater. Interfaces 2018, 10 (30), 25811–25818. [PubMed: 29993231]

210. Mao LN; Pan TS; Guo JX; Ke YZ; Zhu J; Cheng HY; Lin Y, Reconfigurable, Stretchable Strain Sensor with the Localized Controlling of Substrate Modulus by Two-Phase Liquid Metal Cells. Nanomaterials 2022, 12 (5), 11.

211. Xu J; Tat T; Zhao X; Zhou YH; Ngo D; Xiao X; Chen J, A programmable magnetoelastic sensor array for self-powered human-machine interface. Appl. Phys. Rev. 2022, 9 (3), 8.

212. Votzke C; Daalkhaijav U; Menguc Y; Johnston ML; Ieee In Highly-Stretchable Biomechanical Strain Sensor using Printed Liquid Metal Paste, IEEE Biomedical Circuits and Systems Conference (BioCAS) - Advanced Systems for Enhancing Human Health, Cleveland, OH, Oct 17–19; Ieee: Cleveland, OH, 2018; pp 37–40.

213. Gul O; Kim K; Gu J; Choi J; Henriquez DD; Ahn J; Park I, Sensitivity-Controllable Liquid-Metal-Based Pressure Sensor for Wearable Applications. Acs Applied Electronic Materials 2021, 3 (9), 4027–4036.

214. Zheng K; Gu F; Wei HJ; Zhang LJ; Chen X; Jin HL; Pan S; Chen YH; Wang S, Flexible, Permeable, and Recyclable Liquid-Metal-Based Transient Circuit Enables Contact/Noncontact Sensing for Wearable Human-Machine Interaction. Small Methods 2023, 7 (4), 10.

215. Yun GL; Cole T; Zhang YX; Zheng JH; Sun SS; Ou-yang Y; Shu J; Lu HD; Zhang QT; Wang YJ; Pham D; Hasan T; Li WH; Zhang SW; Tang SY, Electro-mechano responsive elastomers with self- tunable conductivity and stiffness. Science Advances 2023, 9 (4), 10.

216. Mitra A; Xu K; Babu S; Choi JH; Lee JB, Liquid-Metal-Enabled Flexible Metasurface with Self-Healing Characteristics. Adv. Mater. Interfaces 2022, 9 (12), 7.

217. Wu PC; Zhu WM; Shen ZX; Chong PHJ; Ser W; Tsai DP; Liu AQ, Broadband Wide-Angle Multifunctional Polarization Converter via Liquid-Metal-Based Metasurface. Adv. Opt. Mater. 2017, 5 (7), 7.
218. Yang X; Liu Y; Lei HY; Jia YT; Zhu PS; Zhou ZP, A Radiation Pattern Reconfigurable Fabry-Perot Antenna Based on Liquid Metal. Ieee Transactions on Antennas and Propagation 2020, 68 (11), 7658–7663.
219. Reichel KS; Lozada-Smith N; Joshipura ID; Ma JJ; Shrestha R; Mendis R; Dickey MD; Mittleman DM, Electrically reconfigurable terahertz signal processing devices using liquid metal components. Nat. Commun. 2018, 9, 6. [PubMed: 29295974]
220. Watson AM; Leary TF; Elassy KS; Mattamana AG; Rahman MA; Shiroma WA; Ohta AT; Tabor CE, Physically Reconfigurable RF Liquid Electronics via Laplace Barriers. IEEE Trans. Microw. Theory Tech. 2019, 67 (12), 4881–4889.
221. Zhang GB; Gough RC; Moorefield MR; Cho KJ; Ohta AT; Shiroma WA, A Liquid-Metal Polarization-Pattern-Reconfigurable Dipole Antenna. IEEE Antennas Wirel. Propag. Lett. 2018, 17 (1), 50–53.
222. Yang L; Wang ZH; Wang H; Jin BQ; Meng CZ; Chen X; Li RZ; Wang H; Xin MY; Zhao ZS; Guo SJ; Wu JR; Cheng HY, Self-Healing, Reconfigurable, Thermal-Switching, Transformative Electronics for Health Monitoring. Adv. Mater. 2023, 35 (15), 15.
223. Li XF; Jiang M; Du YM; Ding X; Xiao C; Wang YY; Yang YY; Zhuo YZ; Zheng K; Liu XL; Chen L; Gong Y; Tian XY; Zhang X, Self-healing liquid metal hydrogel for human-computer interaction and infrared camouflage. Materials Horizons 2023, 13.
224. Wang S; Urban MW, Self-healing polymers. Nature Reviews Materials 2020, 5 (8), 562–583.
225. Cole T; Tang S-Y, Liquid metals as soft electromechanical actuators. Materials Advances 2022, 3 (1), 173–185.
226. Shu J; Ge DA; Wang EL; Ren HT; Cole T; Tang SY; Li XP; Zhou XB; Li RJ; Jin H; Li WH; Dickey MD; Zhang SW, A Liquid Metal Artificial Muscle. Adv. Mater. 2021, 33 (43), 10.
227. Vasilkov OS; Dobysh VS; Ieee In Features of Application Hybrid Energy Storage in Power Supply Systems, IEEE Conference of Russian Young Researchers in Electrical and Electronic Engineering (EIConRus), St Petersburg Electrotechn Univ, RUSSIA, Jan 28–31; Ieee: St Petersburg Electrotechn Univ, RUSSIA, 2019; pp 728–730.
228. Guan MJ; Liao WH, Characteristics of energy storage devices in piezoelectric energy harvesting systems. J. Intell. Mater. Syst. Struct. 2008, 19 (6), 671–680.
229. Dhavale SM; Kulkarni NM; Shaligram AD In Development of Energy Storage Device for Mobile Health Monitoring, 3rd International Conference on Emerging Technologies - Micro to Nano (ETMN), Solapur Univ, Solapur, INDIA, Oct 06–07; Amer Inst Physics: Solapur Univ, Solapur, INDIA, 2017.
230. Vallem V; Sargolzaeiaval Y; Ozturk M; Lai YC; Dickey MD, Energy Harvesting and Storage with Soft and Stretchable Materials. Adv. Mater. 2021, 33 (19), 37.
231. Kim MG; Lee B; Li M; Noda S; Kim C; Kim J; Song WJ; Lee SW; Brand O, All-Soft Supercapacitors Based on Liquid Metal Electrodes with Integrated Functionalized Carbon Nanotubes. Acs Nano 2020, 14 (5), 5659–5667. [PubMed: 32379413]
232. Ramesh VP; Sargolzaeiaval Y; Neumann T; Misra V; Vashaee D; Dickey MD; Ozturk MC, Flexible thermoelectric generator with liquid metal interconnects and low thermal conductivity silicone filler. Npj Flexible Electronics 2021, 5 (1), 12.
233. Zhong LN; Tang LX; Yang SJ; Zhao ZT; Zheng ZJ; Jiang XY, Stretchable Liquid Metal-Based Metal-Polymer Conductors for Fully Screen-Printed Biofuel Cells. Anal. Chem. 2022, 94 (48), 16738–16745.
234. Shen QC; Jiang MD; Wang RT; Song KX; Vong MH; Jung WJ; Krisnadi F; Kan RY; Zheng FY; Fu BW; Tao P; Song CY; Weng GM; Peng B; Wang J; Shang W; Dickey MD; Deng T, Liquid metal-based soft, hermetic, and wireless-communicable seals for stretchable systems. Science 2023, 379 (6631), 488–493. [PubMed: 36730410]
235. Qi DP; Zhang KY; Tian GW; Jiang B; Huang YD, Stretchable Electronics Based on PDMS Substrates. Adv. Mater. 2021, 33 (6), 25.

236. Lim HR; Kim HS; Qazi R; Kwon YT; Jeong JW; Yeo WH, Advanced Soft Materials, Sensor Integrations, and Applications of Wearable Flexible Hybrid Electronics in Healthcare, Energy, and Environment. Adv. Mater. 2020, 32 (15), 43.

237. Tang LX; Shang J; Jiang XY, Multilayered electronic transfer tattoo that can enable the crease amplification effect. Science Advances 2021, 7 (3), 10.

238. Ochirkhuyag N; Matsuda R; Song ZH; Nakamura F; Endo T; Ota H, Liquid metal-based nanocomposite materials: fabrication technology and applications. Nanoscale 2021, 13 (4), 2113–2135. [PubMed: 33465221]

239. Cheng JH; Shang J; Yang SJ; Dou JB; Shi XH; Jiang XY, Wet-Adhesive Elastomer for Liquid Metal-Based Conformal Epidermal Electronics. Advanced Functional Materials 2022, 32 (25), 12.

240. Jeong SH; Zhang S; Hjort K; Hilborn J; Wu ZG, PDMS-Based Elastomer Tuned Soft, Stretchable, and Sticky for Epidermal Electronics. Adv. Mater. 2016, 28 (28), 5830–5836. [PubMed: 27167137]

241. Tang LX; Yang SJ; Zhang K; Jiang XY, Skin Electronics from Biocompatible In Situ Welding Enabled By Intrinsically Sticky Conductors. Adv. Sci. 2022, 9 (23), 11.

242. Yang L; Wang Z; Wang H; Jin B; Meng C; Chen X; Li R; Wang H; Xin M; Zhao Z; Guo S; Wu J; Cheng H, Self-Healing, Reconfigurable, Thermal-Switching, Transformative Electronics for Health Monitoring. Advanced Materials 2023, 35 (15), 2207742.

243. Pei DF; Yu SY; Liu P; Wu YP; Zhang XF; Chen YJ; Li MJ; Li CX, Reversible Wet-Adhesive and Self-Healing Conductive Composite Elastomer of Liquid Metal. Advanced Functional Materials 2022, 32 (35), 9.

244. Zhou ZX; Qian CH; Yuan WZ, Self-healing, anti-freezing, adhesive and remoldable hydrogel sensor with ion-liquid metal dual conductivity for biomimetic skin. Compos. Sci. Technol. 2021, 203, 10.

245. Sun M; Li P; Qin H; Liu N; Ma H; Zhang Z; Li J; Lu B; Pan X; Wu L, Liquid metal/CNTs hydrogel-based transparent strain sensor for wireless health monitoring of aquatic animals. Chemical Engineering Journal 2023, 454, 140459.

246. Ding L; Hang C; Yang SJ; Qi J; Dong RH; Zhang Y; Sun HS; Jiang XY, In Situ Deposition of Skin-Adhesive Liquid Metal Particles with Robust Wear Resistance for Epidermal Electronics. Nano Lett. 2022, 22 (11), 4482–4490. [PubMed: 35580197]

247. Xue JJ; Wu T; Dai YQ; Xia YN, Electrospinning and Electrospun Nanofibers: Methods, Materials, and Applications. Chem. Rev. 2019, 119 (8), 5298–5415. [PubMed: 30916938]

248. Zhuang QN; Ma ZJ; Gao Y; Zhang YK; Wang SC; Lu X; Hu H; Cheung CF; Huang QY; Zheng ZJ, Liquid-Metal-Superlyophilic and Conductivity-Strain-Enhancing Scaffold for Permeable Superelastic Conductors. Advanced Functional Materials 2021, 31 (47), 8.

249. Wang F; Altschuh P; Ratke L; Zhang HD; Selzer M; Nestler B, Progress Report on Phase Separation in Polymer Solutions. Adv. Mater. 2019, 31 (26), 14.

250. Xu YD; Su YJ; Xu XC; Arends B; Zhao GG; Ackerman DN; Huang HY; Reid SP; Santarpia JL; Kim C; Chen ZH; Mahmoud S; Ling Y; Brown A; Chen Q; Huang GL; Xie JW; Yan Z, Porous liquid metal-elastomer composites with high leakage resistance and antimicrobial property for skin-interfaced bioelectronics. Science Advances 2023, 9 (1), 10.

251. Liu SLZ; Kim SY; Henry KE; Shah DS; Kramer-Bottiglio R, Printed and Laser-Activated Liquid Metal-Elastomer Conductors Enabled by Ethanol/PDMS/Liquid Metal Double Emulsions. ACS Appl. Mater. Interfaces 2021, 13 (24), 28729–28736.

252. Gong S; Yap LW; Zhu Y; Zhu BW; Wang Y; Ling YZ; Zhao YM; An TC; Lu YR; Cheng WL, A Soft Resistive Acoustic Sensor Based on Suspended Standing Nanowire Membranes with Point Crack Design. Advanced Functional Materials 2020, 30 (25), 9.

253. Haake A; Tutika R; Schloer GM; Bartlett MD; Markvicka EJ, On-Demand Programming of Liquid Metal-Composite Microstructures through Direct Ink Write 3D Printing. Adv. Mater. 2022, 34 (20), 11.

254. Lu T; Wissman J; Ruthika; Majidi C, Soft Anisotropic Conductors as Electric Vias for Ga-Based Liquid Metal Circuits. ACS Appl. Mater. Interfaces 2015, 7 (48), 26923–26929.

255. Lopes PA; Santos BC; de Almeida AT; Tavakoli M, Reversible polymer-gel transition for ultrastretchable chip-integrated circuits through self-soldering and self-coating and self-healing. Nat. Commun. 2021, 12 (1), 10. [PubMed: 33397896]

256. Sen P; Kim CJ, Microscale Liquid-Metal Switches-A Review. IEEE Trans. Ind. Electron. 2009, 56 (4), 1314–1330.

257. Culjat MO; Singh RS; White SN; Neurgaonkar RR; Brown ER, Evaluation of gallium-indium alloy as an acoustic couplant for high-impedance, high-frequency applications. Acoust. Res. Lett. Online-ARLO 2005, 6 (3), 125–130.

258. Liu TY; Sen P; Kim C, Characterization of Nontoxic Liquid-Metal Alloy Galinstan for Applications in Microdevices. J. Microelectromech. Syst. 2012, 21 (2), 443–450.

259. Morley NB; Burris J; Cadwallader LC; Nornberg MD, GaInSn usage in the research laboratory. Rev. Sci. Instrum. 2008, 79 (5), 3.

260. Zrnić D; Swatik D. S. J. J. o. T. L. C. M., On the resistivity and surface tension of the eutectic alloy of gallium and indium. 1969, 18, 67–68.

261. Assael MJ; Armyra IJ; Brillo J; Stankus SV; Wu JT; Wakeham WA, Reference Data for the Density and Viscosity of Liquid Cadmium, Cobalt, Gallium, Indium, Mercury, Silicon, Thallium, and Zinc. J. Phys. Chem. Ref. Data 2012, 41 (3), 16.

262. Dickey MD; Chiechi RC; Larsen RJ; Weiss EA; Weitz DA; Whitesides GM, Eutectic gallium-indium (EGaIn): A liquid metal alloy for the formation of stable structures in microchannels at room temperature. Advanced Functional Materials 2008, 18 (7), 1097–1104.

263. Zheng RM; Peng ZF; Fu Y; Deng ZF; Liu SQ; Xing ST; Wu YY; Li JY; Liu L, A Novel Conductive Core-Shell Particle Based on Liquid Metal for Fabricating Real-Time Self-Repairing Flexible Circuits. Advanced Functional Materials 2020, 30 (15), 8.

264. Zhao RQ; Guo R; Xu XL; Liu J, A Fast and Cost-Effective Transfer Printing of Liquid Metal Inks for Three-Dimensional Wiring in Flexible Electronics. ACS Appl. Mater. Interfaces 2020, 12 (32), 36723–36730.

265. Ye D; Peng Z; Liu J; Huang Y, Self-Limited ultraviolet laser sintering of liquid metal particles for μm-Thick flexible electronics devices. Mater. Des. 2022, 223, 111189.

266. Wu J; Hu J; Feng Y; Fan H; Wang K; Deng Z, Mechanical sintering-induced conductive flexible self-healing eGaInSn@PDA NDs/TPU composite based on structural design to against liquid metal leakage. Chemical Engineering Journal 2023, 458.

267. Neumann TV; Facchine EG; Leonardo B; Khan S; Dickey MD, Direct write printing of a self-encapsulating liquid metal-silicone composite. Soft Matter 2020, 16 (28), 6608–6618. [PubMed: 32613217]

268. Zhang S; Wang B; Jiang J; Wu K; Guo CF; Wu Z, High-Fidelity Conformal Printing of 3D Liquid Alloy Circuits for Soft Electronics. ACS Appl Mater Interfaces 2019, 11 (7), 7148–7156. [PubMed: 30675789]

269. Wu H; Zhang LR; Jiang SJ; Zhang YY; Zhang YC; Xin C; Ji SY; Zhu WL; Li JW; Hu YL; Wu D; Chu JR, Ultrathin and High-Stress-Resolution Liquid-Metal-Based Pressure Sensors with Simple Device Structures. ACS Appl. Mater. Interfaces 2020, 12 (49), 55390–55398.

270. Chang H; Zhang P; Guo R; Cui Y; Hou Y; Sun Z; Rao W, Recoverable Liquid Metal Paste with Reversible Rheological Characteristic for Electronics Printing. ACS Appl Mater Interfaces 2020, 12 (12), 14125–14135.

271. Yang J; Cao J; Han J; Xiong Y; Luo L; Dan X; Yang Y; Li L; Sun J; Sun Q, Stretchable multifunctional self-powered systems with Cu-EGaIn liquid metal electrodes. Nano Energy 2022, 101.

272. Zhang YR; Cheng ZL; Ni CK; Wang ZX; Yu YS; Zhai XX; Xu SL; Zhao ZW; Hu L; Hu Y, Highly conductive EGaIn/silk fibroin ink for graphene 3D array structure micro-supercapacitors. Chemical Engineering Journal 2022, 428, 9.

273. Cao LX; Yu DH; Xia ZS; Wan HY; Liu CK; Yin T; He ZZ, Ferromagnetic Liquid Metal Putty-Like Material with Transformed Shape and Reconfigurable Polarity. Adv. Mater. 2020, 32 (17), 9.

274. Guo R; Sun X; Yuan B; Wang H; Liu J, Magnetic Liquid Metal (Fe-EGaIn) Based Multifunctional Electronics for Remote Self-Healing Materials, Degradable Electronics, and Thermal Transfer Printing. Adv Sci (Weinh) 2019, 6 (20), 1901478.

275. Ma B; Xu CT; Chi JJ; Chen J; Zhao C; Liu H, A Versatile Approach for Direct Patterning of Liquid Metal Using Magnetic Field. Advanced Functional Materials 2019, 29 (28), 8.

276. Kim S; Kim S; Hong K; Dickey MD; Park S, Liquid-Metal-Coated Magnetic Particles toward Writable, Nonwettable, Stretchable Circuit Boards, and Directly Assembled Liquid Metal-Elastomer Conductors. ACS Appl Mater Interfaces 2022, 14 (32), 37110–37119.

277. Park YG; Min H; Kim H; Zhexembekova A; Lee CY; Park JU, Three-Dimensional, High-Resolution Printing of Carbon Nanotube/Liquid Metal Composites with Mechanical and Electrical Reinforcement. Nano Lett. 2019, 19 (8), 4866–4872. [PubMed: 30983359]

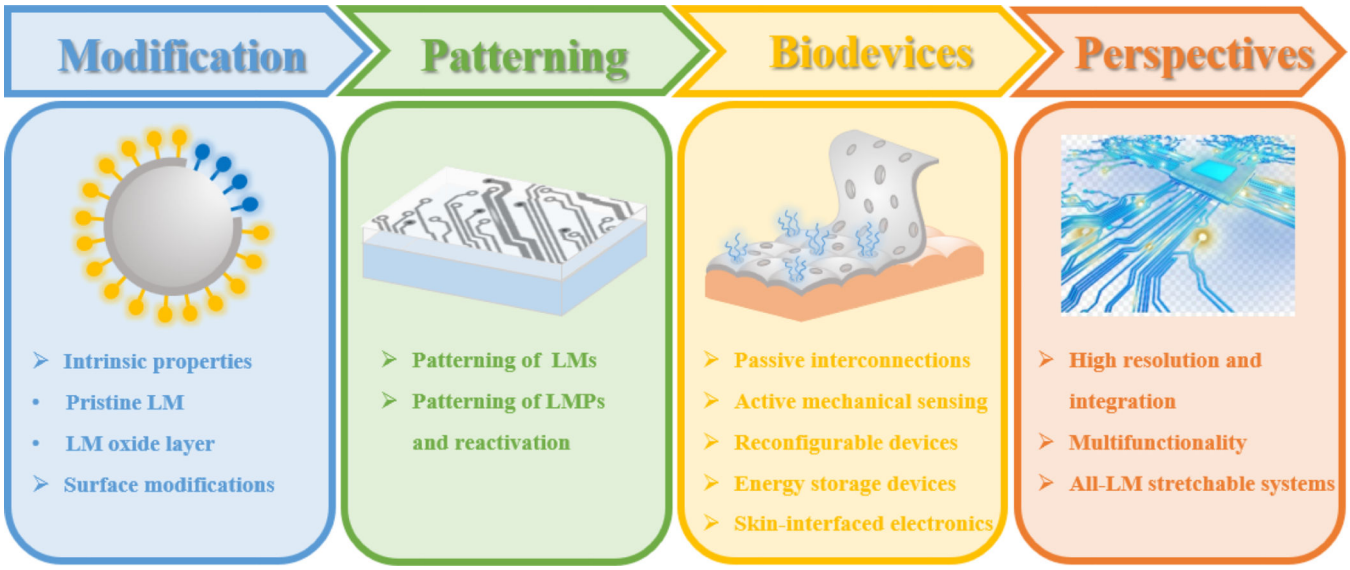

Fig. 1. Overview of the liquid metal (LM)-based bioelectronics.

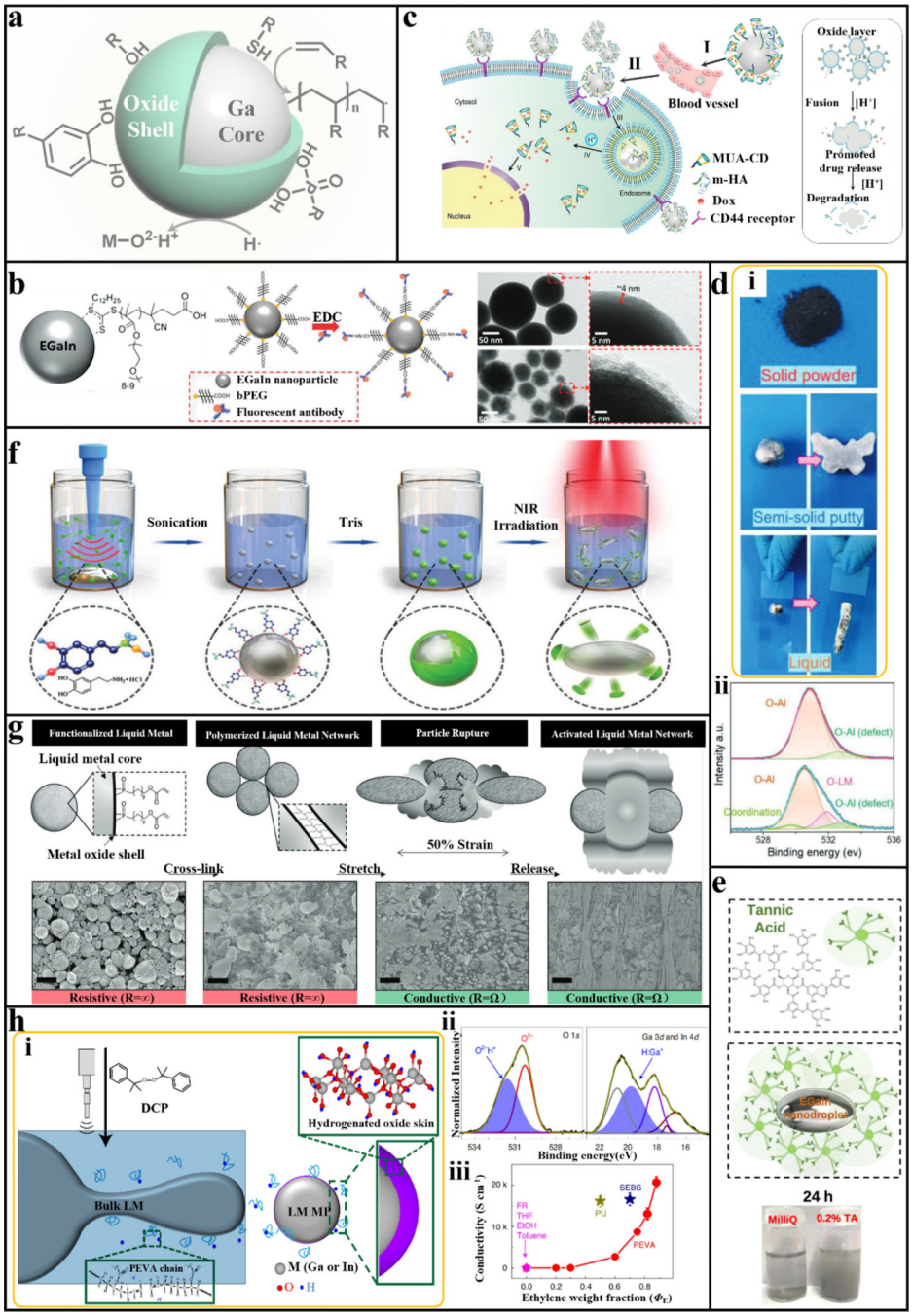

Fig. 2. Surface modification of Ga-based LMs

(a) Schematic showing the surface modification on Ga-based LMs. The modification site can be the inner LM core or the outside oxide layer. The inner pristine Ga atom is highly reactive to bond with thiols through Ga-S bonds, serve as radicals in polymerization reactions, or form coordination bonds with inorganic materials. The outer oxide layer can react with various polymers with hydroxyl groups. **(b)** LM particles (LMPs) modified by brushed polyethylene glycol chains (bPEG) with trithiocarbonate end-groups for slowing-down oxidation and further chemical grafts. **(c)** pH-responsive delivery of doxorubicin

(Dox) using LMPs modified by thiolated hyaluronic acid (m-HA) as the targeting moiety and thiolated (2-hydroxypropyl)-β-cyclodextrin (MUA-CD) as the drug holder. These polymers are conjugated with LMPs by Ga-S bonds. **(d)** Tannic acid (TA)-modified LMPs for improved dispersion stability with TA conjugated on LMPs through a large number of hydroxyl groups. **(e)** LMs modified by inorganic microparticles. **(i)** Transformation of the LM/microparticle composites between three states: power, putty, and liquid, with increasing LM fractions. **(ii)** X-ray photoelectron spectroscopy (XPS) of the pristine LM and LM/Al_2O_3 composite. **(f)** Polydopamine (PDA)-coated LMPs with enhanced photothermal conversion efficiency. The increasing temperature under near-infrared (NIR) irradiation leads to the shape transformation of LMPs due to the dealloying effect. **(g)** Acrylate-containing phosphonic acid ligand grafted on LMPs increases the interactions for improved efficacy of mechanical sintering and electromechanical properties. **(h)** Chemical doping of the oxide layer to activate the conductivity of LMPs. **(i)** Schematic showing the chemical doping of LMPs with ethylene-rich polymers. **(ii)** XPS of the hydrogen-doped LMPs. **(iii)** Conductivity of printed polymer-doped LMPs with different ethylene weight fractions.

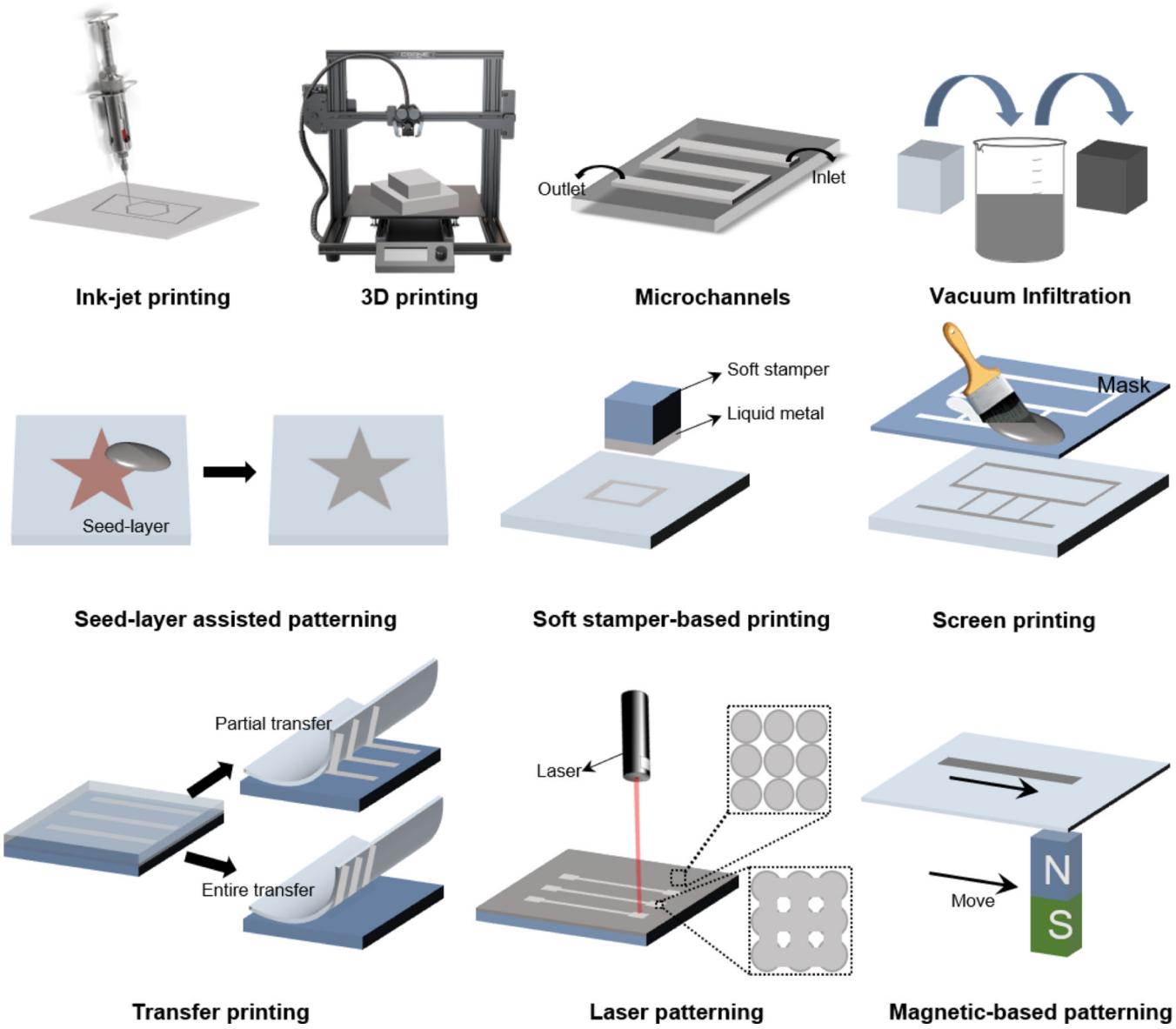

Fig. 3. An overview of LM or LM-based composite patterning techniques

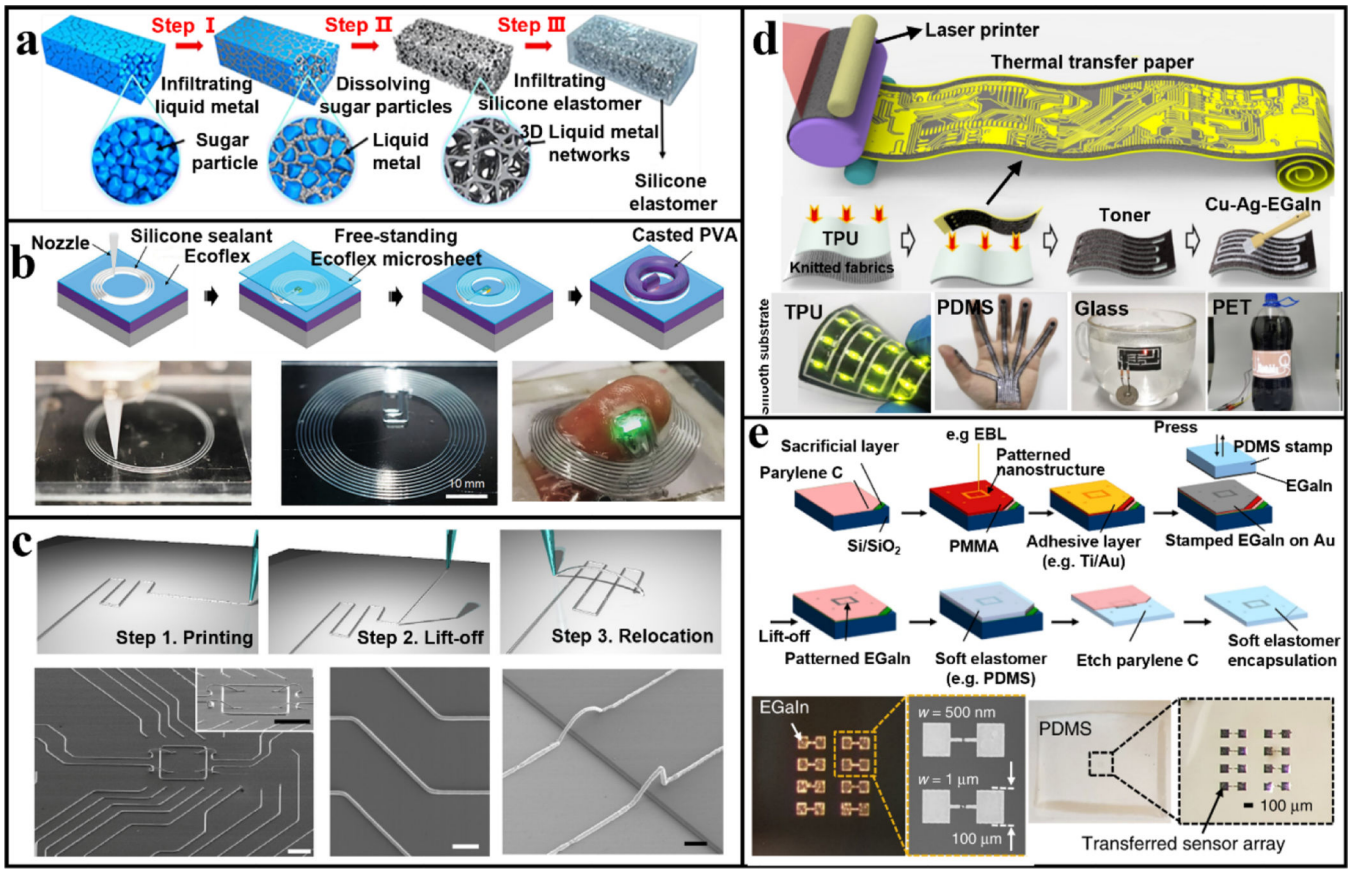

Fig. 4. Patterning of pristine LMs

(a) The fabrication process of 3D LM structures by vacuum-assisted infiltration: 1) vacuum-assisted infiltration of LMs into a dissolvable porous template made of sugar particles, 2) dissolving the sugar template in an ice water bath to keep the 3D LM network in the solid state, and 3) vacuum-assisted infiltration of Ecoflex precursors into the 3D LM network and subsequent curing of Ecoflex at 0˚C. **(b)** Schematic showing direct-print ultrathin microchannels for the injection of LMs (top panel). A PVA layer coated on the microchannel as the reinforcing support layer facilitates the injection process. The bottom panel shows the experimental setup of the 3D printing process (left), the as-fabricated ultrathin LM device in the free state (middle), or on the curvy tissue (right). **(c)** Direct 3D printing of LMs to form high-precision 3D structures through printing, lifting-off, and relocating (top), with the SEM image of 2D and 3D EGaIn patterns shown at the bottom. Scale bar: 10 μm. **(d)** High-yield patterning of Cu-Ag-EGaIn paste on a TPU substrate modified by toner for integrated devices (top). The fabrication process of Cu-Ag-EGaIn patterns starts with laser printing of toner patterns on a thermal transfer paper, followed by transferring to a TPU receiving substrate. Brush-coating the Cu-Ag-EGaIn paste on the TPU substrate forms the reserved image due to the low adhesion between the paste and toner. The bottom panel shows the optical image of the Cu-Ag-EGaIn-based integrated device upon bending deformations or on various curvy surfaces. **(e)** Ultra-high precision LM patterns fabricated by using a metal seed layer defined by electron beam lithography (EBL). The fabrication process starts with coating the PMMA layer on the parylene-C/PAA layer, followed by the

EBL patterning of PMMA. After the deposition of a metal layer on the PMMA layer, LMs are coated on the metal by using a PDMS stamp. The stamped LM/Au is patterned by a PMMA lift-off process and then coated with PDMS. After dissolving the PPA layer in water and plasma-etching of parylene-C, the LM pattern transferred to PDMS is encapsulated by another thin layer of PDMS to complete the fabrication process. The bottom panel shows the as-fabricated LM patterns on the donor substrate or the stretchable receiving PDMS substrate.

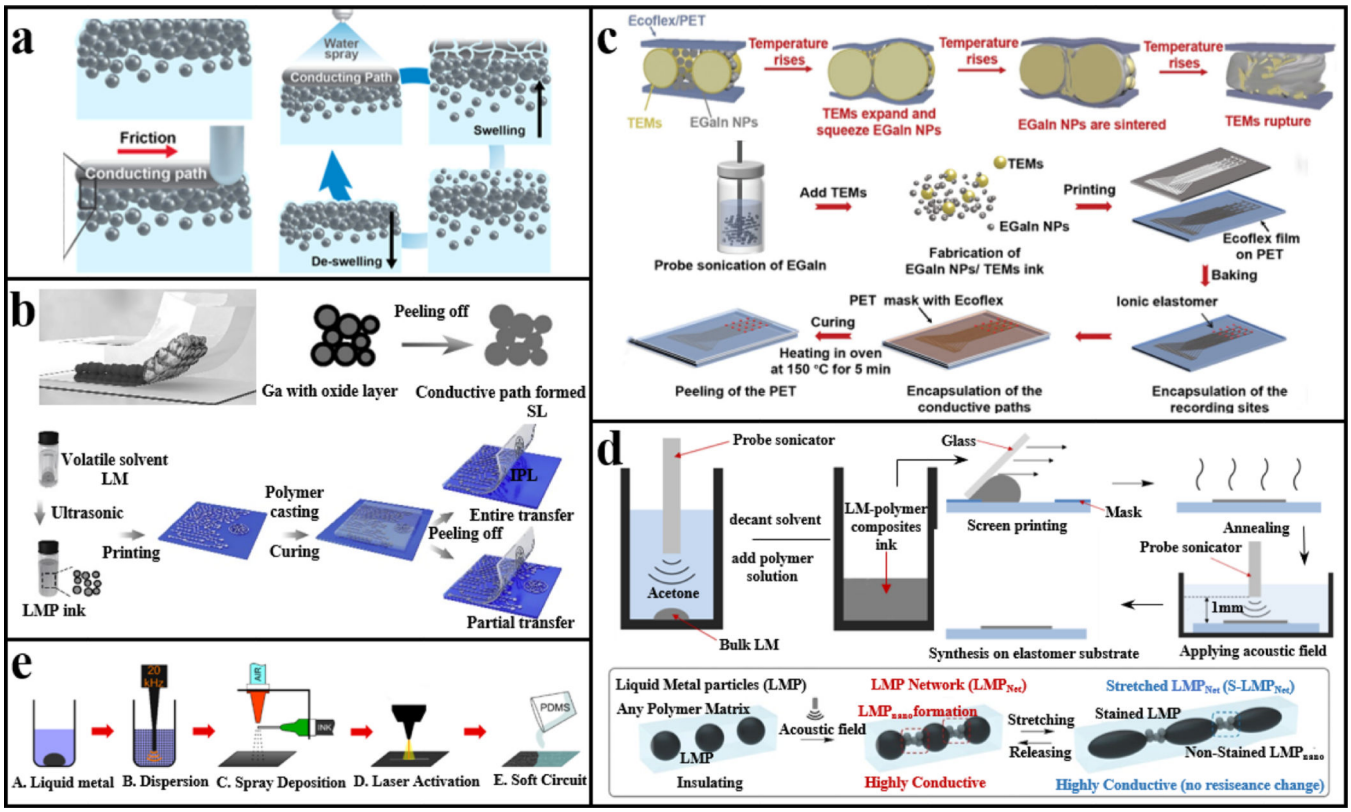

Fig. 5. Patterning of LMPs

(a) The mechanical sintering and erasing process of LMPs in a poly(ethylene glycol) diacrylate(PEGDA) hydrogel. Mechanical loading above the yield stress of Ga_2O_3 ruptures the oxide layer, leading to the formation of conductive pathways. The conductive LM pattern can be erased by water spray to swell PEGDA for the rewriting process. **(b)** LMPs transferred to stretchable substrates are electrically activated due to the tensile stress from peel-off. LMPs in a volatile solvent (n-decyl alcohol) can be printed on the initial patterning layer (IPL) due to the improved wettability. After the evaporation of the volatile solvent, the curable polymer precursor is cast onto the stacked particles as the stripping layer (SL), which is peeled off from the IPL after curing. The entire or partial transfer of LMPs can be tuned by adjusting the affinity between the IPL and SL. **(c)** Thermal sintering of LMPs by utilizing thermal expansion microspheres (TEMs) in the LMP ink. The top panel shows the working principle of thermal sintering of LMPs. The oxide layer of LMPs ruptures to form interconnected conductive pathways at elevated temperatures due to the compressive stress from the thermal expansion of TEMs. The bottom pattern details the fabrication process of an LM-based biopotential sensing patch based on the thermal-activated LMP/TEM ink. The LMP/TEM prepared by tip sonication is patterned on an Ecolex substrate by screen printing. After applying a protective layer on the recording site and an encapsulation layer on the interconnect, the biopotential sensing patch is activated by heating at 150°C for 5 min. **(d)** Electrical activation of LMPs in an LMP/PU composite by the acoustic field (top). The fabrication of LM patterns starts with the screen-printing of the LMP/PU ink on an elastomeric substrate. After curing, the printed LM pattern is activated by a tip sonicator in a water bath. The bottom panel illustrates the mechanism of the acoustic activation

process that relies on the formation of nano-sized LMPs between large LMPs. The small interspacing between nano-sized LMPs permits electron hooping and contributes to the conductive pathway. Upon stretching, the large LMP changes from spherical to ellipsoidal shape to release the local strain, while the shape of nano-sized LMPs and the spacing remain unchanged, leading to a strain-resilience electromechanical property. **(e)** Laser sintering of LMPs to form conductive patterns. The LMP dispersion in ethanol is air-sprayed on an elastomeric substrate, followed by laser-patterning with optimized working parameters. The thermal expansion of the LMP inner core of LMPs from the photothermal effect ruptures the oxide layer and forms conductive patterns. The region without laser scribing remains insulating.

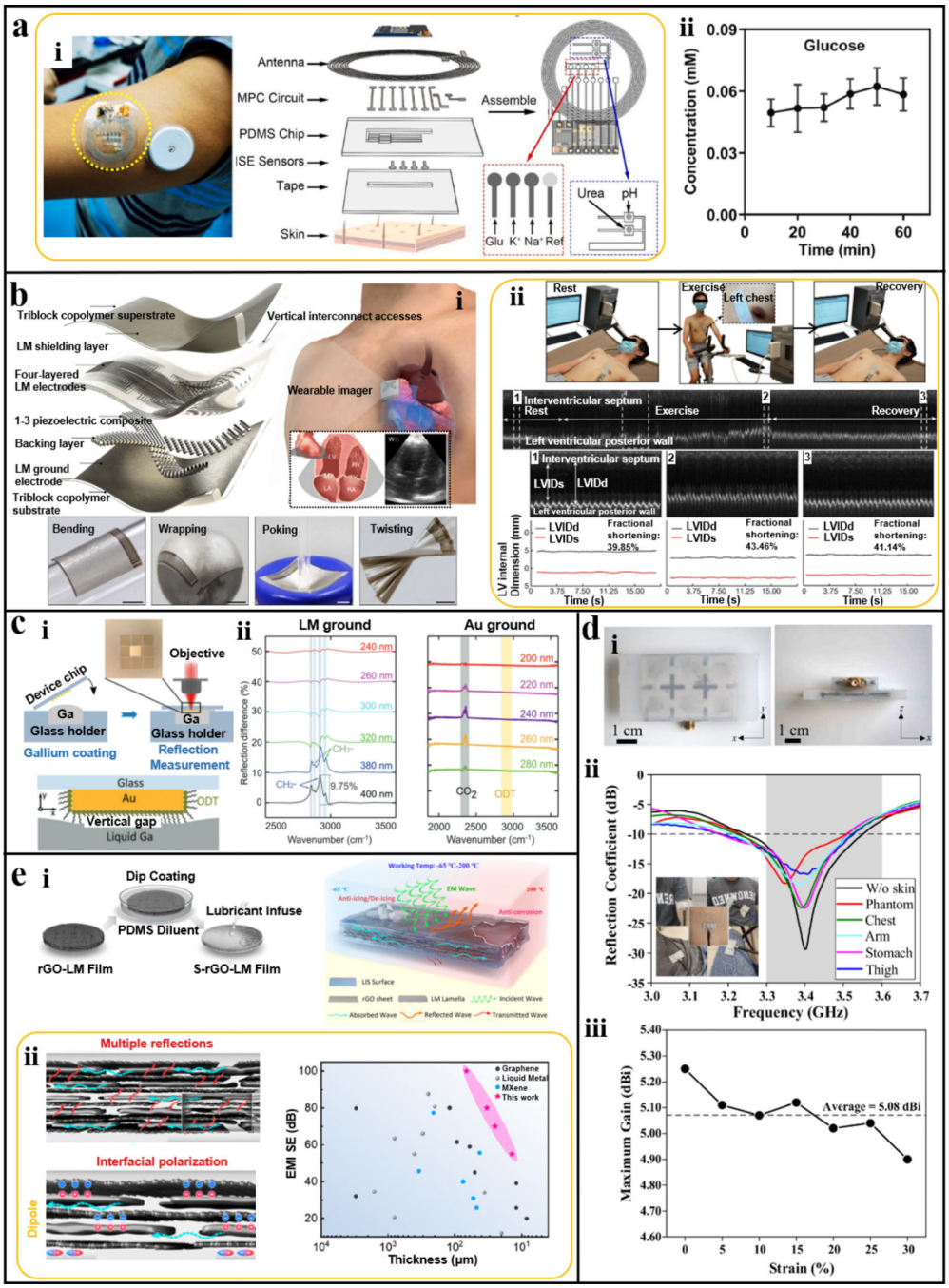

Fig. 6. LM-based passive interconnects, electrodes, or ground planes

(a) LM-based sweat analysis patch for multiplexed biomarker analysis. **(i)** Optical image and exploded illustration of the patch. **(ii)** Measured glucose concentration by the LM-based patch during exercise. **(b)** Stretchable cardiac ultrasound imager. **(i)** Exploded view of the stretchable cardiac imager (top) and its optical images under various deformations (bottom). The LM-based electrodes fabricated by laser engraving provide great stretchability. **(ii)** Stress echocardiography measured by the stretchable cardiac ultrasound imager: resting, riding a stationary bike for 15 min, and laying down for 10 min for recovery. The bottom

panel shows the zoom-in images of stages 1 (rest), 2 (exercise), and 3 (recovery) in the continuous M-mode echocardiography with the extracted left ventricular internal diameter end diastole (LVIDd) and left ventricular internal diameter end systole (LVIDs) waveforms. **(c)** LM-based nanophotonic surface-enhanced infrared absorption (SEIRA) sensor. **(i)** Schematic showing the structure and operation principle of the LM-based SEIRA sensor. **(ii)** Measured reflection spectra of LM or Au plane-based SEIRA towards a self-assembled monolayer 1-octa-decanethiol (ODT). The missing peak for the gold plane-based SEIRA sensor is likely due to the damage of ODT during the metal deposition. **(d)** LM-based wearable antennas for on-body applications. **(i)** optical images of the LM-based wearable antenna composed of a slot antenna backed by a 3 × 2 metasurface. **(ii)** Reflection coefficient of the LM-based antenna placed on different parts of human bodies. **(iii)** Measured gain of the LM-based antenna under different tensile strain levels. **(e)** Slippery reduced graphene oxide-LM (S-rGO/LM) composite for high-performance electromagnetic interference shielding. **(i)** The fabrication process of the S-rGO/LM composite from vacuum filtration of an rGO-LM thin film followed by dip-coating with a thin PDMS layer. The right panel shows the schematic illustration of the EMI shielding performance of the S-rGO/LM composite in harsh environments, such as at a low temperature or in corrosive solutions. **(ii)** The EMI shielding mechanism of the S-rGO/LM composite and its comparison with other reported materials.

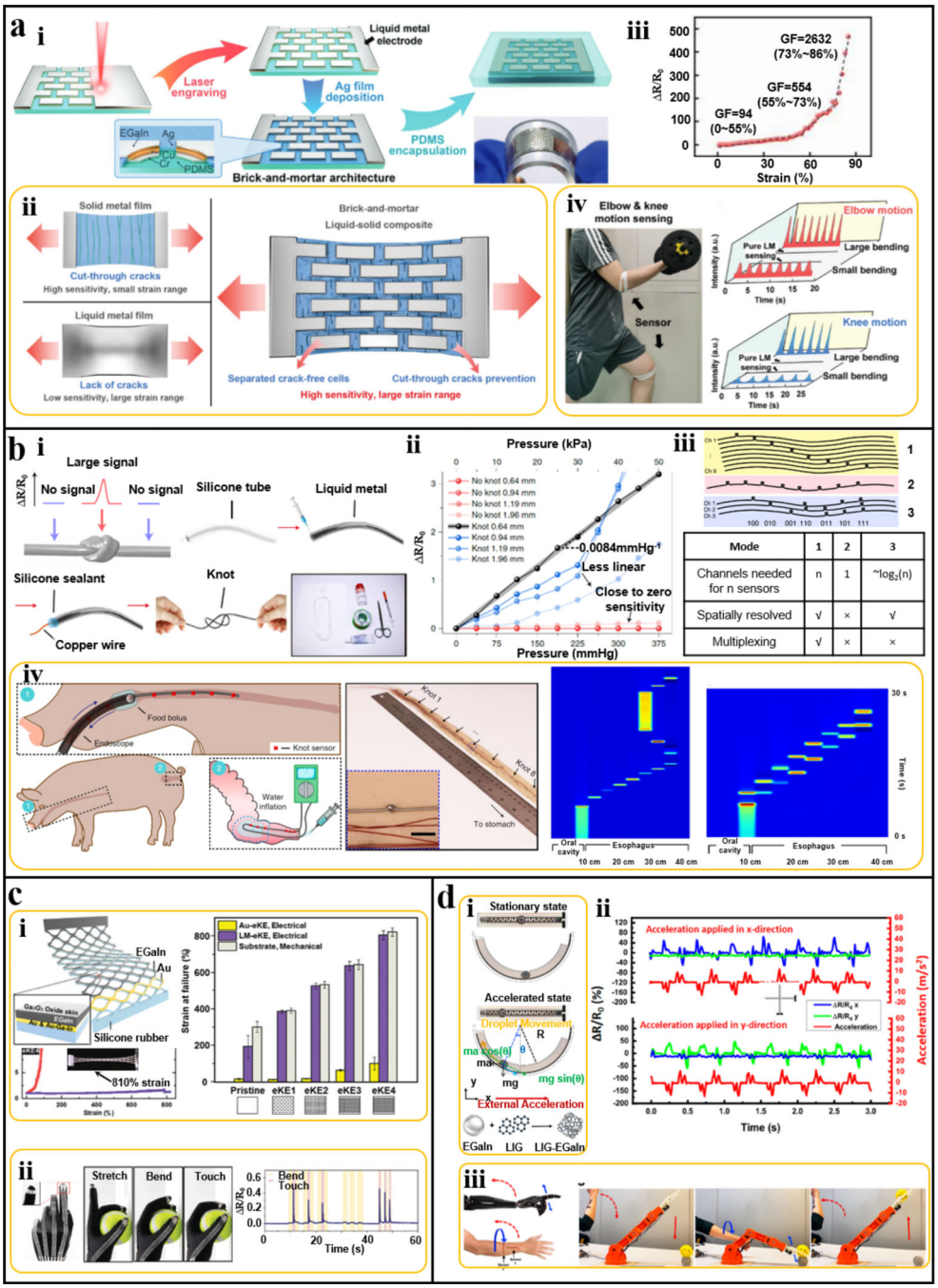

Fig. 7. LM-based flexible/stretchable mechanical or motion sensors

(a) Ultrasensitive LM-based strain sensors with a brick-and-mortar architecture. **(i)** The fabrication process: uniform LM coating on the PDMS substrate with Cr/Cu as the adhesive layer is patterned by laser engraving as the “brick”, followed by depositing Ag on the patterned sample at the regions between the “bricks” to form the “mortar”. **(ii)** Working principle of the brick-and-mortar LM-based strain sensor to simultaneously achieve a large measurement range and high sensitivity, with the measured resistance-strain curve shown in **(iii)**. (iv) Motion sensing at the elbow and knee joints from the patterned (red)

and unpatterned (black) LM-based strain sensors. **(b)** Highly sensitive LM-based pressure sensors with knotting structures. **(i)** The fabrication process and working principle. **(ii)** Measured resistive changes of LM-infused silicone tubing with different outer diameters (0.64–1.96 mm), with or without an overhand knot, as a function of applied pressure. **(iii)** Schematic showing three modes for multiplex pressure sensing. (iv) *In vivo* demonstration of the LM-based pressure sensor for gastrointestinal manometry (left). The sensing mode 1 configuration is adopted to achieve maximum spatial resolution (central). The right panel shows the pressure colour plot from two representative events: retraction and retention of artificial food bolus, and successive passage of two artificial food boluses in the porcine oesophagus. **(c)** LM-based elastic kirigami electrode (LM-eKE). **(i)** Schematic illustration and electromechanical properties of the LM-eKE (left). The right panel shows the comparison in the maximal stretchability between LM-eKE with different kirigami designs. **(ii)** Integration of the strain-insensitive LM-eKE with a pressure sensor in smart gloves to sense gripping, regardless of the bending state of fingers, due to the strain-insensitivity of LM-eKE. **(d)** Inertial sensor based on graphene-coated LMs. **(i)** Schematic showing the inertial sensor consisting of a movable graphene-coated LM droplet and an interdigitated laser-induced graphene electrode with a straight or circular shape in a stationary or accelerated state. The position of the droplet is determined by the acceleration rate, which can be precisely measured by the output voltage. **(ii)** Output of the assembled two-axis inertial sensor when the acceleration is applied along the x- or y-direction. **(iii)** Using two inertial sensors on human arms to control the robotic arm for grabbing.

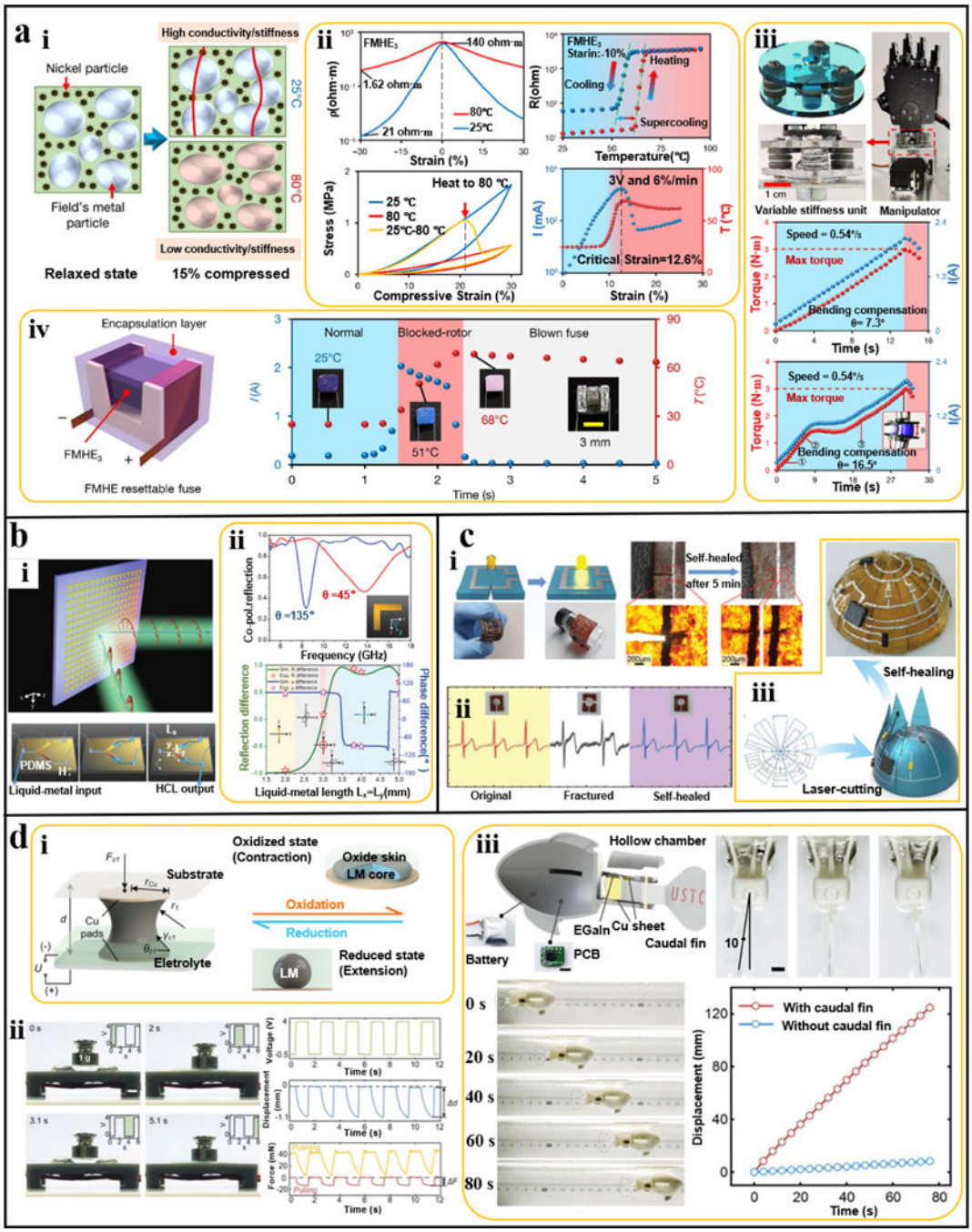

Fig. 8. LM-based smart, electrically reconfigurable flexible/stretchable devices

(a) >Electro-mechano responsive Field's metal-filled hybrid elastomer (FMHE) with tunable conductivity and stiffness. **(i)** Schematic showing FMHE with a Ni/PDMS ratio of 3:1 ($FMHE_3$) under 15% compression at 25 or 80 °C. $FMHE_3$ shows high or low conductivity and stiffness at low or high temperatures (left). **(ii)** The resistivity-strain curve of $FMHE_3$ at 25 or 80°C and stress-strain curves of $FMHE_3$ at different temperatures (left), the resistance-temperature curve of $FMHE_3$ during a heating-cooling cycle under 10% compression and current/temperature-strain curve of $FMHE_3$ powered by a 3V source during compression

(right). **(iii)** Schematic diagram and optical image of the $FMHE_3$ compensation unit integrated into a robotic manipulator (top). Torch and current curves of $FMHE_3$ powered by 0 or 5 V voltage (middle). The blue (or red) shaded region corresponds to the normal (or blocked) operation. The softening of $FMHE_3$ triggered by self-heating leads to an improved compensation angle from 7.3˚ to 16.5˚. **(iv)** Schematic showing the $FMHE_3$ resettable fuse (left) and the corresponding current and temperature curves in a normal-overflow working cycle. Under pre-determined compression, $FMHE_3$ changes from a high to low-conductive state due to the heating effect under overflow, acting as a smart current-limiting fuse. **(b)** LM-based reconfigurable metasurfaces. **(i)** Schematic of the LM-based metasurface and the corresponding L-shaped resonator with tunable geometric parameters and symmetry. **(ii)** Measured spectra of the symmetric L-shaped resonator under normal incident illumination with the electric field along 45° and 135°. Two orthogonal resonant eigenmodes are excited. bb Reflection ($\Delta R = R_{xy} - R_{yy}$) and phase ($\Delta\varphi = \varphi_{xy} - \varphi_{yy}$) differences as a function of LM-arm length in symmetric L-shaped antennas with the y-polarized incident EM wave. Multifunctional polarization conversion can be achieved by changing the arm length. **(c)** Self-healable LM-based flexible electronics. **(i)** Schematic showing LM-based flexible electronics on self-healing hygroscopic randomly hyperbranched polymers (HRHPs). **(ii)** ECG signals collected by the LM/HRHP-based electrode in the original, fractured, and self-healed state. **(iii)** Fabrication of 3D conformal electronics on a hemispherical surface from kirigami assembly by leveraging the self-healing of LM/HRHP-based electronics. **(d)** An LM-based artificial muscle (LMAM) by a reversible oxidation and reduction process. **(i)** Schematic of an LMAM unit reversibly switched between the (reduced) actuated and (oxidized) contracted states. **(ii)** The LMAM actuator composes of four units under a load of 1 g in 100 μL 0.2 M NaOH solution, with the measured displacement and lifting force of the LMAM actuated by a stepwise voltage (4 and −0.5 V at 0.25 Hz). **(iii)** optical images showing the swing of the bionic robotic fish (top panel). The bottom panel shows timelapse images of the robotic fish swimming in the NaOH solution and the corresponding displacement as a function of time.

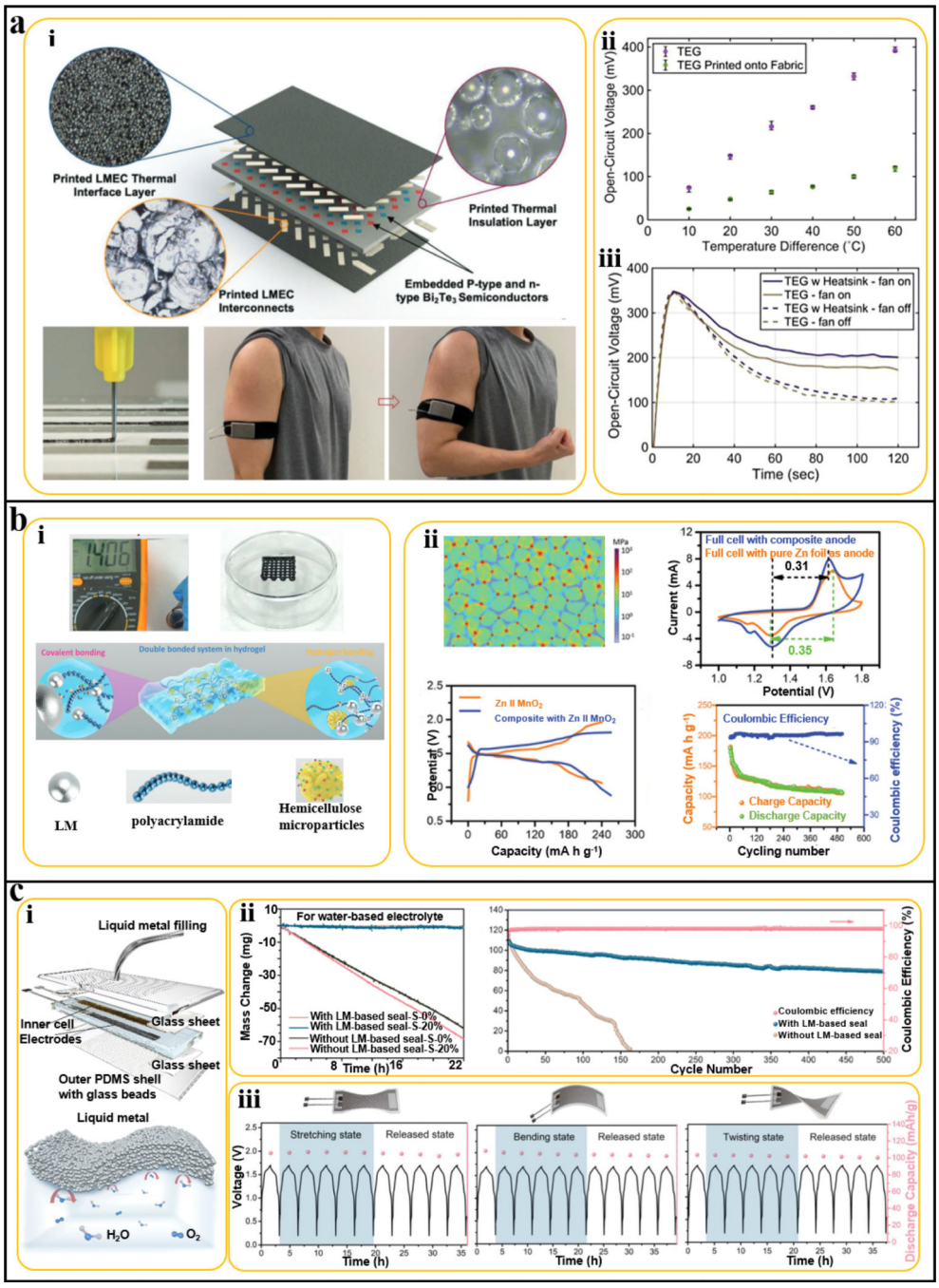

Fig. 9. LM-based energy storage devices

(a) Wearable LM-based thermoelectric generator (TEG). **(i)** Exploded view of the stretchable TEG mainly composed of printed LM elastomer composite (LMEC) interconnects, LMEC-based thermal interface layers, Bi_2Te_3 thermoelectric semiconductors, and thermal insulation layers. The bottom panel shows the printing process of LMEC interconnects and a wearable TEG device on a stretchable fabric armband. **(ii)** Open-circuit voltage of the freestanding TEG device and TEG on the armband as a function of the temperature difference. **(iii)** Open-circuit voltage of the freestanding TEG under

various working conditions such as with a heatsink and/or fan (temperature difference of 60°C). **(b)** LM-based hydrogel composites used as the anode of Zn-ion batteries. **(i)** The image and schematic of the composite made of LMPs, polyacrylamide, and hemicellulose microparticles with double-covalent hydrogen-bonding networks. **(ii)** Simulated stress distribution in the anode during Zn^{2+} plating and stripping. The double-bonding network can effectively dissipate the stress by dynamic breaking and reforming. CV curves of the full cell with the composite or pure Zn foil as the anode at a scan rate of 10 mV/S. Comparison of galvanostatic charge/discharge profile of the full battery at the first scan with a current density of 500 mA/g. Long-term stability of the full cell with the composite anode at charging/discharging current density of 500 mA/g. **(c)** LM-based soft hermetic seals for stretchable systems. **(i)** Schematic showing the exploded view of the LM-based seal integrated into a stretchable lithium-ion battery (LIB) (top) and the good mechanical and hermetic properties (bottom). **(ii)** Mass change of LIBs with and without the LM-based seal, with water-based electrolyte used for all LIBs (left). The right panel shows the room-temperature-cycle life comparison of LIBs with or without the LM-based seal at a current density of 0.6 mA/cm^2. The pink dot is the Coulombic efficiency of the LIB with the LM-based seal. **(iii)** Output voltage (black curve) and discharge capacity (pink dot) of the LIBs with the LM-based sealing before and after stretching (left), bending (middle), and twisting (right).

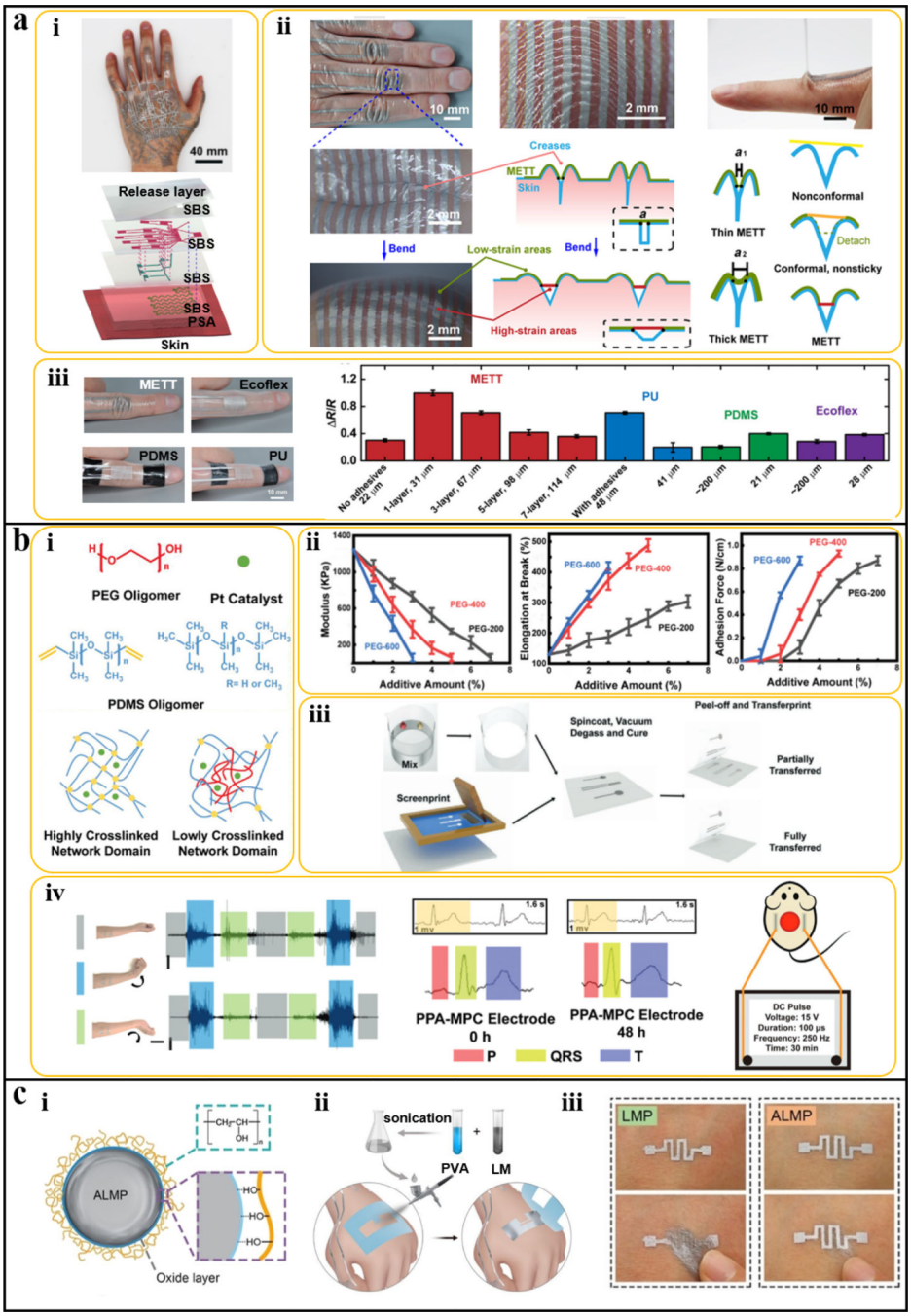

Fig. 10. LM-based adhesive bioelectronics

(a) LM-based electronics using a water-based acrylic pressure-sensitive adhesive. **(i)** Optical image (top) and exploded schematic (bottom) of a multilayered LM-based adhesive electronic transfer tattoo on the dorsum of a human hand. (ii) Optical images of the LM-based tattoo electronics conformally attached to fingers and proximal interphalangeal joints. The thin LM-based tattoo electronics with strong adhesion allow full embedding into the crease structure for highly sensitive strain mapping. **(iii)** Optical images and the strain sensing performance of LM-based electronics on different substrates (i.e., adhesive

PSA, Ecoflex, PDMS, and PU) with different thicknesses. The conformal attachment to the crease structure is the key to achieving the amplification effect. **(b)** LM-based adhesive electronics fabricated on a chemically modified PDMS substrate. **(i)** Schematic showing adhesive PDMS with reduced crosslinking density by adding a small fraction of PEG oligomers into PDMS precursors. **(ii)** The Young's moduli, stretchability, and adhesion strength of the chemically modified PDMS as a function of the additive PEG concentration. **(iii)** Fabrication process of LM patterns on the adhesive PDMS substrate. (iv) Application of the LM-based adhesive electronics in long-time biopotential (EMG and ECG) measurements and electrical therapy for wound healing. **(c)** *In situ* deposition of skin-adhesive LM-based epidermal electronics. **(i)** Schematic showing the chemical structure of skin-adhesive liquid metal particles (ALMPs). The oxide layer forms hydrogen bonds with the hydroxyls on the polyvinyl alcohol (PVA) to achieve strong adhesion to tissues. **(ii)** Patterning process of the PVA-modified LMP on human skins. **(iii)** Optical images of LMP and ALMP patterns before and after a rubbing, washing, and drying cycle.

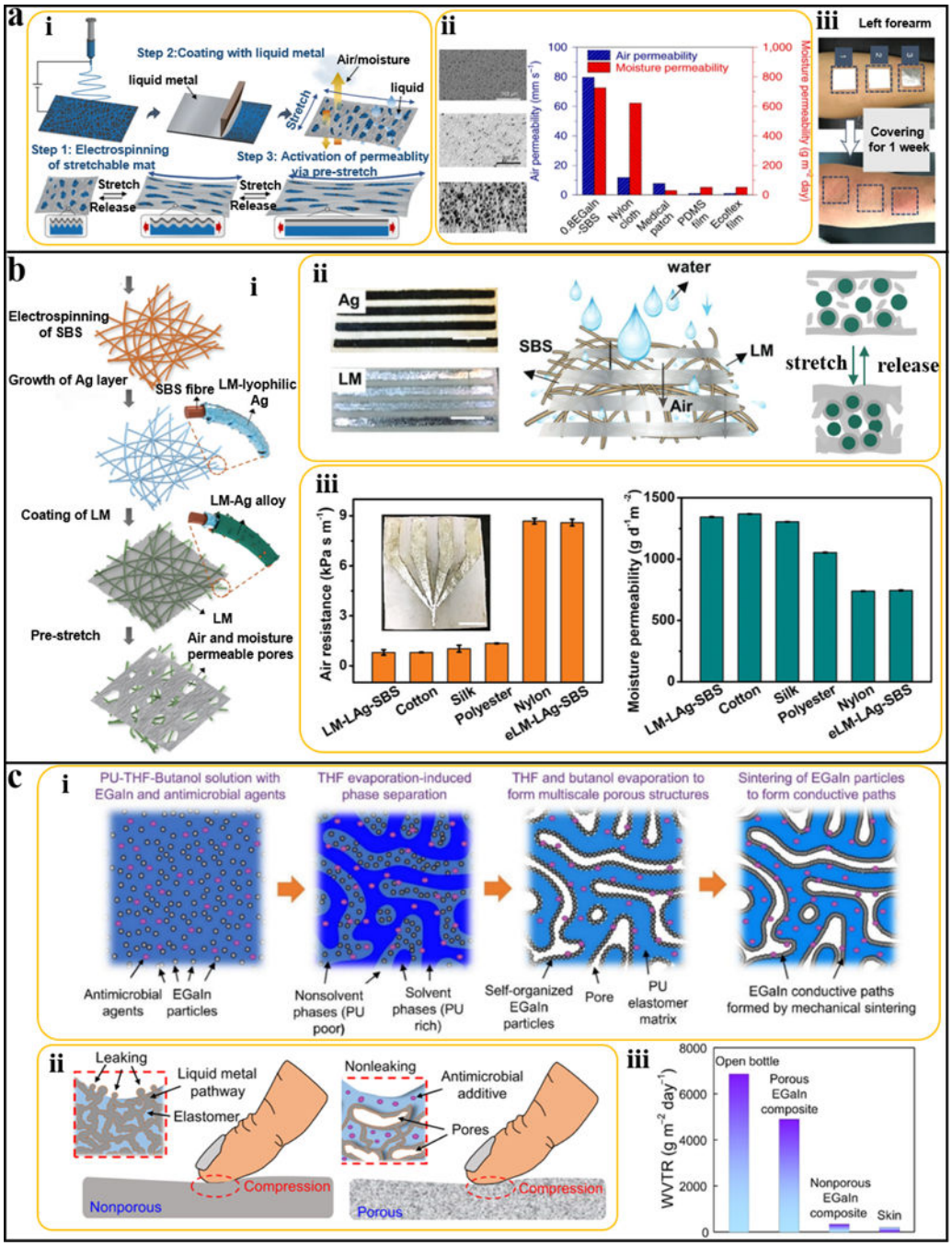

Fig. 11. Highly permeable LM-based electronics

(a) LM/fibrous poly(styrene-block-butadiene-block-styrene) (SBS)-based breathable electronics. (i) The fabrication process of the breathable LM/SBS-based electronics: electrospinning of SBS fiber, LM coating, and activation of permeability by pre-stretching. The bottom panel illustrates the structure of the LM/SBS mat from the top and cross-sectional views during stretching. The mesh-like hole and vertical wrinkle form after the pre-stretch cycles due to the destruction and reconstruction of the oxide layer. (ii) SEM images of the SBS substrate and the LM/SBS mat before and after activation. The right

panel shows the superb air and moisture permeability of the LM/SBS mat, compared with the nylon clothes, medical patch, PDMS, and Ecoflex film. (iii) Optical images showing the skin irritation results for different materials (1: SBS mat; 2: LM/SBS mat; 3: non-permeable LM-SBS mat). **(b)** Highly permeable and strain-resilient LM-lyophilic Ag-SBS (LM-LAg-SBS)-based electronics. (i) Preparation of the LM-LAg-SBS mat: electrospinning of SBS fibers, *in situ* growth of the Ag seed layer, LM coating, and pre-stretch activation. (ii) Optical images of the LAg-SBS mat before and after LM coating (left). The right panel shows the mechanism of the gas permeability of the LM-LAg-SBS mat in the free or stretched state. (iii) Measured air resistance and moisture permeability of the LM-LAg-SBS mat and other commonly used materials (i.e., cotton, silk, polyester, and nylon). Encapsulation of the LM-LAg-SBS mat significantly reduces its air permeability. **(c)** LM-PU-based porous composites. (i) Schematic showing the phase separation-based synthesis of porous soft LM-based composites. The porous structures are formed due to the phase separation of THF and 1-butanol with different boiling points. (ii) Schematic showing the mechanism of the high leakage resistance of the porous soft LM-base composites due to damping effects of the porous structure against mechanical deformation. (iii) Water vapor transmission rates (WVTRs) of an open bottle, porous EGaIn composite, nonporous EGaIn composite, and skin.

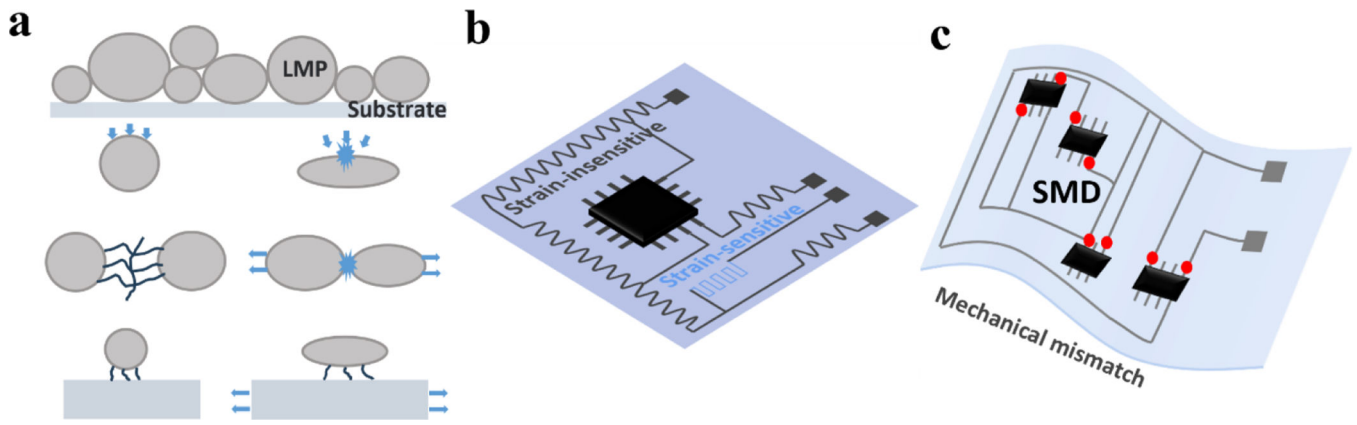

Fig. 12. Highly permeable LM-based electronics

(a) High-resolution LM patterning involves the issues of yield strength, mechanical sintering, and interacting with supporting substrates of LMPs in submicron scale. **(b)** Schematic showing All-LM-based stretchable electronics with spatially dependent electromechanical properties (i.e., strain-insensitive and strain-sensitive). **(c)** LM-based integrated stretchable electronics with surface mountable devices (SMDs).

Table 1

Summary of physical, chemical, and mechanical properties of Ga-based LMs

	G a	**E G a I n**	**Galinstan (GaInSn)**
Melting point (°C)	29.77 [256]	15.7°C [257]	-19°C [258]
Boiling point (°C)	2205 [256]	2000 [259]	>1300 [258]
Surface tension (mN/)	705–730 [25]	624 [260]	600 [25]
Oxidized surface tension (mN/m)	NA	356 [25]	364 [25]
Viscosity (Pas)	1.37×10^{-3} @ 350 °C [261]	1.99×10^{-3} [262]	2.4×10^{-3}@ 20 °C [258]
Vapor pressure (Pa)	9.31×10^{-36}@ 29.9 °C [256]	NA	$<10^{-6}$@ 500 °C [258]
Thermal conductivity ($Wm^{-1}K^{-1}$)	28.1 [256]	26.4 [137]	16.5 [256]
Electrical resistivity (μΩ·m)	0.13 [256]	0.29 [262]	0.43 [256]

Table 2

Comparison of various LM or LM-based composite patterning techniques

Types	Compositions	Patterning	Working principles	Complexity	Substrates	Features	References
Pristine LMs	**Ga**	3D printing	The self-supporting oxide layer on the surface of extruded LMs	High	Rigid substrates or hydrogel matrixes	10 μm, small size, 3D structures	114-117, 119-122
	EGaIn	Microfluidic	Manual Injection of LMs into microfluidic channels fabricated from elastomers	Low	silicone elastomers	50–100 μm, large size, 2D patterns	108, 112, 113
		Infiltration	Penetration of LMs into porous elastomers fabricated from dissolvable templates by vacuum	Low	Silicone polymers	mm-level, large size, 3D networks	110, 111
		Seed-layer-assisted patterning	Designing adhesion contrast on stretchable substrates by selective metal deposition	High	Various elastomers	0.5 μm, small size, 2D patterns	125, 126, 130-133
		Soft stamper-based printing	Intimate contact between the stamper and substrate to force the LM into the mask pockets	Low	Various elastomers	50 μm, large size, 2D patterns	30, 134
LMP dispersions	**LMP/solvents**	Screen/stencil printing	Direct patterning of LMPs on stretchable substrates through masks	Low	Various elastomers	100 μm, large size, 2D Patterns	43, 44, 263
		Transfer printing	Patterning LMPs on sacrificial substrates, then transferring to stretchable substrates	Low	Adhesive elastomers/ liquid precursors	100 μm, large size, 2D patterns	152, 264
		Laser sintering	Laser patterning and sintering of an LMP coating on stretchable substrates in one step	Low	Various elastomers	100 μm, large size, 2D patterns	155, 156, 265
LM/LMP-based composites	**LMP/polymer**	Molding	Pouring LMP/ polymer composites into printed 3D molds	Low	Not applicable	mm-level, large size, simple bulky shapes	11, 266
		Screen/ stencil/i nk-jet printing	Direct patterning of LM/polymer composites on stretchable substrates	Low	Various elastomers	100 μm, large size, 2D patterns	143, 147, 153, 267
		Laser patterning	Laser cutting or scribing of cured LM/polymer composites	Low	Various elastomers	200 μm, large size, 2D patterns	268, 269
	LM/ microparticles	Screen/stencil printing	LM mixed with microparticles owes improved	Low	Various elastomers	50 μm, large size, 2D patterns	124, 270-272

Types	Compositions	Patterning	Working principles	Complexity	Substrates	Features	References
			rheological properties for printing				
		Magnetic-based patterning	LM mixed with magnetic microparticles offers printability and magnetic manipulation	Low	Various elastomers	500 μm, large size, 2D patterns	273-276
	LM/ nanoparticles	3D/ink-jet printing	LM mixed with microparticles for reinforced mechanical stiffness	High	Freestanding	5 μm, small size, 3D structures	121, 277